Conical Quasioptical Dielectric Resonator

A. A. Barannik, S. A. Bunyaev*, and N. T. Cherpak

Usikov Institute of Radiophysics and Electronics, National Academy of Sciences of Ukraine, Kharkov, Ukraine
* e-mail: bunyaev@ire.kharkov.ua
Received April 18, 2005

Abstract—A dielectric resonator of the new type—conical quasioptical dielectric resonator—is proposed. The dependence of the resonance oscillation frequency, the quality factor, and the electric field distribution on the cone angle of such a resonator with a conducting screen in the base plane has been experimentally studied in the 8-mm (*Ka*-band) wavelength range. © 2005 Pleiades Publishing, Inc.

Introduction. Quasioptical dielectric resonators featuring oscillations of the whispering gallery mode type have been studied and implemented predominantly with the shape of a round cylinder (see, e.g., [1]). In recent years, it has been demonstrated that such cylindrical quasioptical dielectric resonators with conducting end screens can be used for the measurement of the surface resistance R_s of thin high-temperature superconductor (HTSC) films [2, 3]. Advantages of this method are the increased sensitivity in the region of small R_s in the millimeter wavelength range and the possibility of measuring the absolute R_s values, since the electromagnetic field structure in said resonators is determined directly from a solution of the Maxwell equations. However, a significant disadvantage of this approach consists in that the obtained values of surface resistances refer to two HTSC films. Determination of the individual R_s values requires conducting a round-robin procedure [4], which encounters practical difficulties.

In order to solve this problem, it would be natural to seek for a special resonator geometry which would involve a single conducting surface but still allow an analytical solution of the electrodynamic problem. Such a geometry is offered by the dielectric hemisphere on a metal plane [5]. However, manufacturing high-*Q* hemispherical quasioptical resonators from single crystal leucosapphire involves a rather complicated and laborious technology.

An alternative solution is offered by a quasioptical dielectric resonator having the shape of a cone with a conducting screen in the base plane. Unfortunately, a theoretical description of such resonators has not yet been developed. For this reason, we have experimentally studied a resonator with this geometry and measured the resonance oscillation frequency, the quality factor, and the electric field distribution depending on the cone angle α relative to the axis.

Experiment. We have studied Teflon resonators having the shape of a truncated cone with the generatrix

slope angle relative to the axis varied from 0° to 35°. The resonator height *h* was equal to the base radius *R* = 39 mm. The measurements were performed for both open resonators (without a conducting screen in the base plane) and those with a conducting base surface (brass screen) in the 8-mm wavelength range. The resonator was excited using rectangular dielectric (Teflon) waveguides with one metal-coated surface. The waveguide orientation was selected so as to excite HE modes in the cylindrical resonator (α = 0) and was the same for the other cone angles. The quality factor was determined from the resonance linewidth under weak coupling conditions. The electric field distribution in the resonator was measured using a metal probe.

Experimental results. Figures 1 and 2 show the results of measurements of the resonance frequency *f* and the quality factor *Q* as functions of the cone angle α. The measurements were performed for the $HE_{371\delta}$ mode, where *n* = 37 is the azimuthal index, *m* = 1 is the
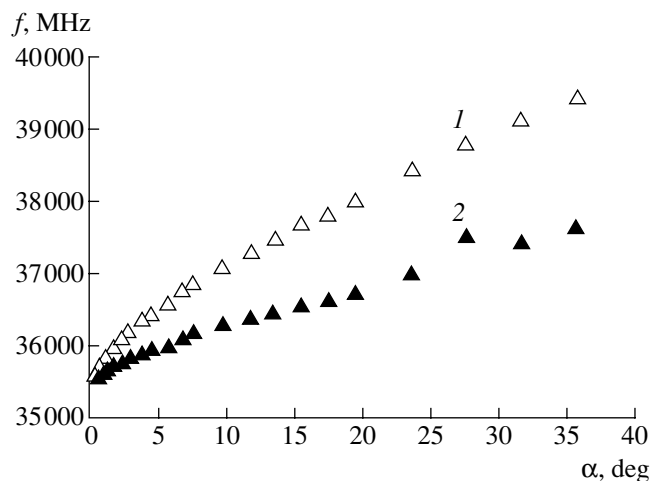

Fig. 1. Plots of the resonance frequency *f* versus generatrix slope angle relative to the axis for a conical quasioptical dielectric resonator (*1*) without and (*2*) with a conducting screen in the base plane.

Fig. 2. Plots of the experimental quality factor Q versus generatrix slope angle relative to the axis for a conical quasioptical dielectric resonator (*1*) without a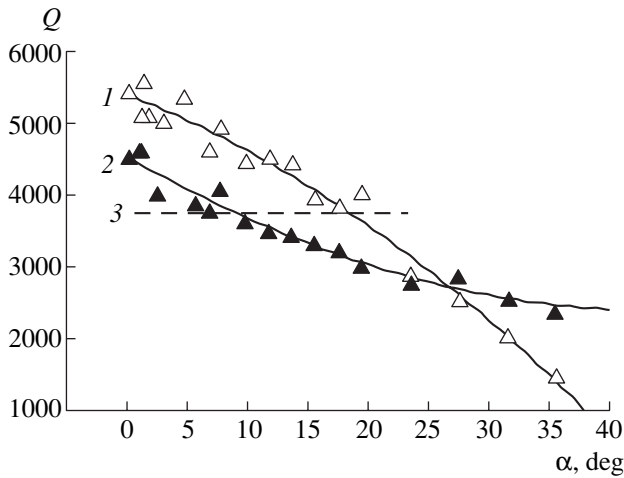nd (*2*) with a conducting screen in the base plane. Dashed line *3* shows the Q value of a hemispherical resonator with a conducting screen in the base plane.

number of field variations along the radius of the cone base, and $\delta \leq 1$ is the number of field variations along the cone axis. As can be seen, a change in α is accompanied by evolution of the resonator properties.

The resonance frequencies of both the open resonator and that with the conducting screen in the base plane increase with the cone angle α (for n = const). The growth is more pronounced for $\alpha < 3°$ than for $\alpha > 3°$ and becomes virtually linear in the interval of $\alpha = 10°-35°$. The further increase in f for the open resonator is almost twice that for the system with a conducting end screen (Fig. 1).

The behavior of the Q values shows that the quality factors of both open and screened resonators decrease with increasing α. However, the Q value of the open resonator exhibits a sharp drop at $\alpha > 20°$, while the variation of Q of the resonator with the end screen slows down for $\alpha > 10°$. The inverse quality factor of the resonator as a function of α can be described using the following formula:

$$Q^{-1} = k\tan\delta + A_s R_s + Q_{rad}^{-1}, \qquad (1)$$

where k is a constant factor close to unity, $\tan\delta$ is the loss tangent of the dielectric material, A_s is the coefficient of inclusion of the conducting end screen, R_s is the surface resistance of a metal used in the conducting screen, and Q_{rad} is the radiation quality factor. As the α angle is increased, the unloaded Q of the open resonator ($A_s = 0$) can increase only at the expense of radiation

losses. At the same time, the Q value of a quasioptical dielectric resonator with a conducting end screen can decrease as a result of the growth in both A_s and Q_{rad}^{-1}. The former factor is useful from the standpoint of increasing the sensitivity of the R_s measurements, while the latter factor has to be taken into account to provide the condition $Q_{rad}/Q \gg 1$ necessary for retaining a high measurement accuracy. For comparison, Fig. 2 also shows the Q value of a hemispherical quasioptical dielectric resonator with a conducting base plane. As can be seen, the quality factor of this resonators is equal to that of a screened conical resonator with $\alpha \approx 9°$.

The results of our investigation of the electric field variation along the Z axis coinciding with the longitudinal axis of the resonator showed that, at small cone angles ($\alpha = 5°-10°$), the field is "pressed" against the impedance plane, which improves the interaction between the field and the conductor and leads to an increase in A_s.

Conclusion. We have experimentally demonstrated the possibility of exciting whispering gallery modes in dielectric resonators having a truncated cone shape, both with and without a conducting end screen, for the cone generatrix slope angle relative to the axis varied from 0° to 35°.

The field structure in the resonator depends on the cone angle α, which makes it possible to control the resonator properties (f, Q_{rad}^{-1}, A_s) and can be used in such resonators for various microwave applications.

At small cone angles ($\alpha = 5°-10°$), the energy characteristics of a conical resonator with the conducting end screen are close to those of a screened hemispherical resonator. With allowance for the relative simplicity of manufacturing conical resonators, this fact opens ways to the use of conical sapphire resonators in impedance measurements for normal conductors and superconductors.

REFERENCES

1. X. H. Jiao, P. Guillon, I. A. Benmudes, *et al.*, IEEE Trans. Microwave Theory Tech. **35**, 1169 (1987).
2. N. T. Cherpak, A. A. Barannik, Yu. V. Prokopenko, *et al.*, IEEE Trans. Appl. Supercond. **13**, 3570 (2003).
3. N. T. Cherpak, A. A. Barannik, Yu. V. Prokopenko, *et al.*, Supercond. Sci. Technol. **17**, 899 (2004).
4. Z.-Y. Shen, *High-Temperature Superconducting Microwave Circuits* (Artech House, Nortwood, 1994).
5. S. Kharkovsky, Y. Filipov, and Z. Eremenko, Microwave Opt. Technol. Lett. **21**, 252 (1999).

Translated by P. Pozdeev

Sound Generation in Sliding Friction

A. V. Kolubaev*, E. A. Kolubaev, I. N. Vagin, and O. V. Sizova

*Institute of Strength Physics and Materials Science, Siberian Division, Russian Academy of Sciences,
Tomsk, 634055 Russia*
* *e-mail: root@ispms.tomsk.ru*
Revised manuscript received April 1, 2005

Abstract—The process of sound generation in a sliding friction contact in the absence of lubricants has been studied simultaneously with measurements of the friction coefficient. A correlation between the sound intensity, the spectrum of sound generated in the tribological system, and the friction coefficient is established. It is shown that not only do the tribological properties of contacting materials influence the characteristics of the acoustic signal, but the reverse influence may take place as well: the elimination of elastic oscillations accompanied by sound generation in the junction leads to a decrease in the friction coefficient. © 2005 Pleiades Publishing, Inc.

Under certain conditions of sliding friction, the junction in a friction couple becomes a source of vibration and/or acoustic emission (sounding like noise, creak, or scream). Using special equipment, it is also possible to detect ultrasonic signals [1] accompanying the friction. All these phenomena reflect the elastic oscillations arising due to the relative motion of contacting surfaces in the friction couple. The nature of elastic oscillations accompanying friction has been studied for a long time, and now it is commonly accepted that the main factor responsible for these oscillations is a decrease in the friction coefficient with increasing relative sliding velocity [2]. However, the mechanics does not indicate a reason for this decrease in the friction coefficient. According to one assumption [3–6], the elastic oscillations are caused by the fluctuating friction force, which can be induced by the deformation of surface roughnesses or by their adhesive interaction with the conjugated surface, as well as by the detachment of particles of the worn material. All these processes may give rise to variations in the friction coefficient, which determines a relation between the friction force and the normal load, and it not excluded that these variations will be exactly such that are necessary in order to excite oscillations in the tribological system under consideration. A relation between the elastic oscillations and wear in friction was also pointed out in [7], where it was concluded that the greater the wear, the higher the intensity of sound caused by the fretting process. A decrease in the extent of wear upon elimination of the ultrasonic oscillations in the friction couple was reported in [8].

Thus, we may ascertain that elastic oscillations, including those accompanied by the generation of sound, are determined by the tribological properties of materials in the friction couple and are related to the rate of wear and the coefficient of friction. The other aspect of the excitation of elastic oscillations in sliding friction—namely, their influence on the characteristics of friction—is practically unconsidered in the available literature, except for the aforementioned paper [8], where a decrease in wear in the stage of surface fitting was observed upon damping the sample with absorbing gaskets that eliminated the excitation of ultrasonic oscillations.

This Letter presents the results of investigation into the dry sliding friction and the related excitation of acoustic oscillations in the tribological system in the range of sound frequencies. We have compared the friction coefficient, on the one hand, and the intensity and spectrum of sound generated in the friction coupe, on the other hand. The tribological tests were carried out for 6 h on a 2168 UMT testing machine in the shaft-in-sleeve mode at a rotation speed of 0.7 s^{-1} and a normal load varied from 250 to 2500 N. The sleeves were made of a wear-resistant G13 steel and had an inner diameter of 31.1, 31.2, and 31.3 mm and a height of 10, 20, and 30 mm; the conjugated shafts with a diameter of 31.0 mm were made of a 42KhM4F chromium-based steel and heat-treated to $HRC = 56$. Both sleeves and shafts were fabricated according to the accuracy class 2, with a limiting diameter deviation of $\Delta = +25$ μm for the sleeves and $\Delta = -25$ μm for the shafts.

The acoustic signals were recorded, characterized, and processed in a personal computer using a standard program for digital sound processing. The signal was detected with a KhM8500 microphone having an amplitude ripple of ± 5 dB in a passband from 100 to 1.5×10^4 Hz. The readings of the frictional torque sensor were monitored once per second.

The influence of oscillations generated in the tribological system on the friction coefficient was studied using a specially designed device, in which the sample and the counterbody were mounted. This device admitted the arrangement of damping sleeves on the outer, inner, or both surfaces of the working junction, which
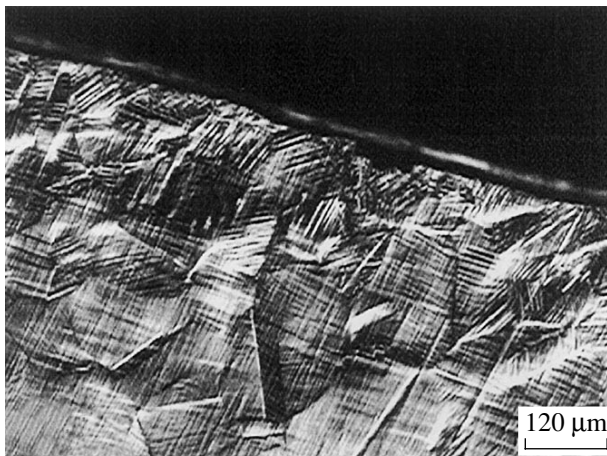
Fig. 1. A micrograph of the side surface of a sleeve in the friction zone observed upon a 6-h test with a damping device decreasing the intensity of sound generated in the friction couple.

allowed us to control the parameters of high-frequency oscillations of the tribological system in the course of tests. The sound served as an indicator of the state of the junction, by which it was possible to judge the efficacy of damping. The main aim of investigations in this testing system was to vary the parameters of autooscillations at the tribological junction, while maintaining constant regimes and conditions at the contact. The main tests were performed on the sleeves with an inner diameter of 31.2 mm and a height of $L = 10$ and 20 mm, at a normal load to 300 and 250 N, respectively.

As is known [9, 10], Hadfield steel (G13 grade) is characterized by a high wear resistance, which is related to the ability of this material to develop an extremely high rate of strain hardening within a 50-μm-thick surface layer. Figure 1 shows a micrograph of the preliminarily polished side surface of a sleeve in the friction zone observed upon a 6-h test. As can be seen, the sample surface is deformed to a much greater depth as compared to the values reported in the literature cited. In all tests, the strained relief on the side surface of sleeves had generally the same character as that depicted in Fig. 1, with the friction-modified depth dependent only on the load, irrespective of the presence or absence of the damping sleeves. It should be noted that a static pressure of the same magnitude as that applied in the course of friction (slightly above 1 MPa) does not produce any visible traces of deformation in the samples. Thus, the deformation observed in a surface layer whose thickness reached about 700 μm was caused entirely by the elastic excitation. The fact that the depth of the deformed relief was the same with and without damping indicates that the frequency range of oscillations generated during friction is much wider than that detected by the microphone. It should also be noted that the damping device probably modified the spectrum of elastic oscillations, eliminating them in

one frequency interval and inducing in some other interval outside the microphone sensitivity band.

The wear of sleeves tested with and without damping was determined in the contact area—more exactly, on the arc along which the shaft and sleeve were in contact. For example, the length of this line for 10-mm-long sleeves was within 25–30 mm (at a 300 N load) and exhibited no regular influence of the damping device. However, a comparative analysis of the acoustic signal and the friction coefficient f_{fr} revealed a correlation between the sound intensity and spectrum and the f_{fr} value. Once this fact was established, the subsequent investigation was concentrated on these characteristics.

The results of our sliding friction tests confirmed the existing notions concerning the relationship between the sound intensity and the friction coefficient. In all variants of testing, it was found that a decrease in f_{fr} led to a reduction in the intensity of sound generated by the friction couple. The friction coefficient exhibited a decrease with increasing pressure in the friction zone. This pressure could be varied by changing the sleeve size or the external load applied to the junction. It is interesting to note one specific feature revealed by analysis of the sound spectrum: an increase in the applied load was accompanied by a decrease not only in the friction coefficient and the sound intensity but in the number of characteristic sound frequencies in the acoustic signal spectrum as well.

Figure 2 shows the results of simultaneous monitoring of the acoustic signal and friction coefficient in a standard test without damping, whereby the dry sliding friction is accompanied by the sound generation. These data were obtained for a sleeve with a diameter of 31.2 mm and $L = 20$ mm under a load of 250 N. As can be seen from the signal amplitude variation in Fig. 2a, the sound is periodically generated at a repetition rate of ~1.5 s^{-1}. The spectrum of sound (Fig. 2b) consists of a series of harmonics, with each peak probably reflecting the excitation of different parts of the tribological junction, including certain elements of the testing machine. The character of sound and the intensity and spectrum of the acoustic signal during each test remained unchanged. Figure 2c shows a plot of the friction coefficient versus time, which can be seen to vary in a random manner with small amplitude about an average level.

The data presented in Fig. 3 show that the use of a specially designed damping device holding the sample and counterbody significantly decreased the intensity (Fig. 3a) and changed the spectrum (Fig. 3b) of sound generated in the otherwise identical friction couple. As can be seen, the resonance frequencies have disappeared and the level of sound only rather slightly exceeds the sensitivity threshold (–120 dB). This change in the characteristics of sound generated in the tribological system for the same test regime and contact conditions must also influence the friction coefficient. Indeed, the average f_{fr} value in Fig. 3c is lower than that
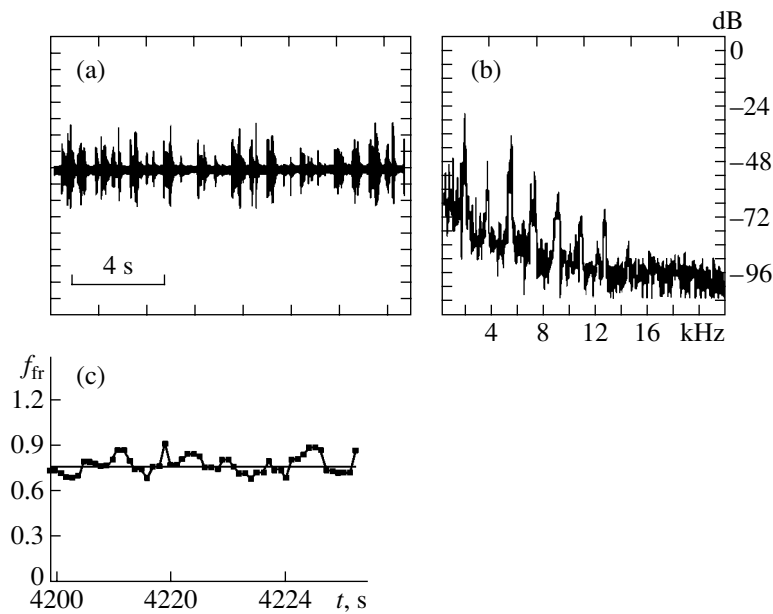
Fig. 2. (a) Time series of the amplitude of sound (arbitrary units), (b) the spectrum of sound, and (c) time variation of the friction coefficient for a sleeve with a diameter of 31.2 mm tested without a damping device.

Fig. 3. (a) Time series of the amplitude of sound (arbitrary units, the same scale as in Fig. 2), (b) the spectrum of sound, and (c) time variation of the friction coefficient for a sleeve with a diameter of 31.2 mm tested with a damping device.
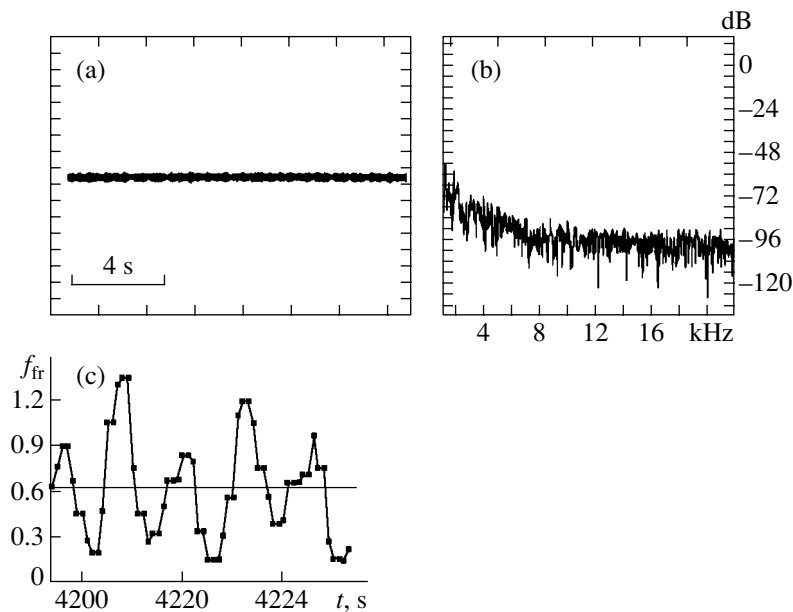
in Fig. 2c. In addition, the time variation of f_{fr} acquired a pronounced periodic character with the amplitude significantly exceeding the level of fluctuations observed in Fig. 2c. A comparison of the friction coefficient profile in Fig. 3c to a sinusoidal fitting curve showed evidence for a good coincidence with a correlation coefficient of $r = 0.87$. Note that the correlation coefficient calculated in the same way for the curve in Fig. 2c was $r = -0.25$. The period of oscillations in the

friction coefficient in Fig. 3c is several times greater than the period of sleeve rotation, so that this behavior cannot be related to rotation of the shaft of the testing machine or to some features of its design. Such a periodic variation of the friction coefficient (similar behavior was observed in our previous friction tests on wear-resistant steels) is probably related to the periodic character of the wear process, as was also pointed out by other researchers [5]. As is known, the process of wear

involves the stage of defect accumulation in a surface layer, whereby the material exhibits strain hardening, and the stage of intensive fracture in this layer with the detachment of particles of the worn material. The absence of periodicity in variation of the friction coefficient in the tests performed in a usual tribological system can be related to the different character of wear, whereby the duration of the aforementioned wear stages exhibits random variations under the action of elastic stresses caused by oscillations of the elements of the tribological junction. The possibility of such influence of the elastic wave on the friction couple was confirmed by the results of our mathematical modeling of the friction process [6], according to which the elementary event of plastic shear on the surface took place when the elastic wave front arrived at this surface. In such cases, the friction stress and the stress related to the elastic wave are added to induce plastic straining at the surface.

The aforementioned correlation between the sound intensity in sliding friction and the friction coefficient in the tests with G13 steel was repeatedly observed under different conditions of loading, both with and without special sample holders. Therefore, we may suggest that the friction coefficient is determined not only by the physicochemical interaction of conjugated surfaces but also depends on the energy losses related to the excitation of high-frequency oscillations. Thus, the results of our tests showed that the excitation of oscillations accompanied by sound generation and the friction coefficient are influences by the pressure in the contact zone and by features of the tribological system design. In some cases, the elimination of elastic oscil-

lations in the tribological junction leads to a decrease in the friction coefficient.

REFERENCES

1. A. I. Sviridenok, N. I. Myshkin, T. F. Kalmykova, and O. V. Kholodilov, *Acoustical and Electrical Methods in Triboengineering* (Nauka i Tekhnika, Minsk, 1987) [in Russian].

2. *Fundamentals of Tribology (Friction, Wear, Lubrication)*, Ed. by A. V. Chichinadze (Mashinostroenie, Moscow, 1995) [in Russian].

3. F. M. Borodich and I. V. Kryukova, Pis'ma Zh. Tekh. Fiz. **23** (6), 67 (1997) [Tech. Phys. Lett. **23**, 239 (1997)].

4. G. X. Chen and Z. R. Zhou, Wear **255**, 376 (2003).

5. Yu. A. Fadin, A. M. Leksovskiĭ, B. M. Ginzburg, and V. P. Bulatov, Pis'ma Zh. Tekh. Fiz. **19** (5), 10 (1993) [Tech. Phys. Lett. **19**, 136 (1993)].

6. V. E. Rubtsov and A. V. Kolubaev, Zh. Tekh. Fiz. **74** (11), 63 (2004) [Tech. Phys. **49**, 1457 (2004)].

7. T. Jibiki, M. Shima, H. Akita, and M. Tamura, Wear **251**, 1492 (2001).

8. B. P. Gritsenko, K. V. Krukovskiĭ, and O. A. Kashin, Fiz. Mezomekh., Special Issue, Chap. 1, 415 (2004).

9. L. G. Korshunov, I. N. Bogachev, Yu. I. Averin, *et al.*, Fiz. Met. Metalloved. **49** (1), 113 (1980).

10. L. G. Korshunov, Fiz. Met. Metalloved. **73** (8), 3 (1992).

Translated by P. Pozdeev

Cross Sections for Surface Plasmon Polariton Scattering from a Nanoparticle in the Dipole Approximation

A. B. Evlyukhin

Vladimir State University, Vladimir, Russia
e-mail: a.b.evlyukhin@mail.ru
Revised manuscript received April 14, 2005

Abstract—The differential and total cross sections for the scattering of surface electromagnetic waves in the optical frequency range (surface plasmon polaritons, SPPs) from a small particle into waves in the near-field zone (SPPs) and into waves propagating from the surface to the far-field zone have been calculated within the framework of the dipole approximation. The efficiencies of these scattering channels are compared as dependent on the main parameters of the system. An increase in the wavelength of the radiation exciting SPPs at a plane dielectric–metal interface (air–gold) may lead to a change in the most effective scattering channel. © 2005 Pleiades Publishing, Inc.

In recent years, much attention has been devoted to investigations of the properties of surface electromagnetic waves in the optical frequency range, which are excited at the interface between a dielectric and a metal. Since the excitation of these waves involves free charge carriers of the metal, they are frequently called surface plasmon polaritons (SPPs) [1, 2]. The exponential localization of SPPs at the surface and their high sensitivity to surface inhomogeneities make SPPs a unique signal source for near-field microscopy. Indeed, an SPP propagating along a flat surface and meeting a local nanodimensional inhomogeneity (surface defect, artificial nanostructure, biological object, etc.) exhibits scattering and, hence, by monitoring the pattern of distribution of the resulting electromagnetic field, one can obtain information about the properties of the scatterer.

The SPP scattering can proceed via two main channels: (i) the elastic scattering of SPPs into SPPs and (ii) the scattering of SPPs into waves propagating from the surface to a far-field zone. Both these channels, either separately or jointly, can be considered as sources of information about the scatterer. If the scattered SPP distribution serves the source of information, the second channel is considered as undesired because it implies the loss of energy from the SPP channel. In contrast, monitoring of the response signal in the far-field zone poses the problem of minimizing the elastic SPP scattering probability. Which one of the two possible modes is optimal depends on the specific features of interactions of the surface object and the probe with SPPs. Therefore, expanding the possibilities of the SPP microscopy, including its resolving power, requires a deeper insight into features of the process of SPP scattering related to the configuration (mutual arrangement of scatterers and the surface with SPPs) and material parameters of the system.

From the theoretical standpoint, this is a rather complicated problem, because even the relatively simple case of a single symmetric scatterer requires using numerical methods [3]. However, taking into account that the dimensions of objects studied in the near-field microscopy as well as those of a probe (made as small as possible in order to increase resolution) are frequently much smaller than the SPP wavelength, the description of SPP scattering in many cases [4] can be restricted to the dipole approximation. This approach significantly simplifies the problem and allows a solution to be obtained in the analytical form.

This Letter presents the results of calculations of the differential and total cross sections for the SPP scattering from a small particle for the two mechanisms of scattering considered in the dipole approximation. The efficiencies of the two scattering channels are compared as functions of the main parameters of the system.

The calculations are performed using the method of Green's tensor function for a system comprising two half-spaces filled with a dielectric medium and a metal with the relative permittivities ε_r and ε_m, respectively, such that $(-\varepsilon_m) > \varepsilon_r$ (this is a necessary condition for the existence of SPPs). The permittivity of the metal is assumed to be real, which considerably simplifies obtaining the main results and is close to real experimental situations. For the noble metals (gold, silver, etc.), which are most frequently used in the experiments with SPPs, the SPP decay length related to ohmic losses is several orders of magnitude greater than the SPP wavelength [2]. This circumstance is related to the small value of the imaginary part of the permittivity. The time dependence will be described by the harmonic function $\exp(-i\omega t)$, where ω is the cyclic frequency of SPPs.

The physical system also includes a small spherical particle with the volume $V_p = 4\pi R_p^3/3$ centered at a point with the radius vector $\mathbf{r}_p$ and the Cartesian coordinates $(0, 0, z_p)$ on the dielectric side. The particle is situated over the metal surface, which coincides with the $z = 0$ plane (the z axis is directed from metal to dielectric). The particle radius is assumed to be much shorter than the SPP wavelength and than the distance to the surface ($z_p \gg R_p$). The particle has the permittivity ε_p.

Consider an external plane SPP wave propagating in the positive direction of the x axis, which is incident on the particle and is scattered from it. Using the method of Green's tensor function of the wave equation, the electric field strength $\mathbf{E}_{sc}$ of the scattered wave at an arbitrary point $\mathbf{r}$ outside the scattering particle can be described in the dipole approximation as

$$\mathbf{E}_{sc}(\mathbf{r}) = \frac{k_0^2}{\varepsilon_0}\hat{G}_0(\mathbf{r}, \mathbf{r}_p)\hat{\alpha}_d\mathbf{E}_0(\mathbf{r}_p), \tag{1}$$

where ε_0 is the permittivity of vacuum, k_0 is the wavenumber in vacuum corresponding to the frequency ω, $\mathbf{E}_0$ is the electric field vector in the incident SPP wave [5, 6], $\hat{G}_0(\mathbf{r}, \mathbf{r}')$ is Green's tensor function of the system under consideration in the absence of the scattering particle, and $\hat{\alpha}_d$ is the particle polarizability tensor with allowance for the influence of the metal surface. For a small spherical particle, the polarizability can be expressed as [4, 5]

$$\hat{\alpha}_d = \alpha_0\left(\frac{1}{1 + \xi\beta}\hat{x}\hat{x} + \frac{1}{1 + \xi\beta}\hat{y}\hat{y} + \frac{1}{1 + 2\xi\beta}\hat{z}\hat{z}\right), \tag{2}$$

where $\alpha_0 = \varepsilon_0\varepsilon_r V_p 3(\varepsilon_p - \varepsilon_r)/(\varepsilon_p + 2\varepsilon_r)$ is the electrostatic polarizability of the particle in a homogeneous medium with the permittivity ε_r (the permittivities are frequency dependent); $\beta = (R_p/(2z_p))^3$; $\xi = [(\varepsilon_r - \varepsilon_m)(\varepsilon_p - \varepsilon_r)]/[(\varepsilon_r + \varepsilon_m)(\varepsilon_p + 2\varepsilon_r)]$; and $\hat{x}$, $\hat{y}$, $\hat{z}$ are the unit vectors of the Cartesian coordinate system.

In order to assess the efficiency of SPP scattering into SPP as compared to the scattering into waves propagating from the surface to the far-field zone, we may consider Eq. (1) with Green's tensor written in the far-field zone approximation and represent it as a sum of two parts, $\hat{G}_S(\mathbf{r}, \mathbf{r}')$ and $\hat{G}_T(\mathbf{r}, \mathbf{r}')$, where $\hat{G}_S(\mathbf{r}, \mathbf{r}')$ is the Green's tensor part describing excitations in the SPP system and $\hat{G}_T(\mathbf{r}, \mathbf{r}')$ is the tensor part describing electromagnetic waves propagating from the metal surface to the dielectric medium with the permittivity ε_r. Then, Eq. (1) written with only one part of Green's tensor gives the electric field vector in the corresponding scat-

tered wave. Using the known analytical representations for $\hat{G}_S(\mathbf{r}, \mathbf{r}')$ [6] and $\hat{G}_T(\mathbf{r}, \mathbf{r}')$ [7], we can determine the electric field strength in the corresponding wave. The corresponding magnetic fields can be determined from Maxwell's equations. The process of SPP scattering into SPPs is conveniently described using the cylindrical coordinates (ρ, φ, z). The scattering into waves propagating away from the surface is more conveniently described using the spherical coordinates (r, φ, θ), where θ and φ are the polar and azimuthal angle, respectively.

The differential scattering cross section is defined as the ratio of the time-average flux of electromagnetic energy in a given direction to the average energy flux in the incident SPP wave per unit length in the direction perpendicular to the direction of incidence. The total cross section is obtained by integrating the differential cross section over all scattering angles. According to these definitions, the differential and total cross sections for the SPP scattering into SPPs are given by the following expressions:

$$\sigma_p(\varphi) = \frac{k_0^4 k_s(-\varepsilon_m)^5\varepsilon_r(1 + \eta_p\cos\varphi)^2}{2\pi\varepsilon_0^2(\varepsilon_m - \varepsilon_r)^2(\varepsilon_m + \varepsilon_r)^4} \times \left(\frac{\alpha_0}{1 + 2\xi\beta}\right)^2 e^{-4ak_sz_p}, \tag{3}$$

$$\sigma_{scat}^{spp} = \frac{k_0^4 k_s(-\varepsilon_m)^5\varepsilon_r(2 + \eta_p^2)}{2\varepsilon_0^2(\varepsilon_m - \varepsilon_r)^2(\varepsilon_m + \varepsilon_r)^4}\left(\frac{\alpha_0}{1 + 2\xi\beta}\right)^2 e^{-4ak_sz_p}, \tag{4}$$

where φ is the angle determining the scattering direction in the cylindrical coordinate system, $k_s = k_0\sqrt{\varepsilon_r\varepsilon_m/(\varepsilon_r + \varepsilon_m)}$ is the SPP wavevector, $a = \sqrt{\varepsilon_r/-\varepsilon_m}$, and $\eta_p = a^2(1 + 2\xi\beta)/(1 + \xi\beta)$.

In calculating the scattering cross sections for the second mechanism, we can take into account that the electromagnetic field in the far zone is transverse and, hence, the amplitudes of the electric and magnetic fields are related to the wave impedance of the homogeneous medium with the permittivity ε_r. Then, the differential cross section for SPP scattering into waves propagating away from the metal surface can be written as

$$\sigma_{space}(\varphi, \theta) = \frac{2k_r a}{(1 - a^2)(1 - a^4)}|\mathbf{E}_{sc}|^2 r^2, \tag{5}$$

where $k_r = k_0\sqrt{\varepsilon_r}$ and r is the distance from the origin to the point of observation. The total cross sections for

waves of the two types of polarization are given by the expressions

$$\sigma_{scat}^{(s)} = \int_0^{2\pi}\int_0^{\pi/2} \frac{2k_r a|E_\varphi(r, \varphi, \theta)|^2}{(1-a^2)(1-a^4)} r^2 \sin\theta \, d\varphi \, d\theta; \quad (6)$$

$$\sigma_{scat}^{(p)} = \int_0^{2\pi}\int_0^{\pi/2} \frac{2k_r a|E_\theta(r, \varphi, \theta)|^2}{(1-a^2)(1-a^4)} r^2 \sin\theta \, d\varphi \, d\theta. \quad (7)$$

Here, the electric vector components in the scattered wave field are determined from Eq. (1):

$$E_\varphi(r, \varphi, \theta) = \frac{i \, k_0^2}{a \, \varepsilon_0} \frac{\alpha_0}{1+2\xi\beta}\eta_p$$

$$\times \sin\varphi (1 + r^{(s)}e^{ik_r 2z_p\cos\theta})\frac{e^{ik_r r}}{4\pi r}e^{-ak_s z_p - ik_r z_p\cos\theta}; \quad (8)$$

$$E_\theta(r, \varphi, \theta) = -\frac{k_0^2}{\varepsilon_0}\frac{\alpha_0}{1+2\xi\beta}\left\{\frac{i}{a}\eta_p\cos\varphi\cos\theta\right.$$

$$\times (1 - r^{(p)}e^{ik_r 2z_p\cos\theta}) + \left.\sin\theta(1 + r^{(p)}e^{ik_r 2z_p\cos\theta})\right\} \quad (9)$$

$$\times \frac{e^{ik_r r}}{4\pi r}e^{-ak_s z_p - ik_r z_p\cos\theta},$$

where $r^{(p)}$ and $r^{(s)}$ are the reflection coefficients for the two types of polarization, which can be found in [6].

Using the obtained results, we can compare the efficiencies of two scattering channels for certain sets of parameters of the system under consideration. Let us consider the case when the substrate is made of gold [8] and the scattering particle is either metal or dielectric. As can be seen from the results of calculations presented in Fig. 1, the total cross section for the SPP excited by light with a wavelength of 800 nm and scattered into SPPs can exceed the cross section for the SPPs scattered into waves propagating from the metal surface to the far-field zone for both metal and dielectric particles. As the distance from the scatterer to the metal surface increases, the difference between the cross sections of scattering into two channels decreases. When the particle contacts with the metal surface, the cross sections sharply increase as a result of their interaction. However, in this case, the dipole approximation is insufficient [4] and the description of scattering must take into account the contributions due to higher multipoles.

An increase in the wavelength of the radiation exciting SPPs is accompanied by a growth in the permittiv-
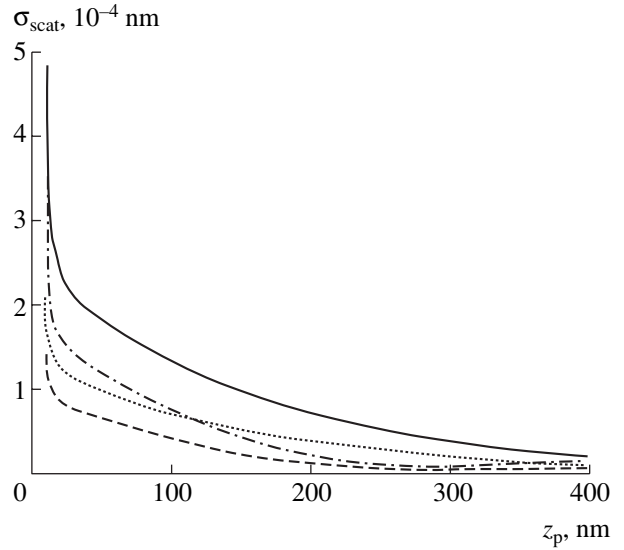

Fig. 1. Total cross sections of SPP scattering versus the distance z_p from the surface to the scatterer—a spherical particle with the radius $R_p = 10$ nm: (solid curve) σ_{scat}^{spp} for $\varepsilon_p = -26.3$; (dash–dot curve) $\sigma_{scat}^{(s)} + \sigma_{scat}^{(p)}$ for $\varepsilon_p = -26.3$; (dotted curve) σ_{scat}^{spp} for $\varepsilon_p = 15$; (dashed curve) $\sigma_{scat}^{(s)} + \sigma_{scat}^{(p)}$ for $\varepsilon_p = 15$. The calculation was performed for $\lambda = 800$ nm, $\varepsilon_m = -26.3$, and $\varepsilon_r = 1$.
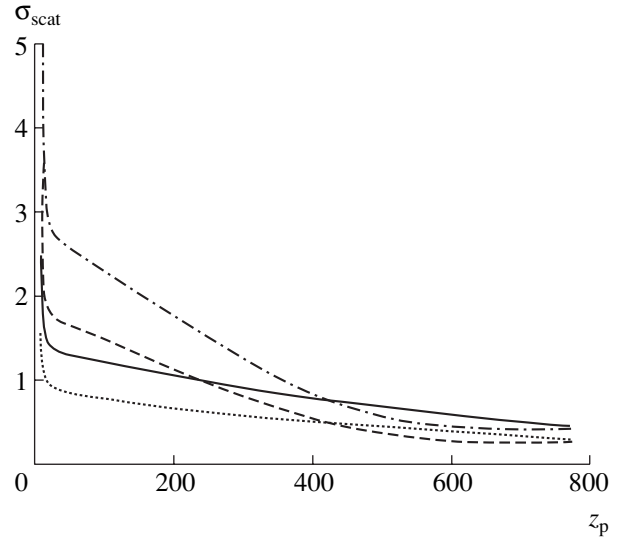

Fig. 2. Total cross sections of SPP scattering versus the distance z_p from the surface to the scatterer—a spherical particle with the radius $R_p = 10$ nm: (solid curve) σ_{scat}^{spp} for $\varepsilon_p = -132$; (dash–dot curve) $\sigma_{scat}^{(s)} + \sigma_{scat}^{(p)}$ for $\varepsilon_p = -132$; (dotted curve) σ_{scat}^{spp} for $\varepsilon_p = 15$; (dashed curve) $\sigma_{scat}^{(s)} + \sigma_{scat}^{(p)}$ for $\varepsilon_p = 15$. The calculation was performed for $\lambda = 1550$ nm, $\varepsilon_m = -132$, and $\varepsilon_r = 1$.

ity modulus of gold, which leads to a change in the ratio of the cross sections for the two channels (Fig. 2). At a relatively small distance from the scatterer to the surface, the cross section of scattering into waves propagating away from the metal surface exceeds that for the scattering into SPPs irrespective of the permittivity of the scattering particle. Thus, a comparison of the curves presented in Figs. 1 and 2 leads to an important conclusion: by changing the wavelength of the exciting radiation, it is possible to control the relative efficiency of different channels for the SPP scattering from a small particle at the surface featuring SPPs. This conclusion has direct implementations in the SPP near-field microscopy, since it helps select the optimum regimes of measurements depending on the parameters of experiment. In conclusion, it should be noted that the limits of applicability of the dipole approximation to the problems of SPP scattering have been recently considered in detail in [4].

REFERENCES

1. A. V. Zayats and I. I. Smolyaninov, J. Opt. A: Pure Appl. Opt. **5**, S16 (2003).

2. W. L. Barnes, A. Dereux, and T. W. Ebbesen, Nature **424**, 824 (2003).

3. A. V. Shchegrov, I. V. Novikov, and A. A. Maradudin, Phys. Rev. Lett. **78**, 4269 (1997).

4. A. B. Evlyukhin and S. I. Bozhevolnyi, Pis'ma Zh. Éksp. Teor. Fiz. **81**, 278 (2005) [JETP Lett. **81**, 218 (2005)].

5. T. Sondergaard and S. I. Bozhevolnyi, Phys. Rev. B **67**, 165405 (2003).

6. T. Sondergaard and S. I. Bozhevolnyi, Phys. Rev. B **69**, 045422 (2004).

7. L. Novotny, J. Opt. Soc. Am. A **14**, 105 (1997).

8. *Handbook of Optical Constants of Solids*, Ed. by E. D. Palik (Academic, New York, 1985).

Translated by P. Pozdeev

Application of the Kirchhoff Method
to the Problem of Wave Diffraction on a Ribbon
at Small Sliding Incidence Angles

P. N. Dagurov* and A. V. Dmitriev

*Department for Physical Problems, Buryatian Scientific Center, Siberian Division, Russian Academy of Sciences,
Ulan-Ude, Buryatia, Russia*

* e-mail: dpn@ofpsrv.bsc.buryatia.ru

Received May 4, 2005

Abstract—A new approach to the problem of electromagnetic wave diffraction on a conducting ribbon at small sliding incidence angles is developed within the framework of the Fresnel–Kirchhoff method. The wave diffraction in this system has been theoretically and experimentally studied using the proposed method. The experimental data agree with the results of theoretical analysis. © 2005 Pleiades Publishing, Inc.

The problem of electromagnetic wave diffraction on a conducting ribbon (or a supplementary problem of wave diffraction on a slit) is among the classical diffraction problems which have been extensively studied. Strict and asymptotic approaches to the solution of this problem are offered by the method of separation of variables and the method of integral equations [1–4], the method of edge waves [5], and the geometric theory of diffraction [5]. In addition, a simple and clear approximate solution, which is frequently used in practice, can be obtained using the Kirchhoff method or the method of physical optics. In the case of application of the standard Kirchhoff method, the field behind a body (ribbon) on which the diffraction takes place is independent of the polarization and is determined by the projection of this body onto the wave front surface. Thus, the diffraction fields behind bodies having different shapes, but the same projections are indistinguishable. Another conclusion is that a wave incident at a small glancing angle will not "see" the ribbon.

We propose a new approach to the solution of the problem of electromagnetic wave diffraction on a conducting ribbon at small sliding incidence angles. The Kirchhoff theory in its standard formulation does not cover this angular interval. The proposed method is based on a consistent application of the Huygens–Fresnel principle and the method of mirror images with allowance for the wave polarization.

Figure 1 shows the geometry of the problem under consideration. A conducting ribbon with a width of $a = d_2$ is situated between elementary dipole A and the point of observation B. The ribbon occurs in the plane $y = 0$ and its edges have the coordinates $z = d_1$ and $d_1 + d_2$. The coordinates of the radiator (y_0) and the detector (y_3) are

assumed to obey the conditions $y_0 \ll d_1$ and $y_3 \ll d_3$. In order to find the field at point B, consider the planes S_1 and S_2 containing the ribbon edges, which are described by the equations $z = d_1$ and $z = d_1 + d_2$. According to the Huygens–Fresnel principle, the field $U(B)$ at point B is determined as the total sum of waves coming from all Huygens' point sources occurring in the S_2 plane. In turn, the field $U(P_2)$ at a current point P_2 in the S_2 plane is equal to the total sum of waves coming from all Huygens' point sources occurring in the S_1 plane, with allowance for the influence of the ribbon. In order to determine this influence, let us use the method of mirror images (essentially, the Kirchhoff method, since we ignore the edge effects). Thus, the influence of the ribbon is modeled by introducing the mirror source P_1^*. The field at a current point P_1 in the S_1 plane is, according to the Kirchhoff approximation, equal to a source field in free space.
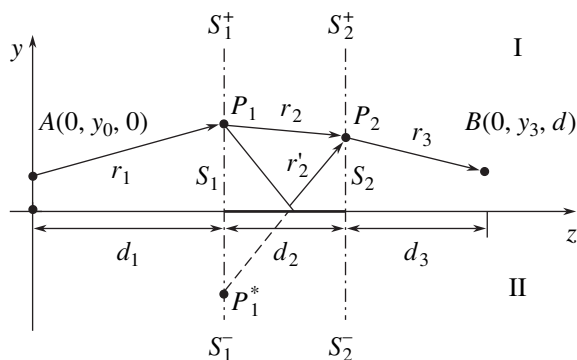

Fig. 1. Geometry of the problem under consideration (see the text for explanations).

The field at point B can be written in terms of the Rayleigh–Sommerfeld integral:

$$U(B) = -\frac{1}{2\pi}\int\limits_{S_2} U(P_2)\frac{\partial G_2}{\partial n_2}dS_2, \qquad (1)$$

where $k = 2\pi/\lambda$ is the wavenumber, λ is the wave length, n_2 is outward normal to the S_2 plane, and $G_2 = \exp(ikr_3)/r_3$ is Green's function.

In view of the smallness of y_0 and y_3 values, the field U is assumed to be approximately equal either to the electric field component E_x (for a horizontal dipole) or E_y (for a vertical dipole). Sequentially using formula (1), we obtain an expression for the field at point B:

$$U(B) = \frac{1}{4\pi^2}\left(\iint\limits_{S_1^+ S_2^+} + \iint\limits_{S_1^- S_2^-}\right)U(P_1)\frac{\partial G_1}{\partial n_1}\frac{\partial G_2}{\partial n_2}dS_1 dS_2, \quad (2)$$

where $U(P_1) = \exp(ikr_1/)r_1$ is the field at the current point P_1 in the S_1 plane; $G_1 = \exp(ikr_2)/r_2 + \Phi\exp(ikr_2')/r_2'$; S_1^+, S_2^+ and S_1^-, S_2^- are the half-planes situated above and below the plane $y = 0$, respectively.

Assuming that kr_1, kr_2, $kr_3 \gg 1$, we obtain an approximate formula

$$U(B) = -\left(\frac{k}{2\pi}\right)^2 \int\limits_{-\infty}^{\infty}\int\limits_{-\infty}^{\infty} dx_1 dx_2 \left[\left(\int\limits_{-\infty}^{0}\int\limits_{-\infty}^{0} + \int\limits_{0}^{\infty}\int\limits_{0}^{\infty}\right)\right.$$

$$\times\left(\frac{\exp[ik(r_1 + r_2 + r_3)]}{r_1 r_2 r_3}\right. \qquad (3)$$

$$\left.\left. + \Phi\frac{\exp[ik(r_1 + r_2' + r_3)]}{r_1 r_2' r_3}\right)dy_1 dy_2\right].$$

Expanding in this expression r_1, r_2, r_2', and r_3 into series, restricting the expansion to the square terms in the exponents (Fresnel's diffraction), putting $r_1 \approx d_1$, $r_2 \approx d_2$, and $r_3 \approx d_3$ in the amplitude factors, integrating with respect to x_1 and x_2, and accomplishing algebraic transformations, we arrive at the following formula:

$$U(B) = \frac{\exp(ikr)}{d}P(h_1, h_2, -\beta)$$

$$+ \frac{\exp(ikr')}{d}\Phi P(h_1', h_2', \beta), \qquad (4)$$

where

$$r \approx d + (y_0 - y_3)^2/2d, \quad r' \approx d + (y_0 + y_3)^2/2d,$$

$$\beta = \sqrt{d_1 d_3/[(d_1 + d_2)(d_2 + d_3)]}, \quad d = \sum_{i=1}^{3} d_i;$$

$$h_1 = \frac{y_0(d_2 + d_3) + y_3 d_1}{d}\left[\frac{\pi(d_1 + d_2)}{\lambda d_1 d_2}\right]^{1/2},$$

$$h_2 = \frac{y_3(d_1 + d_2) + y_0 d_3}{d}\left[\frac{\pi(d_2 + d_3)}{\lambda d_2 d_3}\right]^{1/2},$$

$$h_1' = \frac{y_0(d_2 + d_3) - y_3 d_1}{d}\left[\frac{\pi(d_1 + d_2)}{\lambda d_1 d_2}\right]^{1/2},$$

$$h_2' = \frac{y_3(d_1 + d_2) - y_0 d_3}{d}\left[\frac{\pi(d_2 + d_3)}{\lambda d_2 d_3}\right]^{1/2}.$$

$$P(a_1, a_2, \pm\beta) = 1 - F(\sqrt{1 - \beta^2}a_1) - F(\sqrt{1 - \beta^2}a_2)$$

$$+ 2[G(a_1 \pm \beta a_2, \sqrt{1 - \beta^2}a_2)$$

$$+ G(a_2 \pm \beta a_1, \sqrt{1 - \beta^2}a_1)],$$

$F(x) = \int_0^\infty \exp(it^2)dt$ is the Fresnel integral, and $G(x, y) = (y/2\pi)\int_x^\infty \exp[i(t^2 + y^2)]/(t^2 + y^2)dt$ is the generalized Fresnel integral [6].

An analysis of formula (4) shows that, for example, in the case of glancing incidence (where $y_0 = y_3 = 0$ and, accordingly, $h_1 = h_2 = h_1' = h_2' = 0$)

$$U(B) = \frac{\exp(ikd)}{d}\left\{\left(\frac{1}{2} + \frac{1}{\pi}\arctan\frac{\beta}{\sqrt{1 - \beta^2}}\right)\right.$$

$$\left. + \Phi\left(\frac{1}{2} - \frac{1}{\pi}\arctan\frac{\beta}{\sqrt{1 - \beta^2}}\right)\right\}. \qquad (5)$$

If the electric field strength is perpendicular to the ribbon plane, the reflection coefficient is $\Phi = 1$ and $U(B) = \exp(ikd)/d$, which means that the wave does not "see" the ribbon.

When the wave is polarized parallel to the ribbon edges, we have $\Phi = -1$ and

$$U(B) = \frac{\exp(ikd)}{d}\frac{2}{\pi}\arctan\frac{\beta}{\sqrt{1 - \beta^2}}$$

$$= \frac{\exp(ikd)}{d}\frac{2}{\pi}\arctan\sqrt{\frac{d_1 d_3}{d_2 d}} \qquad (6)$$

$$= \frac{\exp(ikd)}{d}\left(1 - \frac{2}{\pi}\arctan\sqrt{\frac{d_2 d}{d_1 d_3}}\right).$$

For $d_2 = 0$, the primary field is $U(B) = \exp(ikd)/d$. Therefore, formula (6) correctly describes the field in the absence of the ribbon, although it was derived assuming that $d_2 \gg \lambda$.

Let the ribbon to extend in the z direction from radiator to the detector, in which case $d_1 = d_3 = 0$ and $d_2 = d$. Then, formula (6) yields $U(B) = 0$ and, hence, still adequately describes the situation.

Formula (4) shows that, when the source and the detector (observation point) do not occur in the ribbon plane and $d_1 = d_3 = 0$ and $d_2 = d$, the field at point B is equal to the sum of a direct wave and that reflected from an infinite plane when both radiation and detection points are situated above or below the ribbon plane, and $U(B) = 0$ when the radiation and detection points are situated on the opposite sides from the ribbon plane.

We have performed experimental verification of the above theory by measuring the diffraction from a ribbon at a wavelength of $\lambda = 0.03$ m. The experimental arrangement was as follows: a conducting (duralumin) 5×10^{-4} m thick ribbon was vertically suspended above a flat horizontal metal surface, so that the bottom edge of the ribbon with a length of d_2 touched the metal surface. The radiating and receiving antennas had the form of vertical grounded quarter-wave dipoles, so that the radiation was polarized parallel to the ribbon edges and the reflection coefficient was $\Phi = -1$. The size of the horizontal metal surface (i.e., of the "mirror" screening the bottom half-space) was sufficiently large to avoid the edge effects. In interpreting the experimental results, we assumed that the method of mirror images is applicable and the experimental conditions correspond to those in the free space for a ribbon and vibrators of double lengths. In our experiments, the ribbon length was 1 m and could be considered as infinite. The horizontal metal surface had the dimensions of 1×1 m.

Figure 2 shows experimental plots of the diffraction field intensity (normalized to that in the absence of the ribbon) versus the detector coordinate y_3 for $d_1 = d_3 = 0.42$ m, $d_2 = 0.063$ m, and $y_0 = 0.15$ m. For comparison,
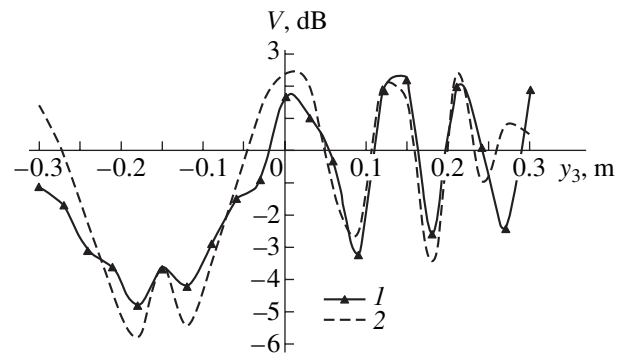

Fig. 2. Comparison of the (*1*) experimental and (*2*) calculated profiles of the diffraction field intensity.

Fig. 2 also presents the results of calculations using formula (4). As can be seen, the experimental and theoretical curves are in good agreement, which confirms the correctness of the proposed method of solution of the diffraction problem.

REFERENCES

1. H. Hönl, A. W. Maue, and K. Westpfahl, in *Handbuch der Physik* (Springer, Berlin, 1961; Mir, Moscow, 1964).

2. E. I. Nefedov and A. T. Fialkovskiĭ, *Asymptotic Diffraction Theory of Electromagnetic Waves on Finite Structures* (Nauka, Moscow, 1972) [in Russian].

3. M. D. Khaskind and L. A. Vaĭnshteĭn, Radiotekh. Élektron. (Moscow), No. 10, 1800 (1964).

4. S. I. Éminov, Pis'ma Zh. Tekh. Fiz. **29** (16), 80 (2003) [Tech. Phys. Lett. **29**, 694 (2003)].

5. P. Ya. Ufimtsev, *Method of Edge Waves in Physical Diffraction Theory* (Sov. Radio, Moscow, 1962) [in Russian].

6. V. A. Borovikov and B. E. Kinber, *Geometrical Theory of Diffraction* (Svyaz', Moscow, 1978) [in Russian].

Translated by P. Pozdeev

Output Radiation Focusing
in Curved-Grating Distributed Bragg Reflector Laser

G. S. Sokolovskii[a,*], V. V. Dudelev[a], I. M. Gadzhiev[a], S. N. Losev[a],
A. G. Deryagin[a], V. I. Kuchinskii[a], E. U. Rafailov[a], and W. Sibbett[b]

[a] *Ioffe Physicotechnical Institute, Russian Academy of Sciences, St. Petersburg, 194021 Russia*
[b] *School of Physics and Astronomy, University of St. Andrews, St. Andrews KY 169SS, United Kingdom*
* e-mail: gs@mail.ioffe.ru

Abstract—Output radiation focusing in AlGaAs/GaAs quantum-well curved-grating distributed Bragg reflector (c-DBR) lasers has been theoretically and experimentally studied. It is established that the focal spot size for c-DBR lasers is determined to a considerable extent by the spectral perfection of laser radiation. © 2005 Pleiades Publishing, Inc.

Recent achievements in the development of semiconductor lasers—small sources of coherent radiation—have considerably expanded their field of application in science and technology. Prominent examples are offered by fiber-optic communications, photomedicine, and pumping of fiber-optic amplifiers, solid-state lasers, and nonlinear crystals. However, the needs of these and many other applications are still incompletely satisfied, since they require well-focused single-mode high power laser radiation.

The task of obtaining high-power semiconductor lasers with focused output radiation reduces to ensuring a perfect spatial distribution of laser radiation. This can be achieved, in particular, by creating laser structures with narrow (about 5 μm wide) stripes. Such lasers provide an output power of 100–200 mW in a single-mode regime under continuous pumping conditions [1, 2]. The best lasers of this type can provide an output power on the order of 500 mW, which is close to the threshold of catastrophic degradation or overheating of their mirrors [3]. Other approaches to meeting the contradictory requirements of high output power and spatial perfection of laser radiation are related to the use of laser arrays with narrow stripes and phase-shifted pumping [4], unstable-resonator lasers [5], and master oscillator power amplifiers (MOPAs) with discrete or integrated optics design [6]. Among these, only MOPAs can provide an output power above 1 W with a spatial divergence determined by the diffraction limit. Unfortunately, the MOPA technology is highly complicated and poses considerable limitations on the possible applications of such devices.

This Letter presents the development of a previously formulated idea [7, 8] concerning radiation focusing in a curved-grating distributed Bragg reflector (c-DBR) laser. In this device, the curved grating imparts cylindrical symmetry to the output radiation, thus ensuring focusing of all laser modes in a common focus in the plane of the p–n junction (Fig. 1a). At the same time, the Bragg reflector acts as a spectral filter ensuring stable single-mode lasing, while a large (100 μm and above) stripe width removes power limitations inherent in most narrow-stripe structures.

In the course of theoretical analysis, we have considered three factors determining the focal spot size for c-DBR lasers (Fig. 1b):

(i) "Paraxial" focusing of laser radiation due to the cylindrical symmetry of the c-DBR resonator, which is readily described in the thin lens approximation and determined by numerical aperture of the device, that is, by the ratio of the focal length to the output mirror width. In this approximation, the focal spot size w_p is given by the formula

$$w_p = \frac{\lambda}{2NA},\qquad(1)$$

where λ is the laser wavelength and NA is the numerical aperture defined as a half of the ratio of the output mirror width to the focal length.

(ii) "Nonparaxial" smearing of the focus as a result of refraction of the cylindrical laser beam on a flat output mirror. This factor becomes significant for nonparaxial rays (i.e., beyond the thin lens approximation [8, 9]). The magnitude of this smearing, w_q, is proportional to the square of the numerical aperture:

$$w_q \approx \frac{W_1}{2}NA^2,\qquad(2)$$

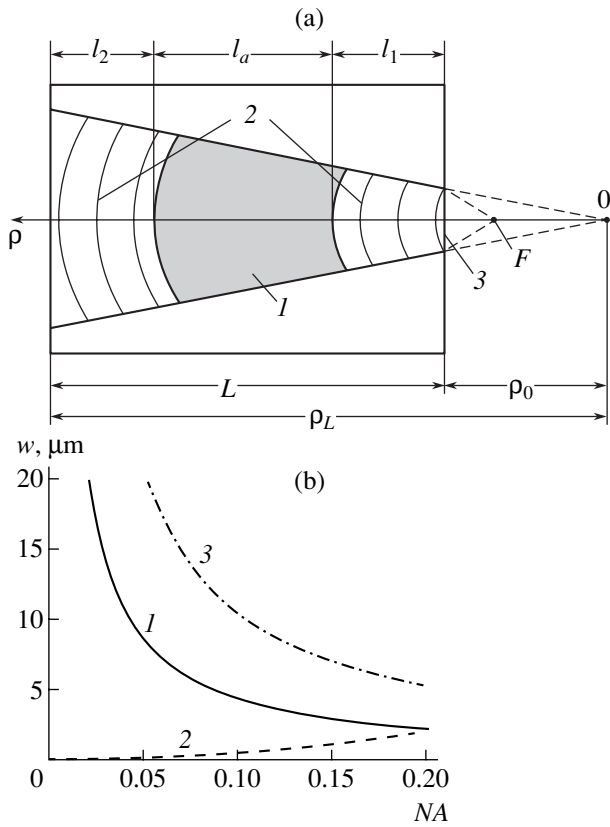where W_1 is the output mirror width.

Fig. 1. (a) Schematic diagram of a c-DBR laser: (*1*) active region; (*2*) curved grating; (*3*) output mirror. (b) The results of theoretical calculations of the focal spot size *w* versus numerical aperture *NA* for a c-DBR laser with $\delta\lambda = 0.1$ nm showing the effects of (*1*) "paraxial" focusing, (*2*) "non-paraxial" smearing due to refraction of a cylindrical ray on the flat output mirror, and (*3*) "spectral" focusing.

Fig. 2. Near-field intensity distributions observed below and above the threshold for a c-DBR laser with $W_1 = 100$ μm and a focal length of 0.8 mm for pumping (a) below and (b) above the laser threshold.

(iii) Focusing of the output radiation due to the spectral selectivity of the curved grating. The physical meaning of this effect can be illustrated by comparing c-DBR lasers to the usual DBR lasers, in which a difference in the divergence of various modes in a wide stripe results in each mode having its own curvature of the wave front (significantly different from that for the fundamental mode). In the case of a c-DBR laser, the curvature of the wave front is determined by a cylindrical symmetry of the resonator and is the same for all modes. "Noncylindrical" ray propagation in the c-DBR resonator implies variation of the effective Bragg period of the cylindrical grating along the ray and, hence, leads to a spectral broadening of the laser line. This spectral broadening depends on the length and curvature of the grating and on the angle between the direction to the center of symmetry and the direction of propagation of the "slightly noncylindrical" ray. On the other hand, the spectral broadening is limited by the spectral selectivity of the c-DBR grating [10, 11]. A comparison of the spectral broadening due to the noncylindrical propagation and the spectral selectivity of the DBR resonator allows the focal spot size caused by
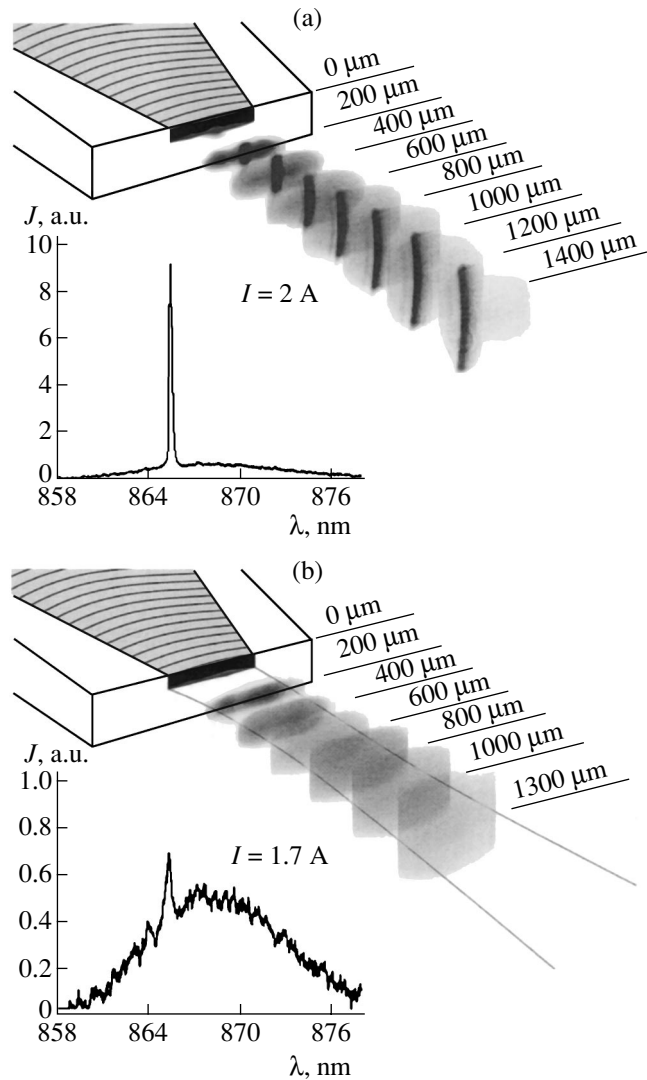
the "spectral" focusing to be theoretically calculated as

$$w_s \approx \frac{nW_1}{NA}\sqrt{\frac{2\delta\lambda}{\lambda}}, \qquad (3)$$

where $\delta\lambda$ is the laser linewidth and n is the effective refractive index of the laser waveguide.

Figure 1b shows the values of the focal spot size calculated using formulas (1)–(3) as function of the numerical aperture for a c-DBR laser with $\delta\lambda = 0.1$ nm, $W_1 = 100$ μm, and $\lambda = 860$ nm. As can be seen from these data, the nonparaxial smearing of the focus at small *NA* values is small as compared to the contributions due to the two other factors. On the other hand, the influence of the laser linewidth via the "spectral" focusing mechanism remains significant even at large *NA*

values. From this we may conclude that a minimum focal spot size can be achieved in c-DBR lasers with large curvature of the grating (optimum *NA*) and narrow laser line (minimum $\delta\lambda$).

We have experimentally studied c-DBR lasers based on AlGaAs/GaAs structures with two quantum wells ($\lambda = 860$ nm). The active region had the form of a tapered stripe with an output mirror width of $W_1 = 100$ μm. Curved distributed reflectors in the form of a third-order diffraction grating with a 385-nm period were created on the structure surface using electron-beam lithography and ion-bean etching to a depth of 0.6 μm (coupling coefficient, $\kappa = 17.5$ cm^{-1}) [9]. The curvature radius of the gratings was varied from 0.7 to 10 mm, which corresponded to a change in the focal length from 0.2 to 2.8 mm. The total laser length, including the two Bragg reflectors and the active region, was about 1.5 mm. The cleaved mirrors were provided with antireflection coatings in order to suppress the Fabry–Perot modes and filamentation. The c-DBR laser wavelength was 867 nm. The threshold currents varied within 1.2–1.5 A depending on the Bragg reflector curvature (i.e., on the area of the pumped region). High values of the threshold current are explained by a large area of the pumped region and by absorption in the c-DBR regions.

Figure 2 shows the near-field intensity distributions observed below and above the threshold for a c-DBR laser with $W_1 = 100$ μm and a focal length of 0.8 mm. As can be seen, the focal spot size in the case of a narrow laser line is about 20 μm, while broadband radiation generated near the threshold can be focused only to 80 μm. These examples illustrate the role of the "spectral" focusing mechanism in c-DBR lasers.

In conclusion, we have theoretically and experimentally studied the features of output radiation focusing in c-DBR lasers and established that the focal spot size in c-DBR lasers is determined to a considerable extent by the spectral perfection of laser radiation. We believe that an increase in the numerical aperture and a decrease in the size of unpumped region (due to increased coupling of curved Bragg reflectors) will provide an additional decrease in the focal spot size and an increase in the efficiency of c-DBR lasers.

REFERENCES

1. D. Z. Garbuzov, N. Y. Antonishkis, S. N. Zhigulin, *et al.*, Appl. Phys. Lett. **62**, 1062 (1993).

2. M. L. Boroditskiĭ, A. E. Dul'kin, I. V. Kochnev, *et al.*, Pis'ma Zh. Tekh. Fiz. **20** (6), 62 (1994) [Tech. Phys. Lett. **20**, 243 (1994)].

3. D. Z. Garbuzov, N. Y. Antonishkis, A. D. Bondarev, *et al.*, IEEE J. Quantum Electron. **27**, 1531 (1991).

4. D. Botez and L. J. Mawst, IEEE Circuits Devices Mag. **12**, 25 (1996).

5. D. A. Francis, C. J. Chang-Hasnain, and K. Eason, Appl. Phys. Lett. **68**, 1598 (1996).

6. J. N. Walpole, E. S. Kintzer, S. R. Chinn, *et al.*, Appl. Phys. Lett. **61**, 740 (1992).

7. G. S. Sokolovskii, E. U. Rafailov, D. J. L. Birkin, *et al.*, Opt. Quantum Electron. **31**, 215 (1999).

8. G. S. Sokolovskii, E. U. Rafailov, D. J. L. Birkin, and W. Sibbett, IEEE J. Quantum Electron. **36**, 1412 (2000).

9. D. A. Yanson, E. U. Rafailov, G. S. Sokolovskii, *et al.*, J. Appl. Phys. **95**, 1502 (2004).

10. Y. Boucher, A. G. Deryagin, V. I. Kuchinskii, *et al.*, Nanotechnology **14**, 615 (2003).

11. Y. Boucher, A. G. Deryagin, V. I. Kuchinskii, *et al.*, Semicond. Sci. Technol. **19**, 1010 (2004).

Translated by P. Pozdeev

Vapor Phase Deposition of Coatings onto Dust Particles in Combined Plasma

L. M. Vasilyak*, M. N. Vasil'ev, S. P. Vetchinin, D. N. Polyakov, and V. E. Fortov

Institute for High Energy Densities, Associated Institute for High Temperatures, Russian Academy of Sciences, Moscow, Russia
* e-mail: lab852@ihed.ras.ru
Received May 19, 2005

Abstract—Nickel coatings on polydisperse microparticles have been deposited from vapor phase in combined RF discharge–electron beam plasma. Features of the behavior of a dusty plasma cloud in the course of evaporation and deposition of coatings are considered. © *2005 Pleiades Publishing, Inc.*

The development of technology of active coatings on small particles, which can be used in nanotechnologies, hydrogen power engineering, and for obtaining disperse phases possessing unusual surface properties, is among currently important tasks. Such coatings can be deposited from a gas or vapor phase or by means of a directed flow of atoms and ions (e.g., in the course of RF magnetron sputtering [1]). The main problem encountered in implementing such methods consists in creating a controlled reaction volume for obtaining homogeneous coatings on the surface of microparticles and in providing the transfer of coated particles to a collector-container. Previously, we showed [2] that, by introducing an electron beam into dusty plasma, it is possible to combine the evaporation of a substance from electron-beam-heated target with the generation of combined RF discharge–electron beam (RFEB) plasma. This approach employs advantages of the electron-beam evaporation and the high activity of combined RFEB plasma. Unfortunately, the possibilities of obtaining a stable dusty plasma structure in the presence of a metal vapor and the temperature gradients (related to the heated target and the diffusive and radiative heat transfer to the dusty plasma) and in various regimes of evaporation have not been studied so far.

This Letter presents the results of investigations of the dynamics and homogeneity of a volume of the combined RFEB plasma containing polydisperse microparticles and nickel vapor in helium at pressures within 0.1–1 Torr. The microparticles represented hollow glass microspheres with diameters from 10 to 120 μm. We have studied the character of nickel deposition on microparticles and the possibility of controlling their flow. The experiments were performed in a large chamber ($35 \times 35 \times 80$ cm) of a laboratory plasmachemical reactor.

Figure 1 shows a schematic diagram of the experimental arrangement. RF discharge *1* was generated between a flat grid electrode *2* (diameter, 8 cm) and the reactor walls *3*. Microparticles were injected into the region above the flat grid electrode, where a dusty plasma structure *4* was formed. A monoenergetic electron beam *5* with an energy of 25 keV and a diameter of 1–2 mm was introduced into the reactor chamber via a two-step gasdynamic window and focused on the surface of nickel target *6*. Thus, the reactor provided activation of the surface of particles and their coating with nickel. After termination of the deposition process, the RF voltage was switched off and coated particles fell down through the grid into collector *7* situated under the electrode. The dusty plasma structure irradiated with a laser beam *9* was imaged using video cameras *8* through the side and top optical windows in the reactor chamber.

Before the onset of target evaporation, a stable dusty plasma structure with quite a high degree of ordering is formed over the RF electrode (Fig. 2a). Electron-beam-induced evaporation of the target gives rise to a temperature gradient caused by the diffusive and radiative heat transfer, which leads to violation of the homogeneity of the dusty plasma cloud (Fig. 2b) as a result of the ther-
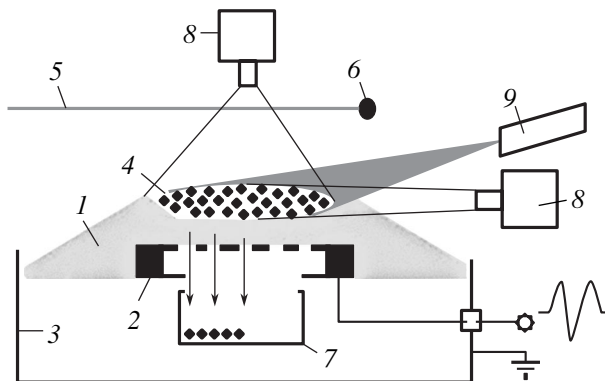

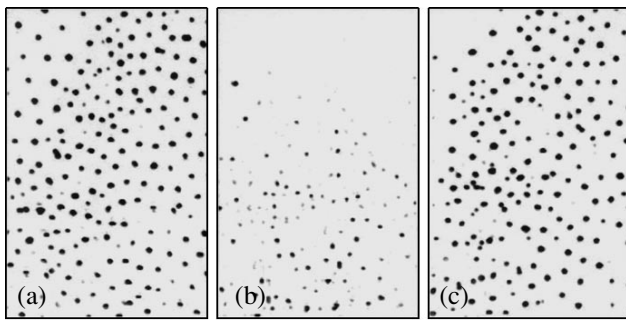**Fig. 1.** Schematic diagram of the experimental setup (see the text for explanations).

Fig. 2. Fragments of the images of the central part of a dusty plasma cloud (top view) (a) before switching on the electron beam, (b) during electron-beam-induced evaporation of the metal target, and (c) in the course of metal deposition onto microparticles.

mophoretic phenomena in the dusty plasma [3]. The cloud shifts away from the heated target, primarily because of the displacement of greater particles (Fig. 2b). When the target heating is switched off, the dusty plasma cloud returns to the initial position (Fig. 3c). The influence of a heated target on the cloud can be decreased by placing additional thermal screens and introducing auxiliary temperature fields in the region of the dusty plasma structure.

The process of activation and coating of the surface of microparticles takes place both during evaporation and after termination of the electron-beam heating of the target. The thickness of the nickel coating on microparticles depends on the time of their exposure in the reaction volume, the electron beam current, and the distance from the target to the dusty plasma structure. This conclusion is confirmed by a change in the optical density of coatings on a model flat glass surface. The task of obtaining homogeneous (over the particle surface) coatings with controlled thickness poses additional requirements on the temporal stability and spatial homogeneity of the reaction volume. The degree of inhomogeneity of the density of evaporated metal atoms in the reaction volume is determined by the asymmetric mutual arrangement of the evaporation and deposition zones, the temperature gradients in the reactor, and the edge effects. The influence of these inhomogeneities can be eliminated and the equal coating of particles can be ensured by providing multiply repeated chaotic stirring of particles over the entire reaction volume, or by their ordering in the horizontal plane with mixing of such layers in the vertical direction and rotation of the dusty plasma structure. It is also necessary to provide for the possibility of changing the grid mesh. In the standard commercial setups intended for the coating of flat substrates, homogeneous deposition is achieved by rotation of the substrates relative to the sources.

In our setup, rotation of the dusty plasma structure and variation of the distance between particles were provided by applying external magnetic fields of preset

configuration. The rate of rotation and the interparticle distance can be controlled by changing the magnetic induction [4]. The charged microparticles and plasma components were rotated in crossed electric and magnetic fields. For the radial magnetic field, the perpendicular field was the longitudinal electric field of the near-electrode layer of the RF discharge. For the longitudinal magnetic field, the perpendicular field can be provided by an ambipolar electric field. Note that the application of a magnetic field also increases the degree of surface activation [5] prior to metal deposition.

The structure of the cloud of microparticles can be stabilized and stirred by means of an appropriate modulation of the RF voltage and the electron beam current, or by selecting proper parameters in the case of their joint action, which was confirmed in experiment. The field-induced oscillations of particles may involve into stirring all layers in the dusty plasma structure. Pulse actions upon the dusty plasma structures can lead either to the chaotization and breakage or to the dynamical and spatial stabilization of such formations, since dusty particles in the plasma trap behave as oscillators. The breakage of the structure and loss of particles from the plasma trap can take place either at resonance frequencies and is determined by the intensity and duration of action both on the particles and their charge and on the plasma.

In order to provide for the collection of coated particles in a container, it is necessary to switch off the RF voltage, which implies termination of the discharge and does not allow the modification (coating) of particles to be carried out in a continuous regime. Moreover, since the container is situated in the zone of sedimentation, uncoated particles can also fall down and mix with the useful product. The removal of processed particles from the discharge zone and their collection can be provided using the phenomenon of electron beam action upon the dusty plasma structure [6]. According to this, an electron beam approaching such a cloud results in the attraction or repulsion of particles, depending on the beam current. Thus, by moving the beam in the horizontal plane, it is possible to shift the cloud toward the collector, which can be placed aside from the active reactor zone. The cloud can be driven using both attraction of the particles to the beam and their repulsion from it. Since the container is now situated in the region of a weak electric field, it is possible to collect coated particles without switching the RF discharge, by merely modulating the electron beam current and position. Simultaneously, a new portion of microparticles can be injected into the active zone, so that the process can be carried out in a quasi-continuous regime. Using thermophoresis induced by cooling of the container, it is possible to provide additional correction of the trajectories of collected particles and even to freeze them to the collector.

To summarize, the results of our experiments showed that it is possible to realize a stable dusty

plasma structure with a metal vapor, to obtain a homogeneous metal coating on microparticles, to drive the cloud of coated particles out of the discharge zone with the aid of an electron beam, and to collect the particles in a container.

REFERENCES

1. A. Ivanov, V. Mitin, A. Pal, *et al.*, in *Plasma Processes and Polymers: Proceedings of the 16th International Symposium on Plasma Chemistry, Taormina, 2003*, Ed. by R. d'Agostino, P. Favia, C. Oehr, and M. R. Wertheimer (Wiley, 2005).

2. L. M. Vasilyak, M. N. Vasil'ev, S. P. Vetchinin, *et al.*, Zh. Éksp. Teor. Fiz. **123**, 498 (2003) [JETP **96**, 440 (2003)].

3. L. M. Vasilyak, S. P. Vetchinin, D. N. Polyakov, *et al.*, Zh. Éksp. Teor. Fiz. **127**, 1166 (2005) [JETP **100**, 1029 (2005)].

4. L. M. Vasilyak, S. P. Vetchinin, and D. N. Polyakov, Tr. Inst. Teplofiz. Ékstrem. Sost. Ob"edin. Inst. Vysokikh Temp., No. 6, 291 (2004).

5. H. Okano, T. Ymazaki, and Y. Horiike, Solid State Technol. **25**, 166 (1982).

6. L. M. Vasilyak, M. N. Vasil'ev, S. P. Vetchinin, *et al.*, Izv. Ross. Akad. Nauk, Ser. Fiz. **67** (9), 20 (2003).

Translated by P. Pozdeev

High-Porosity Metal Structure Formation
under Stationary Nonequilibrium Condensation Conditions

V. I. Perekrestov

Sumy State University, Sumy, 40007 Ukraine
e-mail: kpe@sumdu.edu.ua
Received May 3, 2005

Abstract—A substantially new technological approach to the formation of high-porosity metal layers is proposed, which is based on the process of stationary nonequilibrium vapor condensation inside a hollow cathode. The conditions necessary for the manifestation of such a spatially distributed selective nucleation and growth of metal condensates are the realization of only monoatomic critical nuclei and the existence of a critical energy for the binding of adatoms to the growth surface (below this level, the probability of condensate formation is negligibly small). © *2005 Pleiades Publishing, Inc.*

High-porosity layers are promising materials for the creation of various nanostructures, sensor elements, ultrafine filters, catalysts, etc., which explains the increasing interest in the development of technologies for the formation of such layers. Previously, it was established [1, 2] that suppression of the process of coalescence in the diffusion field of adatoms in the course of vapor deposition under ultimately low supersaturation conditions makes possible the realization of a mechanism of spatially distributed nucleation and growth of condensates, which favors the formation of a high-porosity deposit. However, a significant disadvantage of this method is the low velocity of layer growth.

This study was aimed at determining the necessary conditions and developing the corresponding technical solutions for the formation of highly porous layers at a relatively high rate.

Experimental setup, results, and discussion. In the case of a vapor flowing under ultimately low supersaturation conditions, the condensation is possible only provided that the binding energies of adatoms on the growth surface are sufficiently high to decrease the critical nucleus size to a minimum [3]. For this reason, it would be expedient to describe the physics of nonequilibrium condensation in terms of the Walton–Rhodin atomistic model of small nuclei [3, 4]. Figure 1 shows a family of the qualitative dependences $\ln J = f(1/T_c)$ (where J is the nucleation rate and T_c is the temperature of the growth surface) constructed using this model. Each curve corresponds to a certain energy of binding of a condensed atom to the growth surface, and the break points indicate a transition from monoatomic critical nuclei (described by the upper part of the curve) to diatomic ones.

In order to reveal the conditions necessary for the formation of porous films, Fig. 1 shows some special binding energies including the maximum binding

energy (E_1) of adatoms on the defect-free substrate surface, the binding energies (E_2, E_4) of atoms adsorbed on the monoatomic steps of two different crystallographic planes; the binding energy (E_3) of adatoms bound to the substrate surface defects or subimplanted into this surface, and the binding energy (E_5) of an adatom occurring at the crystal intergrowth boundary. In the case under consideration, it is possible to assume that these characteristic energies obey the inequality $E_5 > E_4 > E_3 > E_2 > E_1$. The mutual arrangement of the curves in Fig. 1 corresponds to a situation when the crystal intergrowth boundaries in the condensate are already formed in large amounts. This family confirms the conclusion that purely monoatomic deposition (characteristic of nanotechnologies) at a relatively high condensa-
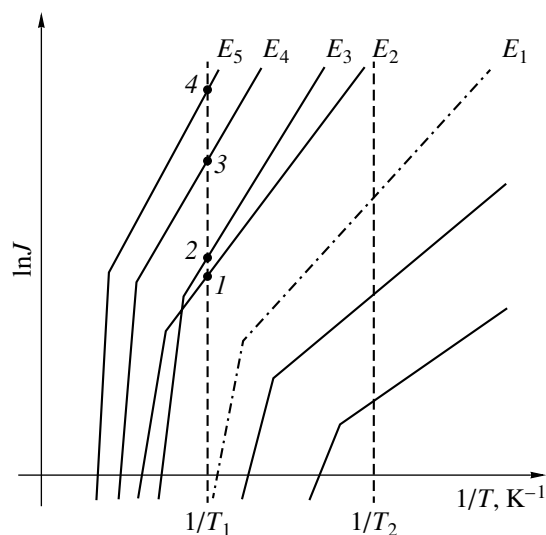

Fig. 1. Plots of the nucleation rate J versus growth surface temperature T_c in the $\ln J = f(1/T_c)$ coordinates.
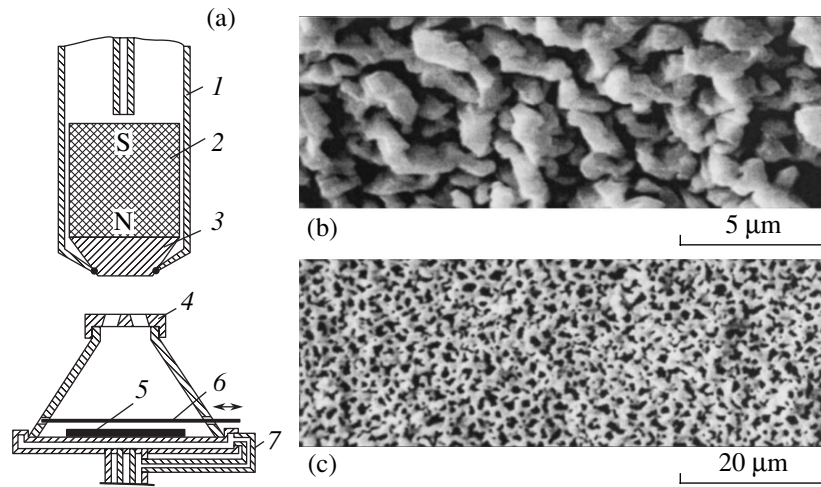
Fig. 2. (a) Schematic diagram of the ion sputter system: (*1*) water-cooled anode; (*2*) magnet; (*3*) magnetic guide; (*4*) sputtered part of cathode; (*5*) substrate; (*6*) shutter; (*7*) water-cooled cathode base. (b, c) Highly porous layers of copper obtained using discharge power P_u = 45 and 150 W, respectively.

tion temperature (~T_1) takes place for binding energies exceeding a certain critical value E_c. The rates J_i of monoatomic nucleation at the corresponding points of intersection obey the conditions $J_1 < J_2 < J_3 < J_4 < J_5$.

For a flow of particles acting on the growth surface, it is convenient to introduce an effective binding energy in any local region of this surface such that $E_e = E_a - (E_s + \Delta E)$, where E_s is the average energy transferred by the incident particles to adatoms and ΔE is the deviation from E_s. For otherwise equal technological parameters, this decrease in the adatom binding energy to E_e shifts all plots in Fig. 1 to lower temperatures. Therefore, by increasing the rate of condensate deposition (see the model of small nuclei [3, 4]), it is possible to return the system of curves in Fig. 1 to the initial position and to obtain high-porosity structures of the deposits.

Thus, the conditions necessary for the high-rate formation of porous structures are as follows:

(1) The process of layer formation on the macroscopic level has to be sufficiently stationary: any changes of technological parameters smear the dependences $\ln J = f(1/T_c)$ and violate selective deposition processes.

(2) In order to increase the anisotropy of crystal growth in various directions, the critical energy E_c must fall within the spectrum of binding energies of the atoms adsorbed on monoatomic steps of various crystallographic planes.

(3) The condensed atoms and other particles incident on the growth surface must possess a minimum spread of energies: otherwise, the effective binding energy will be smeared and, hence, the selective processes will be violated.

(4) In order to exclude the formation of columnar structures, the supply of vapor to various faces of the growing crystals must be sufficiently equiprobable and the electric field strength at the growth surface must be minimum.

Relatively high (up to several tens of microns per hour) rates of growth of the porous deposit were obtained with the aid of a substantially new ion sputter system, in which a stationary process was ensured by discharge stabilization due to the hollow cathode effect and the closed region of crossed electric and magnetic fields (Fig. 2a). The hollow cathode of the device is made entirely from the metal to be condensed and the material is sputtered predominantly from the region at the input hole of the cathode. Subsequently, the sputtered atoms are ionized by an intense electron beam emitted from the hollow cathode, and the ions are accelerated in the electric field and drawn into the cathode. As a result, high-density plasma is formed inside the cathode with a narrow input hole. The plasma contains ions of the condensed metal and the working gas (argon) purified using a special method [5]. A nonequilibrium character of the condensation process is provided by the characteristic action of plasma upon the growth surface [6]. The temperature of deposition was determined using a method described previously [7]. Ion bombardment of the growth surface leads to repeated evaporation and sputtering of the condensed atoms, which are again subjected to ionization and deposition. This cyclic mechanism of mass transfer involving each atom is reproduced until the binding energy would exceed the critical level E_c.

Evidently, on the passage to substances possessing higher equilibrium vapor pressures and ion sputtering yields and/or lower sputtering threshold energies E_r and melting temperatures T_p, the nonequilibrium character of condensation is enhanced. Susceptibility of an element to the spatially distributed selective nucleation

Correlation coefficients α, growth surface temperatures T_c, and optimum discharge powers P_u for the formation of high-porosity metal structures

Metal	Ta	Ni	Al	Cu
α (eV^{-1} K^{-1})	0.13	1.5	3.34	4.6
T_c (°C)	1150–1200	700–800	300–400	120–300
P_u (W)	900	750	350	45–150

and condensation is characterized by the correlation coefficient $\alpha = 10^8 K_i / T_r E_r T_p$, where T_r is the temperature at which the saturated vapor pressure for a given substance amounts to 1.3 Pa and K_i is the sputtering yield for 200-eV Ar$^+$ ions. The spectrum of metals for this investigation (see table) was selected so as to provide for a rather broad interval of α values.

Generalization of the obtained experimental results leads to the following conclusions:

(i) The structural selectivity, which is manifested by the formation of layers with a three-dimensional labyrinth structure, increases with decreasing electric field strength at the growth surface, with increasing efficiency of the volume diffusion field at the growth surface, and with growing T_c, which can be provided by using the optimum discharge power (P_u) in agreement with the correlation coefficient α (see table).

(ii) By enhancing the repeated sputtering of deposited material at the expense of increased discharge power, it is possible to obtain involved structures with connecting elements in the form of nanowires (Figs. 2b and 2c).

REFERENCES

1. V. I. Perekrestov, S. N. Kravchenko, and A. V. Pavlov, Fiz. Met. Metalloved. **88** (5), 72 (1999).
2. V. I. Perekrestov, A. V. Koropov, and S. N. Kravchenko, Fiz. Tverd. Tela (St. Petersburg) **44**, 1131 (2002) [Phys. Solid State **44**, 1181 (2002)].
3. T. Rhodin and D Walton, in *Single Crystal Films* (Mir, Moscow, 1966), pp. 44–57 [in Russian]
4. D. Walton, T. Rhodin, and R. Rollings, J. Chem. Phys. **38**, 2698 (1963).
5. V. I. Perekrestov and S. N. Kravchenko, Prib. Tekh. Éksp., No. 3, 123 (2002).
6. B. I. Moskalev, *Hollow-Cathode Discharge* (Énergiya, Moscow, 1969) [in Russian].
7. V. I. Perekrestov and Yu. A. Kosminskaya, Pis'ma Zh. Éksp. Teor. Fiz. **78**, 258 (2003) [JETP Lett. **78**, 223 (2003)].

Translated by P. Pozdeev

Collisionality in an Ensemble of Identical Charged Particles in a Closed Magnetic Trap

V. A. Gordienko and A. E. Dubinov

Sarov State Physicotechnical Institute, Sarov, Russia
Received April 22, 2005

Abstract—A strict proof of the theorem of infinite collisionality in an ensemble of identical charged particles in a closed magnetic trap is presented. © *2005 Pleiades Publishing, Inc.*

The problem concerning the number of collisions in a finite ensemble of the ideal gas particles on an infinite line, infinite plane, or infinite space was formulated by Ya.G. Sinai several decades ago. It can be shown that this problem reduces to the billiard-table problem with a single particle in a phase space of large dimension and complex geometry, and the total number of collisions is finite. An introduction to the methods of solving such problems is presented and the state of the art in this field is considered in [1–3]. Solution of these problems is important for the analysis of ergodic properties of the ideal gas in statistical mechanics.

It is intuitively clear that the number of particle collisions in the system under consideration is finite, since the particles gradually, one after another, go to infinity and lose the ability to participate in collisions. However, if there are reasons or mechanisms preventing the loss of particles or returning them back to the interaction region, the question concerning collisionality in the system may have a different answer. For example, bounded regions or magnetic fields offer such factors for charged particles.

This Letter is devoted to one of the possible examples—a finite ensemble of charged particles in a closed magnetic trap—and gives a strict proof of the theorem of the infinite collisionality in this system.

The trap Ξ (Fig. 1) comprises an infinite band with the width L bounded by the walls elastically reflecting incident particles, to which a homogeneous stationary magnetic field B is applied. First, let us briefly recall how a single charged particle will behave in such a trap. The particle will move along a trajectory representing a cylindrical helix with constant pitch. The cylinder radius R_c and the period T_c of particle rotation around the cylinder axis are given by the formulas

$$R_c = \frac{m v^{\perp}}{qB}; \quad T_c = \frac{2\pi m}{qB}. \tag{1}$$

Note that the period T_c is independent of the transverse velocity $v^{\perp}$; therefore, particles with identical ratios of charge q to mass m exhibit synchronous rotation (cyclotron resonance). On reaching the wall, the particle is elastically reflected, whereby its transverse velocity component $v^{\perp}$ is retained and the longitudinal velocity $v^{\parallel}$ is changed to opposite. As a result, the particle will perform periodic helical flights between the walls with a period of $T_b = 2L/v^{\parallel}$ (bounce oscillations).

Now let us proceed to the question concerning the number of collisions in an ensemble of identical particles in a closed magnetic trap Ξ. We will assume that the number of particles is not very large (so that the space charge field can be ignored) or that their charge is compensated by a neutralizing inertialess background of oppositely charged particles. Under such conditions, the following theorem is valid:

Theorem. If an ensemble consisting of not less than two identical charged particles of nonzero diameter occurring in a closed magnetic trap Ξ features at least
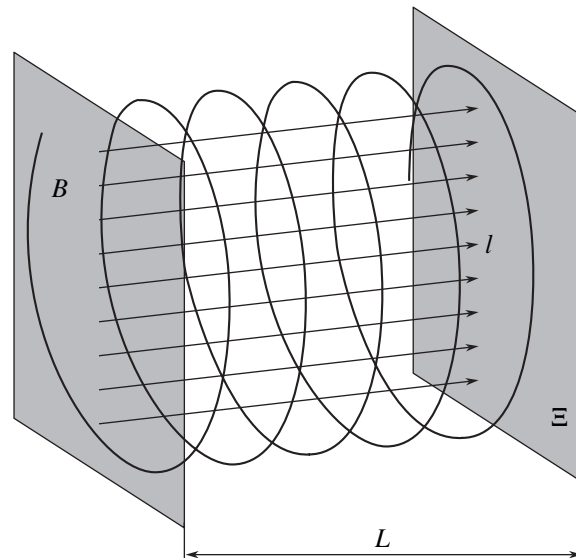

Fig. 1. Schematic diagram showing the closed magnetic trap and the trajectory of a particle in this trap.
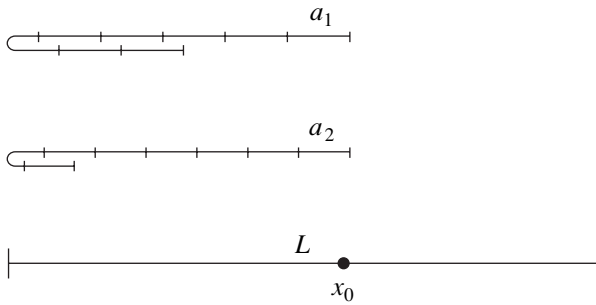
Fig. 2. Stacking segments of lengths a_1 and a_2 over the main segment of length L with reflections from its ends.
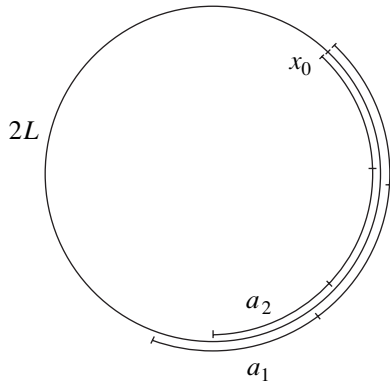

Fig. 3. Stacking arcs of lengths a_1 and a_2 over the circle of perimeter $2L$.

one collision between particles, then the number of such collisions will be infinitely large.

Remark 1. According to the principle of mathematical induction, it will be sufficient to show that, if one collision takes place, this will be unavoidably followed by one more collision.

Proof of the theorem. Let us assume that a collision between a pair of identical particles (for certainty, 1st and 2nd) took place in the trap Ξ at a point with the longitudinal coordinate x_0. Let this collision occur on a magnetic field line l passing through the point x_0. Upon collision, the particles will travel along their trajectories and, in the absence of other collisions, they will return to the field line l at the same moment of time. However, their positions on line l will be displaced relative to point x_0 because of the arbitrary values of the longitudinal velocities $v_1^{\parallel}$ and $v_2^{\parallel}$. Since the transverse velocities of particles, $v_1^{\perp}$ and $v_2^{\perp}$, are also arbitrary, they may collide again only on the field line l (collisions between the same particles out of line l and the collisions of any of them with 3rd particle are possible only under certain specially selected conditions, which only strengthen the proof).

In order to check for the next collision in the pair under consideration, we have to consider the distance between these particles at the moment they simultaneously cross line l. It will be sufficient to show that, for any preset value of δl, there exists a number N of their simultaneous passages through line l, such that the distance between particles is shorter than δl.

Geometrically, the problem is formulated as follows. Consider a point x_0 on a segment of length L and let this segment be butt-covered, beginning with point x_0, by stacked segments of the first kind with the length $a_1 = v_1^{\parallel} T_c$ and by segments of the second kind with the length $a_2 = v_2^{\parallel} T_c$ (Fig. 2). On attaining the end of segment L, the imposed segment is bent backward and the coverage is continued. We have to prove that there exists a number N such that the distance between ends of the segments a_1 and a_2 covering segment L on the Nth step will be shorter than any arbitrarily set dl value.

Remark 2. There are no limitations on the a_1 and a_2 values (in particular, they can be either greater or smaller than L).

Remark 3. Segments a_1 and a_2 can be stacked either in the same or in the opposite directions from point x_0.

Note that the process of stacking segments of lengths a_1 and a_2 over the main segment of length L with reflections from its ends is equivalent to stacking arcs of lengths a_1 and a_2 over the circle with a perimeter of $2L$ (Fig. 3).

In order to solve the problem, we will employ a modified method used to prove the Jacoby theorem [2, p. 32]. Let us assume, for certainty, that $a_1 > a_2$ and the arcs are stacked in the same direction—for example, clockwise—from point x_0. At a certain step of stacking, the first particle will overtake the second particle by making a greater number of complete turns over the $2L$ circle. Let the number of arc steps made by this moment be n and let the distance between particles immediately upon overtake be $b < a_1/2$ (the case of the opposite inequality is treated similarly, by considering the distance immediately before the overtake). Then, after the next n steps, the overtake will reach $2b$, after another n steps it will reach $3b$, and so on. Thus, the distance between particles after every n steps changes at an arc increment of b and, hence, the arc increment has in fact decreased from a_1 to $b < a_1/2$.

This procedure is continued until a moment when, at a certain step of motion with an arc step b, we will cover the distance $2L$. For certainty, let the total number of steps by this moment be $m = kn$, and let the distance between particles immediately upon this overtake be $c < b/2$ (the case of the opposite inequality is treated similarly). Thus, the arc increment has again decreased to become $c < b/2 < a_1/4$.

Continuing this consideration, we will again cover the distance $2L$ by still shorter arc steps and once again decrease the arc distance between particles at the moment of overtake. Therefore, by repeating this process, we can decrease the arc distance between the two particles below any preset value. For a finite radius of particles, this implies unavoidable collision between them. Thus, the theorem is proved.

The case of stacking segments in the opposite directions from point x_0 is treated similarly, by considering the points of meeting instead of the points of overtake.

Thus, we have demonstrated that a homogeneous magnetic field of even very small magnitude can substantially change the answer to the question concerning the collisionality in an ensemble of identical particles.

REFERENCES

1. G. A. Gal'perin, Tr. Mosk. Mat. Obshch. **43**, 142 (1981).

2. G. A. Gal'perin and A. N. Zemlyakov, *Mathematical Billiards* (Nauka, Moscow, 1990) [in Russian].

3. G. A. Gal'perin, Mat. Prosveshchenie, Ser. 3, No. 5, 65 (2001).

Translated by P. Pozdeev

Effects of Intense Plastic Straining on the Structure of Barium, Lead, and Cadmium Titanates

N. V. Prutsakova, Yu. V. Kabirov, E. V. Chebanova,
Yu. A. Kuprina, and M. F. Kupriyanov

Rostov State University, Rostov-on-Don, Russia
e-mail: shpilevay@mail.ru

Received April 7, 2005

Abstract—Under the action of intense plastic straining (IPS), barium titanate ($BaTiO_3$) exhibits a phase transition from the tetragonal to cubic structure, while lead titanate ($PbTiO_3$) shows a tendency to such a transformation. In cadmium titanate ($CdTiO_3$), the IPS induces a transition from the perovskite to ilmenite phase. © 2005 Pleiades Publishing, Inc.

The results of extensive investigations of the ferroelectric oxides with perovskite structures show that the formation and stabilization of the structure and properties of these materials are strongly dependent on numerous internal and external factors. In recent years, much attention has been devoted to nanodimensional effects in the classical ferroelectrics $BaTiO_3$ and $PbTiO_3$ [1–5]. It is commonly accepted that the transition to a nanodimensional state in these perovskites leads to suppression of their ferroelectric properties, which is analogous to the loss of such properties in the crystals with various defects [6–8].

As is known, early crystallization stages in barium titanate ($BaTiO_3$) featuring the passage from nanocrystalline (1–20 nm) to macrocrystalline (20–100 nm and above) states involve a phase transition from the cubic (nanodimensional) to tetragonal structure [9]. During the crystallization from an amorphous state at low annealing temperatures, $BaTiO_3$ forms a pyrochlore phase [10], which converts into a perovskite phase at higher temperatures. Cadmium titanate ($CdTiO_3$) synthesized at low temperatures forms an ilmenite phase [11, 12], which converts into a perovskite phase only at temperatures above 850°C.

At present, various methods are used for obtaining nanostructures [13]. In particular, a method based on the effect of intense plastic straining (IPS) and the results of using this method were described in much detail in [14].

This paper presents the results of X-ray diffraction study of the IPS-induced changes in the structural states of polycrystalline $BaTiO_3$, $PbTiO_3$, and $CdTiO_3$. The initial polycrystalline samples had stabilized perovskite structures corresponding to the macrocrystalline state.

The IPS conditions were realized using an IPD-70M setup described elsewhere [14]. An external pressure of 0.5 GPa was applied to a sample and a shear strain was created by two or four turns of the anvils. The samples in the initial state and upon IPS in different regimes were studied by X-ray diffraction. The measurements were performed n a DRON-3M diffractometer using CuK_α radiation, with computer-aided registration of the diffraction patterns.

The main experimental results are summarized in the table. Figure 1 shows the typical diffractograms, which indicate that $BaTiO_3$ under IPS conditions is subject to a phase transition from the initial tetragonal to cubic structure. Upon the transition, the unit cell volume exhibits an insignificant increase, which was previously observed in the samples upon grain refinement [9].

Thus, the IPS action is sufficient to convert $BaTiO_3$ into a nanocrystalline state. This is indirectly confirmed by a sharp growth in the halfwidth (full width at half
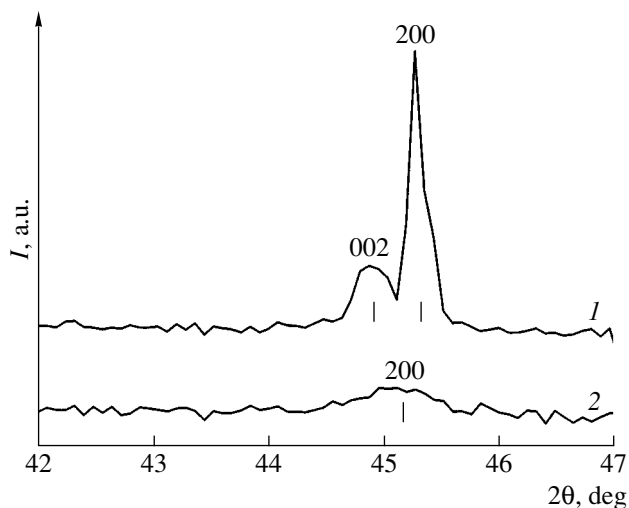

Fig. 1. X-ray diffractograms of $BaTiO_3$ (*1*) before and (*2*) after IPS (at four turns of the anvils).

Fig. 2. X-ray diffractograms of PbTiO$_3$ (*1*) before and (*2*) after IPS (at four turns of the anvils).
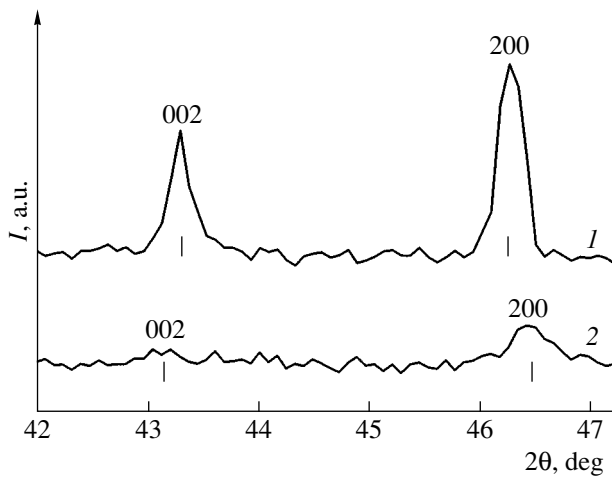

Fig. 3. X-ray diffractograms of CdTiO$_3$ (*1*) before and (*2*) after IPS (at four turns of the anvils).

maximum, FWHM) of diffraction reflections. Unfortunately, the low quality of the diffraction profiles obtained in experiments did not allow us to clearly separate the effect of a decrease in the size of coherent scattering domains from the effect of inhomogeneous microdeformations (which can also be significant under IPS conditions).

The action of IPS on PbTiO$_3$ (Fig. 2) was low effective. The crystal lattice parameters of the sample were changed rather insignificantly, although the observed trends showed a tendency of transition to a nanocrystalline state: the unit cell volume somewhat increased and the degree of tetragonal distortion (c/a) – 1 decreased upon IPS.
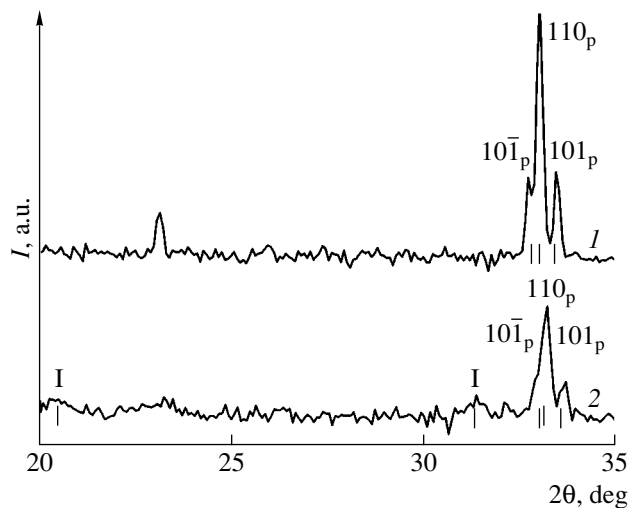
A comparison of the IPS effects on lead and barium titanates shows that PbTiO$_3$ is a more stable ferroelectric crystal than BaTiO$_3$. This is probably related to the higher spontaneous polarization in PbTiO$_3$.

A distinctive feature of the IPS action on CdTiO$_3$ is a decrease in the volume of the monoclinic perovskite cell. The X-ray diffractogram of CdTiO$_3$ upon IPS (Fig. 3) exhibits reflections of an ilmenite phase ($2\theta = 20.30°$ and $31.36°$) in addition to reflections of the perovskite phase. Previously, investigations of the effect of irradiation at a dose of 10^7 R on the state of single crystal and polycrystalline CdTi$_3$ samples with perovskite structures [15, 16] showed that the appearance of radi-

Structural parameters of BaTiO$_3$, PbTiO$_3$, and CdTiO$_3$ before and after IPS

Sample	IPS degree (number of turns)	Unit cell parameters		Unit cell volume, Å^3	FWHM of diffraction reflections	
		a, Å	c, Å		B_{002}, deg	B_{200}, deg
BaTiO$_3$	0	4.000(1)	4.034	64.54	0.37(5)	0.29
	2	4.006	4.020	64.50	$\Sigma = 0.86$*	
	4	4.016	4.016	64.77	0.69	
PbTiO$_3$	0	3.896	4.146	62.93	0.24	0.23
	2	3.897	4.147	62.98	0.79	0.55
	4	3.903	4.143	63.11	1.00	0.45

Sample	IPS degree (number of turns)	Unit cell parameters			Unit cell volume, Å^3	FWHM of diffraction reflections	
		a, Å	b, Å	β, deg		B_{200}, deg	B_{020}, deg
CdTiO$_3$	0	3.815	3.828	91.3	55.69	0.29	0.22
	2	3.805	3.818	91.2	55.26	0.30	0.34
	4	3.804	3.816	91.3	55.23	0.30	0.30

* Total halfwidth of unresolved 002 and 200 reflections.

ation-induced structural defects led only to an increase in the perovskite lattice parameters.

Thus, we have observed for the first time a reversible ilmenite–perovskite reconstructive phase transition in $CdTiO_3$, whereby the IPS action led to a partial conversion of the initial perovskite structure into a relatively loose structure of the ilmenite type.

The decrease in the perovskite cell volume in $CdTiO_3$, in contrast to the increase in the unit cell volumes of $BaTiO_3$ and $PbTiO_3$, is probably related to some special features of the corresponding crystalline states. On the one hand, the IPS action on $BaTiO_3$ and $PbTiO_3$ takes place in the ferroelectric state, whereas $CdTiO_3$ initially occurs in the paraelectric state. On the other hand, a decrease in the perovskite cell volume in $CdTiO_3$ upon IPS can be explained by the fact that the final ilmenite structure (which is more loose than the perovskite one) compensates for the possible loosening of the perovskite structure observed in $BaTiO_3$ and $PbTiO_3$.

REFERENCES

1. S. O'Brien, L. Brus, and B. Murray, J. Am. Chem. Soc. **123**, 12085 (2001).

2. S. Chattopadhyay, P. Ayyub, V. Palkar, *et al.*, Phys. Rev. B **52**, 13177 (1995).

3. P. Ayyub, V. Palkar, S. Chattopadhyay, *et al.*, Phys. Rev. B **51**, 6135 (1995).

4. B. Jiang and L. Bursill, Phys. Rev. B **60**, 9978 (1999).

5. R. Böttcher, C. Klimm, D. Michel, *et al.*, Phys. Rev. B **62**, 2085 (2000).

6. B. Hilczer, Mater. Sci. **1**–**2** (Part 2), 3 (1976).

7. V. Z. Borodin, S. G. Gakh, and V. A. Babanskikh, Izv. Akad. Nauk SSSR, Ser. Fiz. **47**, 762 (1983).

8. O. Hauser and M. Shank, Phys. Status Solidi **18**, 547 (1966).

9. N. B. Kofanova, Yu. A. Kuprina, and M. F. Kupriyanov, Izv. Ross. Akad. Nauk, Ser. Fiz. **66**, 839 (2002).

10. F. W. Martin, Phys. Chem. Glasses **6**, 143 (1965).

11. H. D. Megav, Proc. Phys. Soc. **52** (326), 133 (1946).

12. Yu. V. Kabirov, B. S. Kul'buzhev, and M. F. Kupriyanov, Zh. Strukt. Khim. **42**, 972 (2001).

13. A. I. Gusev and A. A. Rempel', *Nanocrystalline Materials* (Fizmatlit, Moscow, 2001; Cambridge Int. Sci., Cambridge, 2004).

14. R. Z. Valiev and I. V. Aleksandrov, *Nanocrystalline Materials Produced by Intense Plastic Straining* (Logos, Moscow, 2000) [in Russian].

15. Yu. V. Kabirov, M. F. Kupriyanov, Ya. Dets, and P. Vavzhala, Fiz. Tverd. Tela (St. Petersburg) **42**, 1291 (2000) [Phys. Solid State **42**, 1329 (2000)].

16. N. V. Shpilevaya, Yu. V. Kabirov, and M. F. Kupriyanov, Fiz. Tverd. Tela (St. Petersburg) **46**, 1682 (2004) [Phys. Solid State **46**, 1737 (2004)].

Translated by P. Pozdeev

Imaging Inhomogeneous Objects with Free Boundaries by Laser Photoacoustic Method

K. L. Muratikov

Ioffe Physicotechnical Institute, Russian Academy of Sciences, St. Petersburg, 194021 Russia
e-mail: klm@holo.ioffe.ru
Received February 9, 2005; in final form, May 17, 2005

Abstract—The formation of a photoacoustic response from an inhomogeneous object with a free boundary is analyzed. Analytical expressions describing thermoelastic strains in an inhomogeneous object bounded by a plane are obtained within the framework of the perturbation theory. In a quasi-static case, the photoacoustic image is formed due to inhomogeneities in the thermoelastic coupling coefficient. Formulas for the photoacoustic response of a piezoelectric sensor operating in various regimes are obtained. © 2005 Pleiades Publishing, Inc.

In recent years, processes related to the generation, propagation, and detection of thermal and acoustic waves excited by laser radiation in inhomogeneous solids have received much attention [1, 2]. The interest in studying these phenomena is related to the wide possibilities of using photoacoustic and photothermal microscopy for diagnostics of the state of near-surface layers of various materials and structures on a microscopic level [3]. Correct interpretation of the data of photoacoustic and photothermal microscopy is based on a detailed description of the interactions of thermal and acoustic waves with inhomogeneities present in the objects studied. Such interactions have been studied in sufficient detail from the standpoint of photothermal microscopy [4–6], while the situation in photoacoustic microscopy with piezoelectric signal detection is much less satisfactory. An important distinctive feature of the photoacoustic microscopy with piezoelectric signal detection, in comparison to the photothermal microscopy, is the need to take into account nonstationary thermoelastic strains arising in the probed object as a result of absorption of modulated laser radiation.

Previously, the process of laser-radiation-induced nonstationary thermoelastic straining was studied for inhomogeneous objects with fixed boundaries [7]. This Letter presents the results of analysis of the formation of a photoacoustic piezoelectric response from an inhomogeneous object under the conditions where its surface remains free. Similar to the previous analysis [7], we will consider a three-dimensional model within the framework of perturbation theory. In solving this task, we can use the classical theory developed for elastic straining of a medium bounded by a plane; an approach to solving such problems is outlined in [8]. However, the analysis of the photoacoustic effect requires additional determination of thermoelastic deformations. In

this study, the main attention is devoted to the analysis of features related the thermoelastic effect.

Nonstationary thermoelastic strains arising in a solid in the course of absorption of modulated laser radiation can be described using the equations of motion [8] with the stress tensor σ including the thermoelastic effect:

$$\sigma_{ij} = 2\mu(\mathbf{r})u_{ij} + [\lambda(\mathbf{r})u_{kk} - \gamma(\mathbf{r})(T - T_0)]\delta_{ik}.$$

Here, λ and μ are the Lamé elastic constants, γ is the thermoelastic coupling coefficient, u_{ij} are the components of the strain tensor, T is the temperature of the laser-heated object, and T_0 is the temperature of the ambient medium.

An important feature of the above expression, distinguishing it from the commonly accepted representations of the stress tensor is that the Lamé constants and the thermoelastic coupling coefficient are coordinate-dependent. Previously, it was pointed out [7] that the lengths of acoustic waves in solids are much greater than the lengths of thermal waves in a broad range of frequencies up to about 1 GHz. Therefore, within the framework of the so-called quasi-static approximation, the photoacoustic imaging due to inhomogeneities in the elastic properties of objects is impossible because of poor resolution. Then, the observed photoacoustic images are determined predominantly by inhomogeneities in the thermoelastic coupling coefficient, since this response is related to much shorter lengths of the thermal waves.

Taking into account the above remark, let as assume that all inhomogeneities in the object under consideration are related only to the coefficient of thermoelastic coupling. Accordingly, this coefficient can be written as $\gamma = \gamma_0 + \gamma_1(\mathbf{r})$, where γ_0 is the value characterizing the corresponding homogeneous object and γ_1 is the contri-

bution due to inhomogeneities inside the object. Similarly to [7], we will also assume the inhomogeneity of the object to be weak, so that $\gamma_0 \gg \gamma_1$. Then, within the framework of perturbation theory, the temperature variations ΔT in the object excited by nonstationary laser radiation and the thermoelastic strain vector components Δu_i and can also be represented as $\Delta u_i = \Delta u_i^{(0)} + \Delta u_i^{(1)}$ and $\Delta T = \Delta T^{(0)} + \Delta T^{(1)}$, where $\Delta u_i^{(0)} \gg \Delta u_i^{(1)}$ and $\Delta T^{(0)} \gg \Delta T^{(1)}$. Here, $\Delta u_i^{(0)}$ and $\Delta T^{(0)}$ describe the strain and temperature distributions generated by laser radiation in the homogeneous object, $\Delta u_i^{(1)}$ and $\Delta T^{(1)}$ correspond to the perturbations caused by inhomogeneities present in the object.

The equation of motion was presented (with allowance for the above assumptions) in [7]. This equation has to be solved for an object with a free surface, which corresponds to the condition $\sigma_{iz} n_z|_{z=0} = 0$ at $z = 0$, where n_i are the components of a unit vector perpendicular to the sample surface. In the explicit form, this boundary condition for the strain tensor components in the first order of perturbation theory can be written as

$$\Delta u_{xz}^{(1)}\big|_{z=0} = \Delta u_{yz}^{(1)}\big|_{z=0} = 0, \tag{1a}$$

$$(\lambda_0 \Delta u_{ll}^{(1)} + 2\mu_0 \Delta u_{zz}^{(1)})\big|_{z=0} = \gamma_0 \Delta T^{(1)} + \gamma_1 \Delta T^{(0)}. \tag{1b}$$

Within the framework of the proposed model, the consideration will be restricted to an object which is homogeneous with respect to its thermal properties. Then, we may assume that, in Eqs. (1), $\Delta T^{(1)} = 0$ and $\Delta T^{(0)}$ can be determined from the equation of heat conduction in the homogeneous object.

In order to solve the problem formulated above, we can use an approach developed in the theory of elasticity for a solid bounded by a plane [8]. However, we must take into account that the equation of motion in the problem considered in the theory of elasticity is homogeneous, whereas our equation of motion is homogeneous since its right-hand part contains a term of the type $\dfrac{\partial}{\partial x_i}(\gamma_1 \Delta T^{(0)})$. Taking this into account, let us represent the strain vector by analogy with that in [8] as

$$\Delta \mathbf{u}^{(1)} = \mathbf{f}^{(0)} + \Delta \mathbf{U}^{(1)}, \tag{2}$$

where $\mathbf{f}^{(0)}$ is a partial solution of the equation of motion. This partial solution can be found using a method described in [9]. Not dwelling here on the details of these calculations, we will use the final result for the $\mathbf{f}^{(0)}$ vector components:

$$f_i^{(0)} = \frac{1}{4\pi(\lambda_0 + 2\mu_0)}\int d^3 r' \frac{\gamma_1(\mathbf{r}')\Delta T^{(0)}(\mathbf{r}')}{|\mathbf{r} - \mathbf{r}'|^3}(x_i - x_i'). \tag{3}$$

Using representation (2) of the strain tensor components $\Delta u_i^{(1)}$, we can rewrite the boundary conditions (1) for the components of $\Delta U_{ik}^{(1)}$ tensor as

$$\Delta U_{xz}^{(1)}\big|_{z=0} = -\left(\frac{\partial f_x^{(0)}}{\partial z} + \frac{\partial f_z^{(0)}}{\partial x}\right),$$

$$\Delta U_{yz}^{(1)}\big|_{z=0} = -\left(\frac{\partial f_y^{(0)}}{\partial z} + \frac{\partial f_z^{(0)}}{\partial y}\right), \tag{4a}$$

$$(\lambda_0 U_{ll}^{(1)} + 2\mu_0 U_{zz}^{(1)})\big|_{z=0}$$
$$= \gamma_1 \Delta T^{(0)} - \lambda_0 f_{ll}^{(0)} + 2\mu_0 f_{zz}^{(0)}. \tag{4b}$$

Note that the equation of motion for vector $\Delta \mathbf{U}^{(1)}$ is homogeneous.

It should be noted that, considering the problem of the usual theory of elasticity with a certain distribution of the force $\mathbf{P}(x, y)$ on the sample surface, the boundary condition corresponding to the free surface can be written as

$$\sigma_{iz}^{(0)}\big|_{z=0} = -P_i, \tag{5}$$

where $\sigma_{ij}^{(0)} = \lambda u_{ll}\delta_{ik} + 2\mu u_{ij}$ is the stress tensor of the theory of elasticity without allowance for the thermoelastic effect.

A problem of this kind is analyzed in [8]. A comparison of the boundary conditions (4) and (5) shows that they coincide in form for

$$P_x = \mu_0\left(\frac{\partial f_x^{(0)}}{\partial z} + \frac{\partial f_x^{(0)}}{\partial x}\right), \quad P_y = \mu_0\left(\frac{\partial f_y^{(0)}}{\partial z} + \frac{\partial f_z^{(0)}}{\partial y}\right), \tag{6a}$$

$$P_z = \lambda_0 \mathrm{div}\mathbf{f}^{(0)} + 2\mu_0\frac{\partial f_z^{(0)}}{\partial z} - \gamma_1 \Delta T^{(0)}. \tag{6b}$$

Thus, by introducing a force distribution on the sample surface using expressions (6), we can take into account the thermoelastic effect within the framework of the problem considered in the usual theory of elasticity. A solution of this problem with the boundary condition (5) for the strain vector components is presented in [8]. Using this result, the components of vector $\Delta u_i^{(1)}$ in the problem of thermoelasticity under consideration can be written as follows:

$$\Delta u_i^{(1)}(\mathbf{r})$$
$$= f_i^{(0)} + \int dx'\int dy' G_{ik}(x - x', y - y', z)P_k(x', y'), \tag{7}$$

where G_{ik} are the components of the tensor Green's function for the equations of motion in the quasi-static

approximation for a semiinfinite medium occurring under the action of only the surface force with the components P_i given by expressions (6).

The components of the tensor Green's function are presented in [8]. For determining vector $\Delta u^{(1)}$ it is necessary to substitute the components of $\mathbf{P}(x, y)$ from Eqs. (6) into Eq. (7). In the general case, the resulting expressions are rather lengthy and are not reproduced here. Expressions for $\Delta u_i^{(1)}$ can be written in a simpler form in the case of $z \gg |x - x_0|$, $z \ll |y - y_0|$ (see figure). Using Eqs. (7), it is possible to show, for example, that the deformations $\Delta u_x^{(1)}$ and $\Delta u_z^{(1)}$ in this case are described by the formulas

$$\Delta u_x^{(1)} = -\frac{(1 - 4\sigma^2)(1 + \sigma)}{2\pi E(1 - \sigma)}$$
$$\times \frac{1}{z^2} \int dx' \int dy' (x - x') \gamma_1(x', y', 0) \Delta T^{(0)}(x', y', 0), \tag{8a}$$

$$\Delta u_z^{(1)} = -\frac{(3 - 2\sigma)(1 - 2\sigma)(1 + \sigma)}{2\pi E(1 - \sigma)}$$
$$\times \frac{1}{z} \int dx' \int dy' \gamma_1(x', y', 0) \Delta T^{(0)}(x', y', 0). \tag{8b}$$

Using these formulas, it is possible to determine the response signal detected by a piezoelectric sensor at a distance z from the upper surface of the sample. Depending on the oscillation mode excited in the piezo-element, the response signal ΔV can be proportional to $\dfrac{\partial \Delta u_z^{(1)}}{\partial z}$ or $\left(\dfrac{\partial \Delta u_x^{(1)}}{\partial x} + \dfrac{\partial \Delta u_y^{(1)}}{\partial y}\right)$ [10, 11]. The latter expression refers to thin piezoelectric sensors exhibiting bending oscillations in course of signal detection.

It is possible to show that, in accordance with formulas (8), the piezoelectric signals in the two cases are given by the formulas

$$\Delta V_1 = -C_1 \frac{(1 - 4\sigma^2)(1 + \sigma)}{\pi E(1 - \sigma)}$$
$$\times \frac{1}{z^2} \int dx' \int dy' \gamma_1(x', y', 0) \Delta T^{(0)}(x', y', 0), \tag{9a}$$

$$\Delta V_2 = C_2 \frac{(3 - 2\sigma)(1 - 2\sigma)(1 + \sigma)}{2\pi E(1 - \sigma)}$$
$$\times \frac{1}{z^2} \int dx' \int dy' \gamma_1(x', y', 0) \Delta T^{(0)}(x', y', 0), \tag{9b}$$

respectively, where C_1 and C_2 is a coefficient dependent on the piezoelectric sensor characteristics.

Formulas (9) present a three-dimensional generalization of the results obtained previously within the
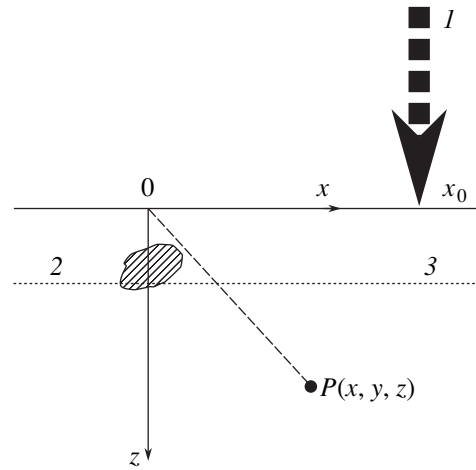
Geometry of photoacoustic imaging: (*1*) exciting laser radiation; (*2*) inhomogeneity in the probed object; (*3*) boundary of the zone of the photoacoustic response signal formation; $P(x, y, z)$ is the point of strain registration.

framework of a one-dimensional model [12–18] and supplement the results obtained in the analysis of the formation of a photoacoustic signal from inhomogeneous objects with a fixed boundary [7]. Expressions (9) were obtained without any special assumptions concerning the properties of materials. Therefore, these formulas are universal and can be used in the interpretation of experimental data for various materials. As can be seen from these expressions, the photoacoustic piezoelectric reveals inhomogeneities of the thermoelastic coupling coefficient near the sample surface. It can be also seen that, by moving the point of laser action over the sample surface, it is possible to image the inhomogeneities of the thermoelastic coupling coefficient at a resolution determined by the thermal wavelength. Previously [14–17], it was pointed out that the thermoelastic coupling coefficient depends, for example, on the internal stresses. Therefore, the obtained results imply that the photoacoustic images obtained under such conditions will reflect the distribution of internal stresses near the sample surface, while formulas (9) can be used for an analysis of the character of this distribution and for evaluation of the magnitude of internal stresses in the sample.

REFERENCES

1. A. Rosencwaig, in *Progress in Photothermal and Photoacoustic Science and Technology*, Ed. by A. Mandelis (PTR Prentice-Hall, New Jersey, 1994), Vol. 2, pp. 1–23.

2. J. Jumel, D. Rochais, F. Enguehard, and F. Lepoutre, Rev. Sci. Instrum. **74**, 608 (2003).

3. R. M. Burbelo, A. L. Gulyaev, A. G. Kuz'mich, and I. Ya. Kucherov, Zh. Tekh. Fiz. **66** (4), 121 (1996) [Tech. Phys. **41**, 361 (1996)].

4. A. L. Glazov and K. L. Muratikov, Zh. Tekh. Fiz. **57**, 2184 (1987) [Sov. Phys. Tech. Phys. **32**, 1320 (1987)].

5. S. K. Likharev and E. I. Rau, Izv. Akad. Nauk SSSR, Ser. Fiz. **54**, 255 (1990).

6. F. Depasse, Ph. Grossel, and W. S. Gomes, J. Phys. D **36**, 204 (2003).

7. K. L. Muratikov, Pis'ma Zh. Tekh. Fiz. **30** (22), 58 (2004) [Tech. Phys. Lett. **30**, 956 (2004)].

8. L. D. Landau and E. M. Lifshitz, *Course of Theoretical Physics*, Vol. 7: *Theory of Elasticity* (Nauka, Moscow, 1987; Pergamon, New York, 1986).

9. S. P. Timoshenko and J. N. Goodier, *Theory of Elasticity*, 3rd ed. (McGraw-Hill, New York, 1970).

10. W. Jackson and N. M. Amer, J. Appl. Phys. **51**, 3343 (1980).

11. M. Qian, Chin. J. Acoust. **14**, 97 (1995).

12. K. L. Muratikov, Pis'ma Zh. Tekh. Fiz. **24** (13), 82 (1998) [Tech. Phys. Lett. **24**, 536 (1998)].

13. K. L. Muratikov, Zh. Tekh. Fiz. **69** (7), 59 (1999) [Tech. Phys. **44**, 792 (1999)].

14. K. L. Muratikov and A. L. Glazov, Zh. Tekh. Fiz. **70** (8), 69 (2000) [Tech. Phys. **45**, 1025 (2000)].

15. K. L. Muratikov, A. L. Glazov, D. N. Rose, and J. E. Dumar, J. Appl. Phys. **88**, 2948 (2000).

16. K. L. Muratikov, A. L. Glazov, D. N. Rose, and D. E. Dumar, Pis'ma Zh. Tekh. Fiz. **28** (9), 48 (2002) [Tech. Phys. Lett. **28**, 377 (2002)].

17. K. L. Muratikov and A. L. Glazov, Zh. Tekh. Fiz. **73** (8), 90 (2003) [Tech. Phys. **48**, 1028 (2003)].

18. K. L. Muratikov, Rev. Sci. Instrum. **74**, 3531 (2003).

Translated by P. Pozdeev

Forming Composites Based on Mineral Fibers

V. K. Dubovyĭ[a], E. I. Ivanova[a], V. I. Ivanov-Omskiĭ[b,*], and V. B. Skupchenko[b]

[a] St. Petersburg State Academy of Forestry, St. Petersburg, Russia
[b] Ioffe Physicotechnical Institute, Russian Academy of Sciences, St. Petersburg, 194021 Russia
* e-mail: ivanov.ivom@mail.ioffe.ru
Received May 25, 2005

Abstract—The effect of aluminum sulfate additives on the structure of a composite material based on basalt fibers has been studied using electron microscopy and IR spectroscopy. The introduction of aluminum sulfate leads to the appearance of outgrowths fastening mineral fibers to each other at their intersection contacts. This is accompanied by the appearance of an absorption band in the IR spectra, which is attributed to hydrogen-bonded hydroxy groups. Estimates of the hydrogen bond lengths are obtained from an analysis of the IR absorption band shape. © 2005 Pleiades Publishing, Inc.

Composites based on mineral fibers are widely used in the production of various paper materials for technical applications [1, 2]. It was empirically established that the strength of such composites can be increased by adding aluminum sulfate to a mineral-fiber mass in a neutral or weakly alkaline medium, but the mechanism of this reinforcement is still incompletely clear. It is obvious that knowledge of this mechanism will offer new possibilities in the development of methods for controlled and automated production of composites based on mineral fibers.

In order to elucidate the mechanism of composite reinforcement in the presence of aluminum compounds, we prepared a series of samples based on basalt fibers on a LOA-2 plate-casting machine and studied their structures using transmission electron microscopy (TEM) and IR spectroscopy.

Figure 1 shows the TEM images of basalt fibers, which were examined before and after the introduction of aluminum sulfate (80% as calculated for Al_2O_3). As can be seen, basalt fibers in the material free of aluminum sulfate are arranged practically independently of each other. Upon the introduction of aluminum sulfate, there appear outgrowths of polynuclear aluminum complexes, which fasten the mineral fibers to each other at their intersection contacts.

Information concerning the mechanism of this fastening can be obtained by studying the IR absorption spectra of samples prepared with and without aluminum sulfate additives in the aqueous suspension of min-
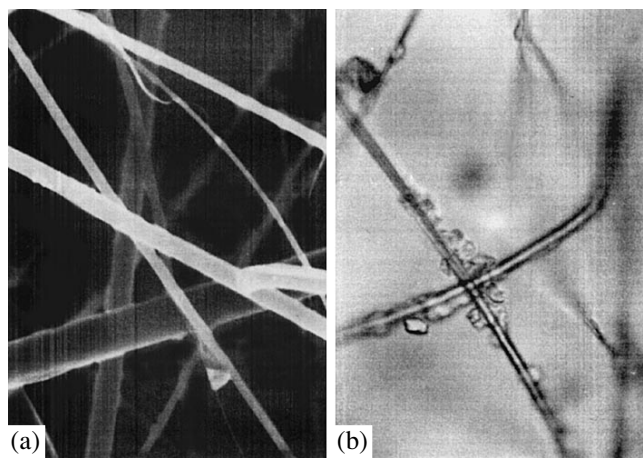

Fig. 1. TEM micrographs of basalt fibers (a) before and (b) after the introduction of aluminum sulfate (80% as calculated for Al_2O_3). Magnification: (a) ×4000; (b) ×1181.
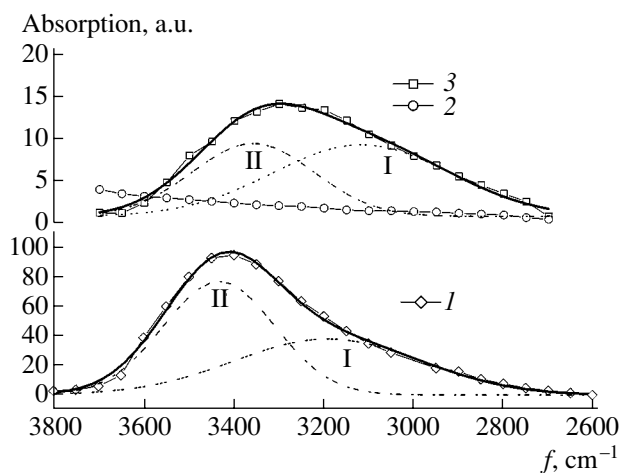

Fig. 2. Fragments of the IR spectra with decomposition into Gaussian components I and II: (*1*) aluminum sulfate; (*2*) basalt fibers; (*3*) basalt fibers after introduction of aluminum sulfate. Thick solid curve shows a sum of the Gaussian components I and II.

Parameters of decomposition of experimental IR absorption bands into Gaussian components (Fig. 2)

Sample	Frequencies of Gaussian components		H-Bond length		Relative content of "strong" H-bonds (d_1/d_2)
	Peak I, cm^{-1}	Peak II, cm^{-1}	d_1, Å	d_2, Å	
Basalt (surface density, 6.5 g/m^2)	3117 ± 137	3358 ± 34	2.68 ± 0.04	2.77 ± 0.02	1.42
Aluminum sulfate (pressed into KBr)	3191 ± 81	3432 ± 6	2.70 ± 0.03	2.82 ± 0.01	0.83

eral fibers. For this purpose, we specially prepared a series of castings with a low mass per square meter and a thickness of 0.2–0.3 mm and measured their IR absorption spectra in the transmission mode. Figure 2 shows the fragments of the IR spectra in the region of absorption by hydroxy groups. As can be seen, the introduction of aluminum sulfate into the aqueous suspension of mineral fibers led to the appearance of a rather broad absorption band in the region of 3800–2600 cm^{-1}, which is characteristic of the hydrogen-bonded hydroxy groups.

As is known, a characteristic feature of aluminum sulfate is the ability of this compound to form polyhydroxocomplexes involving numerous hydroxy groups. This is manifested by a broad absorption band related to the vibrations of hydroxy groups (Fig. 2, curve *1*). A compact mutual arrangement of the hydroxy groups favors the formation of stable hydrogen bonds (H-bonds) binding primarily the internal hydroxy groups of the polyhydroxocomplex and thus determining its strength. However, if structural components with proton acceptors (e.g., oxygen atoms) occur in a close vicinity of the polyhydroxocomplex particles, these components are also involved in the H-bonds. Therefore, we may suggest that an aqueous solution of aluminum sulfate acts according to this very mechanism as a binding agent in mineral fiber composites whose structures usually contain bound oxygen.

An analysis of the shape of the absorption band due to H-bonded hydroxy groups can provide an estimate of the H-bond length (O–H···O) in polynuclear aluminum complexes and related mineral fibers. For this purpose, we have decomposed the experimental absorption bands into Gaussian components I and II with the parameters listed in the table. The H-bond length was estimated using the method described in [3], according to which the frequency of the band component is related to the characteristic bond length, while the band intensity is related to the concentration of such bonds. As can be seen from data in the table, the H-bond structures in the polyhydroxocomplex and in the composite are approximately the same. However, the relative concentrations of short and long bonds differ, so that the composite contains predominantly the short bonds. This fact can be related to the enhancement of H-bonds in the composite. Thus, the H-bonds play a significant role in the formation of composites based on mineral fibers and containing the products of aluminum sulfate hydrolysis.

REFERENCES

1. V. K. Dubovyĭ and G. I. Chizhov, Tsellyuloza, Bumaga, Karton, No. 10, 4 (2004).
2. V. K. Dubovyĭ and G. I. Chizhov, Tsellyuloza, Bumaga, Karton, No. 2, 3 (2005).
3. V. I. Ivanov-Omskiĭ, Pis'ma Zh. Tekh. Fiz. **26** (12), 51 (2000) [Tech. Phys. Lett. **26**, 520 (2000)].

Translated by P. Pozdeev

The Effect of Illumination on the Current–Voltage Characteristics and Conductivity of MnIn$_2$S$_4$ Single Crystals

N. N. Niftiev and O. B. Tagiev

Azerbaijan State Pedagogical University, Baku, Azerbaijan
Revised manuscript received May 24, 2005

Abstract—The effect of illumination on the current–voltage (J–U) characteristics and the temperature dependence of conductivity $\sigma(T)$ of MnIn$_2$S$_4$ single crystals has been studied. Under illumination, the J–U curves can be divided into three parts corresponding to the linear ($J \sim U$), "3/2" ($J \sim U^{1.5}$) and "5/2" ($J \sim U^{2.5}$) laws. This behavior is explained by an increase in the density of free charge carriers under the joint action of electric field and illumination. The current J_1 in the illuminated sample is 10^4–10^5 times the dark J_2 value. The positions of energy levels in the semiconductor crystal under study are determined. © *2005 Pleiades Publishing, Inc.*

This Letter presents the results of investigation of the effect of illumination on the current–voltage (J–U) characteristics and the temperature dependence of conductivity in MnIn$_2$S$_4$ single crystals grown from by means of chemical vapor transport reactions. The X-ray diffraction measurements showed that the obtained singe crystal has a cubic structure (space group, $Fd3m$) a unit cell parameter of $a = 10.71$ Å [1]. The electrical measurements were performed on sandwich structures with fused indium contacts.

Figure 1 shows the typical J–U characteristics of an In–MnIn$_2$S$_4$–In structure measured at 293 K in the dark (curve *1*), in the dark after preliminary illumination (curve *2*), and under constant exposure to a white light (curve *3*). As can be seen, the J–U curve measured in the dark (curve *1*) can be divided into three parts corresponding to a linear increase ($J \sim U$), a quadratic growth ($J \sim U^2$), and a cubic buildup ($J \sim U^3$). Previously, we have established [2] that the current generation in the quadratic region is due to a single-type (unipolar) carrier injection, while the cubic buildup region is due to the double carrier injection. Upon preliminary illumination, the J–U curve exhibits a linear portion ($J \sim U$) and a region where $J \sim U^{3/2}$. In a sample illuminated by white light, the photogenerated electrons are captured by traps and the generated holes are trapped by recombination centers, which results in the electron transitions from valence to conduction band and in the appearance of free charge carriers. The J–U curves measured upon termination of the exposure and keeping the sample for some time in the dark show that the current in such a preilluminated crystal is about 10^2 times that in the nonilluminated one. The additional conductivity is provided by nonequilibrium charge carriers [3].

The J–U characteristic observed under constant illumination (Fig. 1, curve *3*) can be divided into three part corresponding to the linear ($J \sim U$), "3/2" ($J \sim U^{1.5}$) and "5/2" ($J \sim U^{2.5}$) laws. This behavior can be explained by assuming that the joint action of the applied electric field and illumination leads to an increase in the probability of the appearance of free electrons in the conduc-
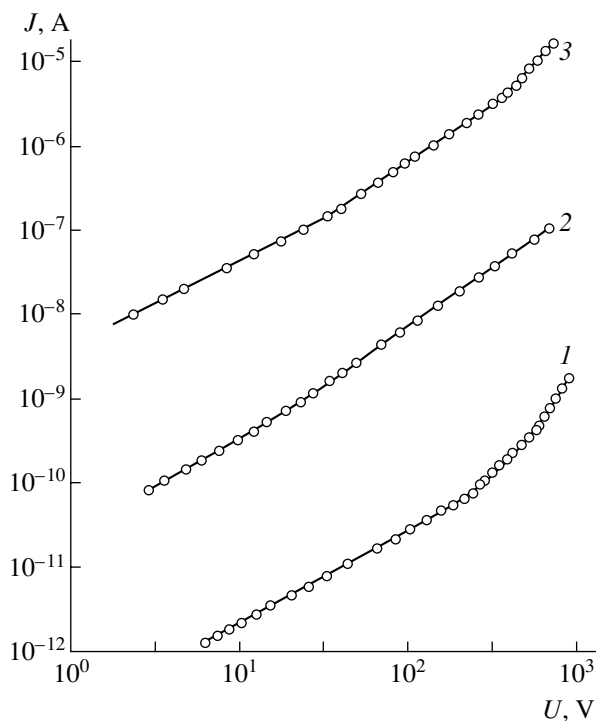

Fig. 1. The typical J–U curves of an In–MnIn$_2$S$_4$–In structure measured at 293 K (*1*) in the dark, (*2*) in the dark after preliminary illumination, and (*3*) under constant exposure to a white light (200 Lx).
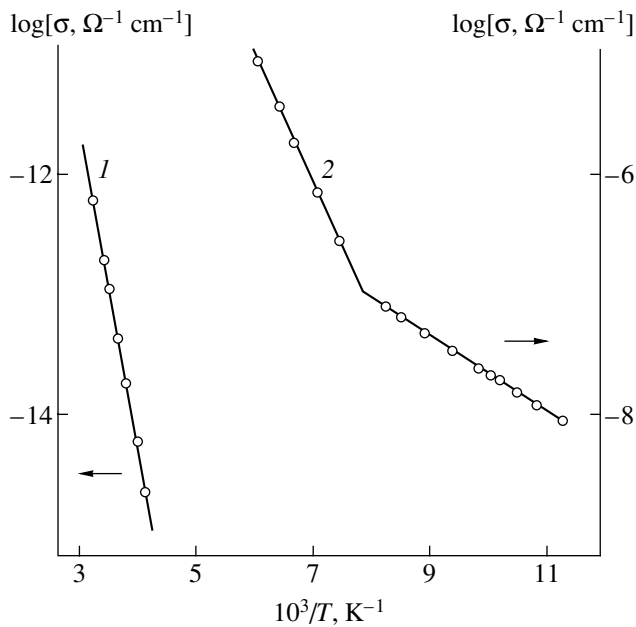
log[σ, Ω⁻¹ cm⁻¹]　　　　　log[σ, Ω⁻¹ cm⁻¹]

Fig. 2. Temperature dependences of the electric conductivity of a MnIn$_2$S$_4$ single crystal measured (*1*) in the dark and (*2*) under illumination with white light (3.5×10^3 Lx).

Figure 2 shows the temperature dependences of the electric conductivity σ of MnIn$_2$S$_4$ single crystals measured in the dark (curve *1*) and under illumination with white light (curve *2*). As can be seen, the conductivity in a low-temperature region is significantly higher under illumination than in the dark. The log σ versus inverse temperature plots for the illuminated single crystal reveals two regions with different activation energies $E = 0.065$ and 0.21 eV, while the entire curve measured in the dark has a single slope corresponding to $E = 0.53$ eV. It should be noted that virtually the same energy levels were also revealed by data on the thermo-stimulated currents [5].

To summarize, we have experimentally studied the effect of illumination on the *J–U* characteristic and the conductivity σ(*T*) of MnIn$_2$S$_4$ single crystals and established that *J–U* curves exhibit three parts corresponding to the linear ($J \sim U$), "3/2" ($J \sim U^{1.5}$) and "5/2" ($J \sim U^{2.5}$) laws. This behavior is explained by features of the charge carrier generation and trapping under the joint action of applied field and illumination. The current J_1 in the illuminated sample is about 10^5 times the dark J_2 value. The positions of energy levels in the semiconductor crystal under study are determined.

tion band, and of the free holes in the valence band, charge carrier generation under. As can be seen, the current J_1 in the illuminated sample was 10^4–10^5 times the dark J_2 value. The $J \sim U^{2.5}$ region observed for the illuminated sample corresponds to the quadratic region in the characteristic of a sample measured in the dark. The illumination of a sample featuring the current due to unipolar injection can lead to an increase in the space charge limited current, provided that a part of the space charge is trapped and that carriers in the traps can absorb the energy of incident light. In particular, the trapped carrier can directly absorb a light quantum and pass to an allowed energy band [4].

REFERENCES

1. T. Kanamato, H. Ido, and T. Kaneko, Jpn. J. Phys. **34**, 554 (1973).
2. N. N. Niftiyev and O. B. Tagiev, Solid State Commun. **81**, 693 (1992).
3. R. H. Bube, *Photoconductivity of Solids* (Wiley, New York, 1960).
4. M. A. Lampert and P. Mark, *Current Injection in Solids* (Academic Press, New York, 1970; Mir, Moscow, 1973), p. 473.
5. N. N. Niftiev, Fiz. Tekh. Poluprovodn. (St. Petersburg) **36**, 836 (2002) [Semiconductors **36**, 782 (2002)].

Translated by P. Pozdeev

Relationship between Phase Synchronization
of Chaotic Oscillators and Time Scale Synchronization

A. A. Koronovskiĭ*, M. K. Kurovskaya, and A. E. Hramov**

Saratov State University, Saratov, Russia
*e-mail: * alkor@cas.ssu.runnet.ru; ** aeh@cas.ssu.runnet.ru*
Received April 19, 2005

Abstract—The relationship between the phase synchronization of chaotic oscillators and their time scale synchronization has been considered, and it is established that the onset of the time scale synchronization depends on the resolving power of the base wavelet. This synchronization usually appears either before or (if said resolving power is insufficient) simultaneously with the onset of phase synchronization. The results are illustrated in the case of one-way coupled Rössler type dynamical systems. © *2005 Pleiades Publishing, Inc.*

Chaotic synchronization of dynamical systems is among basic nonlinear phenomena which have been extensively studied in recent years [1] and are also of considerable practical importance. The development of the theory of dynamical chaos revealed various types of synchronous chaotic behavior of coupled dynamical systems, including the phase [1], generalized [2], lag [3], and complete synchronization [4]. Each particular type of synchronous chaotic dynamics has its own distinctive features, but the question of the relationships between various types of synchronous behavior has been also actively discussed in recent years. Indeed, various forms or synchronization of coupled chaotic oscillators can be considered as manifestations of certain general laws valid for coupled nonlinear systems (see, e.g., [5–7]).

Recently, we have demonstrated [8–10] that all the aforementioned types of synchronous chaotic behavior can be considered as partial cases of the same type of synchronous dynamics referred to as the time scale synchronization. For example, it was found that, if two coupled chaotic oscillators occur in the regime of phase synchronization, then the time scale synchronization can be revealed as well. The inverse statement is generally not valid and it is quite a typical situation when the coupled chaotic oscillators exhibit signs of the time scale synchronization, while the phase synchronization is not observed (see [8, 9, 11]).

The aim of this study was to establish a relationship between the phase synchronization of chaotic oscillators and their time scale synchronization. In particular, we studied the mutual arrangement of the boundaries of these regimes on the plane of control parameters (drive frequency–coupling parameter) of two coupled oscillators.

The phenomenon of phase synchronization is usually described and analyzed in terms of the phase $\phi(t)$ of the chaotic signal [1, 12–16]. The phase synchronization of chaotic signals implies entrainment of their phases, while the amplitudes remain mutually independent and appear as chaotic. The entrainment of phases leads to coincidence of the frequencies of chaotic signals (the characteristic frequency of a chaotic signal is defined as the average rate $\langle \dot{\phi}(t) \rangle$ of phase variation).

There are several methods of introducing the phase of chaotic oscillations, which are applicable to systems with a simple topology of chaotic attractors (i.e., with phase-coherent attractors). First, the phase $\phi(t)$ of a chaotic signal can be defined as an angle in the polar coordinate system on the (x, y) plane [3, 17]. However, in this case, all trajectories of the projection of the chaotic attractor onto the (x, y) plane will rotate around the origin. Sometimes it is possible to use a transformation of coordinates in order to obtain a projection suited for the phase introduction [1, 17]; otherwise, it is possible to consider the system dynamics on the plane of velocities $(\dot{x}, \dot{y})$ [18]. Another way of defining the phase on a chaotic dynamical system is based on the introduction of an analytical signal [12, 14] with the aid of the Hilbert transform. Finally, the phase of a chaotic signal can be introduced with the aid of the Poincaré cross section [12, 14]. All these approaches give similar correct results for the systems with phase-coherent attractors [17]. On the other hand, these methods frequently lead to incorrect results when applied to the systems with poorly defined phase (see, e.g., [1, 19]). For this reason, the phase synchronization of such a system can be revealed in some cases by means of indirect observations [17, 20] and measurements [21], although there are cases where the presence or absence of phase synchronization cannot be practically established.
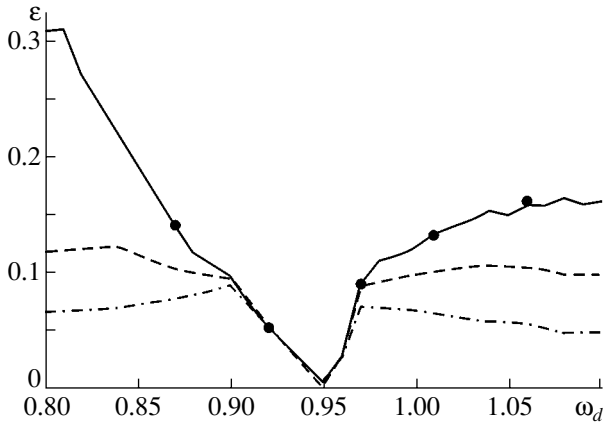
The plane of control parameters (ω_d, ε) for two one-way coupled chaotic Rössler oscillators (3). Solid curve shows the boundary of the onset of phase synchronization of chaotic oscillators; dashed curve shows the boundary of the time scale synchronization for the Morlet wavelet parameter $\Omega = 2\pi$, and dash-dot curve shows this boundary for $\Omega = 16$; points indicate the boundary of the time scale synchronization as determined by analysis using the Morlet wavelet parameter $\Omega = 0.05$.

The regime of time scale synchronization [8–11] is usually described in terms of the time scales s introduced using a continuous wavelet transform with a base wavelet function of the Morlet type (see, e.g., [22]):

$$\psi_0(\eta) = \frac{1}{\sqrt[4]{\pi}} \exp(j\Omega\eta) \exp\left(-\frac{\eta^2}{2}\right). \tag{1}$$

Each time scale s is characterized by the corresponding instantaneous phase $\phi_s(t) = \arg W(s, t)$, where $W(s, t)$ is the complex wavelet surface. In these terms, the phenomenon of time scale synchronization of coupled chaotic systems is manifested by the synchronous behavior of phases $\phi_{s1, 2}(t)$ of the first and second oscillator, respectively, observed in the interval of synchronized time scales $s_m < s < s_b$. Each time scale s from this interval obeys the condition of phase entrainment

$$\left|\phi_{s1}(t) - \phi_{s2}(t)\right| < \text{const}, \tag{2}$$

and the energy fraction of the wavelet spectrum in said interval is nonzero. Since the base wavelet (1) depends on the parameter Ω, it is important to study the influence of this parameter on the possibility to determine the boundary of the regime of time scale synchronization.

Let us consider the problem of the relationship between the phase synchronization and the time scale synchronization in the case of two one-way coupled chaotic oscillators representing Rössler systems with slightly mismatched parameters:

$$\dot{x}_d = -\omega_d y_d - z_d, \quad \dot{x}_r = -\omega_r y_r - z_r + \varepsilon(x_d - x_r),$$

$$\dot{y}_d = \omega_d x_d + a y_d, \quad \dot{y}_r = \omega_r x_r + a y_r, \tag{3}$$

$$\dot{z}_d = p + z_d(x_d - c), \quad \dot{z}_r = p + z_r(x_r - c),$$

where ε is the coupling parameter. The values of the control parameters are selected by analogy with those used in [23]: $a = 0.15$, $p = 0.2$, and $c = 10.0$. The control parameter of the driven (response) system, $\omega_r = 0.95$, which characterizes its fundamental frequency, is fixed. The analogous parameter of the drive system ω_d is varied in the interval from 0.8 to 1.1, which corresponds to a slight mismatch of the two oscillators. It is known that, for the selected values of control parameters, the chaotic attractors of interacting oscillators are phase-coherent (except for small regions on the (ω_d, ε) plane not having significant influence on the final results), which makes possible correct introduction of the phase of chaotic signals and reliable detection of the regime of phase synchronization.

The boundary of the region corresponding to the onset of phase synchronization on the plane of control parameters (ω_d, ε) for the system under consideration is shown in the figure. The appearance of phase synchronization was determined by the condition of entrainment of phases of the drive and response oscillators (3). The phases were defined as the polar angles in the coordinate systems on (x_d, y_d) and (x_r, y_r) planes. It should be noted that the boundary of the region of phase synchronization in cases when the phase was introduced in terms of the Hilbert transform or as the polar angle on the ($\dot{x}$, $\dot{y}$) plane virtually coincided with that presented in the figure, which is related to the good topology of the chaotic attractor in the system studied. As can be seen, the region of phase synchronization has the shape of a "tong," which touches the point (ω_r, 0) on the plane of control parameters (ω_d, ε) and then expands with increasing coupling parameter ε.

The same diagram shows a boundary corresponding to the onset of time scale synchronization for the base Morlet wavelet parameter $\Omega = 2\pi$. This choice (proposed in [8, 9, 11]) is determined by the fact that it provides for a simple and natural relationship between the time scale s and the frequency f of the corresponding Fourier spectrum: $s = 1/f$. For other values of Ω, relations between the frequency and the time scale are more involved (for detail, see [22]).

In the case of a relatively large mismatch between the parameters of interacting oscillators (see the figure), the regime of time scale synchronization is observed at lower values of ε as compared to that corresponding to the onset of phase synchronization. In the case of a small mismatch, the boundaries of the onset of both types of chaotic synchronization practically coincide.

This behavior is related to the resolving power of the wavelet function for a given value of Ω: as long as the detuning of frequencies of the drive and response oscillators is small, the synchronous behavior of both systems on the time scale s_1 (corresponding to the fundamental frequency in the Fourier spectrum of the drive system) can be "masked" by asynchronous dynamics on a time scale s_2 corresponding to the fundamental frequency of the response system [22]. For this reason, asynchronous behavior on both s_1 and s_2 scales will be observed unless the asynchronous dynamics on the s_2 scale is not completely suppressed by the synchronous dynamics on the s_1 scale, which corresponds to establishment of the regime of phase synchronization.

As the mismatch between the drive and response oscillators increases, the interval between the time scales s_1 and s_2 grows accordingly and the dynamics on these scales can be distinguished with the aid of the wavelet function. For this reason, the threshold of the onset of time scale synchronization for a large ω_d–ω_r difference is detected before the phase synchronization threshold.

An increase in the parameter Ω leads to an increase in the resolving power of the Morlet wavelet function (see, e.g., [22]), which makes possible the detection of fine details in the synchronous dynamics. Therefore, the threshold of the onset of time scale synchronization must shift toward lower values of the coupling parameter ε with increasing Ω and, on the contrary, a decrease in Ω will shift the threshold of detection of the regime of time scale synchronization toward greater ε values. Simultaneously, a decrease in Ω is accompanied by expansion of a region on the plane of control parameters (ω_d, ε) in which the boundaries of the time scale synchronization and the phase synchronization coincide. This is illustrated in the figure, which also shows a boundary of the time scale synchronization determined using the Morlet wavelet function with $\Omega = 16$. As can be seen, the time scale synchronization in this case is detected earlier than in the case of $\Omega = 2\pi$.

For comparison, the diagram also shows a boundary of the time scale synchronization determined using a Morlet wavelet function with a very poor resolving power, which corresponds to $\Omega = 0.5$. In this case, the boundary of the time scale synchronization is detected virtually simultaneously with the onset of phase synchronization even for a relatively large mismatch between the parameters of interacting oscillators. Thus, an analysis of the behavior of coupled chaotic oscillators with the aid of the Morlet wavelet with a poor resolving power (small Ω) makes possible the detection of the boundary of the time scale synchronization even for a relative large mismatch between the two coupled oscillators. In such cases, the phase coherence (or its absence) of the chaotic attractor is probably not as important. In particular, for a system of two coupled Rössler oscillators described in [21] with a coupling parameter of $\varepsilon = 0.05$, a synchronous regime can be detected using a Morlet wavelet with $\Omega = 0.5$ even despite the fact that the chaotic attractor is not phase-coherent (in [21], the synchronous regime was detected by passing to the $(\dot{x}, \dot{y})$ plane)).

In conclusion, we have studied a relationship between the phase synchronization of chaotic oscillators and their time scale synchronization and determined the role of selection of the Morlet wavelet parameter on the detection of synchronous regimes in a system of coupled oscillators.

REFERENCES

1. A. Pikovsky, M. Rosenblum, and J. Kurths, *Synchronization: A Universal Concept in Nonlinear Sciences* (Cambridge Univ. Press, Cambridge, 2001).

2. N. F. Rulkov, M. M. Sushchik, L. S. Tsimring, and H. D. I. Abarbanel, Phys. Rev. E **51**, 980 (1995).

3. M. G. Rosenblum, A. S. Pikovsky, and J. Kurths, Phys. Rev. Lett. **78**, 4193 (1997).

4. L. M. Pecora and T. L. Carroll, Phys. Rev. A **44**, 2374 (1991).

5. S. Boccaletti, L. M. Pecora, and A. Pelaez, Phys. Rev. E **63**, 066219 (2001).

6. R. Brown and L. Kocarev, Chaos **10**, 344 (2000).

7. A. A. Koronovskiĭ and A. E. Hramov, Pis'ma Zh. Éksp. Teor. Fiz. **79**, 391 (2004) [JETP Lett. **79**, 316 (2004)].

8. A. E. Hramov and A. A. Koronovskiĭ, Chaos **14**, 603 (2004).

9. A. A. Koronovskiĭ, O. I. Moskalenko, and A. E. Hramov, Pis'ma Zh. Éksp. Teor. Fiz. **80**, 25 (2004) [JETP Lett. **80**, 20 (2004)].

10. A. E. Hramov, A. A. Koronovskiĭ, and Yu. I. Levin, Zh. Éksp. Teor. Fiz. **127**, 886 (2005) [JETP **100**, 784 (2005)].

11. A. E. Hramov, A. A. Koronovskiĭ, P. V. Popov, and I. S. Rempen, Chaos **15**, 013705 (2005).

12. M. G. Rosenblum, A. S. Pikovsky, and J. Kurths, Phys. Rev. Lett. **76**, 1804 (1996).

13. G. V. Osipov, A. S. Pikovsky, M. G. Rosenblum, and J. Kurth, Phys. Rev. E **55**, 2353 (1997).

14. A. Pikovsky, M. Rosenblum, and J. Kurths, Int. J. Bifurcation Chaos Appl. Sci. Eng. **10**, 2291 (2000).

15. V. S. Anishchenko and T. E. Vadivasova, J. Commun. Technol. Electron. **47**, 117 (2002).

16. V. S. Anishchenko, V. Astakhov, A. Neiman, T. Vadivasova, and L. Schimansky-Geier, *Nonlinear Dynamics of Chaotic and Stochastic Systems. Tutorial and Modern Developments* (Springer, Heidelberg, 2002).

17. A. Pikovsky, M. Rosenblum, G. Osipov, and J. Kurths, Physica D **104**, 219 (1997).

18. G. V. Osipov *et al.*, Phys. Rev. Lett. **91**, 024101 (2003).

19. V. S. Anishchenko and T. E. Vadivasova, J. Commun. Technol. Electron. **49**, 69 (2004).

20. A. S. Pikovsky, M. G. Rosenblum, and J. Kurths, Europhys. Lett. **34**, 165 (1996).

21. M. G. Rosenblum, A. S. Pikovsky, J. Kurths, *et al.*, Phys. Rev. Lett. **89**, 264 102 (2002).

22. A. A. Koronovskiĭ and A. E. Hramov, *Continuous Wavelet Analysis and Its Applications* (Fizmatlit, Moscow, 2003) [in Russian].

23. Z. Zheng and G. Hu, Phys. Rev. E **62**, 7882 (2000).

Translated by P. Pozdeev

The Role of Magnetostatic Interactions in the Phenomenon of Thermal Magnetization of Highly Anisotropic Fine-Grained Magnetic Alloys

M. V. Pletneva, Yu. V. Tolstobrov, and N. A. Manakov

Biysk State Pedagogical University, Biysk, Russia
e-mail: rektor@bigpi.biysk.ru
Received April 19, 2005

Abstract—The phenomenon of thermal magnetization of fine-grained alloys has been studied by micromagnetic modeling in a multilayer stochastic system. It is established that thermal magnetization in this system is manifested in a certain temperature interval. The mechanism of this effect is different from that stipulated by the Zaitsev–Lileev model. © *2005 Pleiades Publishing, Inc.*

According to the Zaitsev–Lileev model [1, 2], the phenomenon of thermal magnetization is explained by the presence of microdomains with different values of the anisotropy constant K in the initially demagnetized material. Heating the sample leads to a decrease in these constants and to an increase in the role of magnetostatic interactions. As a result, the magnetization vectors of microdomains with small K values are aligned in the direction of magnetization in the microdomains with large K, which is manifested by the magnetization of the whole sample. It is believed that the final distribution of magnetization is energetically more favorable than the initial state, so that the heating-induced magnetization is retained upon cooling of the sample.

Recently, we proposed [3] an alternative explanation of the thermal magnetization phenomenon. According to the developed model of a multilayer stochastic system composed of infinite uniaxial magnetic layers, the heating-induced magnetization is due to the exchange interaction between these layers in the absence of an external magnetostatic field [3].

In this study, we checked the role of magnetostatic interactions for a model comprising 50 magnetic layers separated by nonmagnetic interlayers (spacers), which excluded the exchange interaction between the magnetic layers. The easy magnetization axes were oriented perpendicularly to the magnetic layers.

A simplified schematic diagram of the model system comprising four magnetic layers without spacers is depicted in the figure. The Cartesian coordinate system is oriented so that the $x0y$ plane is parallel, and the $0z$ axis is perpendicular to the magnetic layers. The magnetization vector **M** and the system parameters are considered as functions of the z coordinate. The free

energy functional G of the system under consideration can be written in a dimensionless form as

$$G = \int_0^1 \left\{ \frac{A}{M_S^2 L^2} \left[\left(\frac{\partial m^x}{\partial z} \right)^2 + \left(\frac{\partial m^y}{\partial z} \right)^2 + \left(\frac{\partial m^z}{\partial z} \right)^2 \right] \right.$$
$$\left. + \frac{K}{M_S^2}(1 - (m^z)^2) + \frac{1}{2}m^z U' \right\}dz, \quad (1)$$

where the integrand comprises a sum of the energy densities due to exchange, anisotropy, and magnetostatic interactions. Here, $M_S = |\mathbf{M}|$ is the saturation magneti-
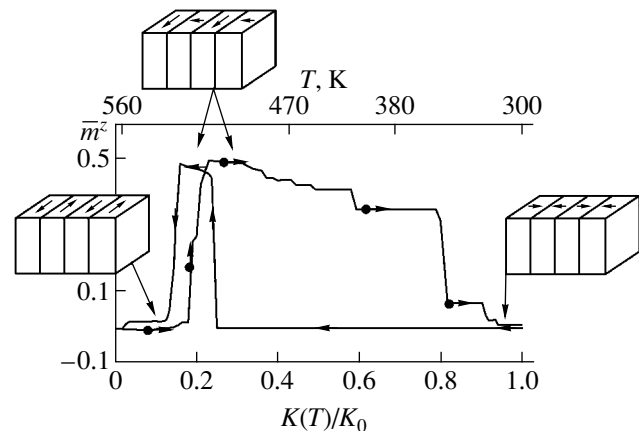
Temperature-induced variation of the magnetization $\overline{m}^z = \int_0^1 m^z(z)dz$ and relative anisotropy $K(T)/K_0$ in a system of 50 layers with thicknesses $d = 2.685$ nm. The arrows (———) and (●———) indicate the direction of changes in the course of heating and cooling, respectively. The insets schematically illustrate the rotation of magnetization vectors in a simplified four-layer model.

zation, $\mathbf{m} = \mathbf{M}/M_S = (m^x, m^y, m^z)$ is the unit vector parallel to the magnetization $\mathbf{M}$, A is the exchange constant, K is the anisotropy constant; U' is the derivative of the magnetostatic field potential with respect to the z coordinate, L is the multilayer system thickness, and $z = 0$ and $z = 1$ are the left and right boundaries of the system (the dimensionless coordinates are expressed in the L units).

The magnetostatic field potential for a certain distribution of the magnetization is described by the following system of equations:

$$U'' = \begin{cases} 4\pi\dfrac{\partial m^z}{\partial z} & \text{(inside magnetic layers)}, \\ 0 & \text{(outside magnetic layers)}; \end{cases} \quad (2)$$

$$\frac{\partial U}{\partial \mathbf{n}} + \frac{\partial U}{\partial(-\mathbf{n})} = -4\pi\mathbf{m}\cdot\mathbf{n} \quad (3)$$

(on the boundaries between layers),

where $\mathbf{n}$ is the unit vector of the normal to the surface of layers.

The problem of determining an equilibrium distribution of the magnetization reduces to finding a local minimum of the free energy functional (1) under conditions (2) and (3). It was assumed that the system evolves so as to provide for the steepest decrease in the free energy. In terms of the numerical modeling, this corresponds to using the method of steepest descent for a discrete analog of the energy functional (1) considered as the function of a finite number of variables.

In order to study the phenomenon of thermal (re)magnetization in the model system under consideration, we have set a completely demagnetized initial state, whereby the magnetization vectors in the adjacent layers were antiparallel and their anisotropy constants acquired the alternating values of K and $K/2$. The temperature variation was expressed via the temperature dependence of K, while the other parameters of the system remained unchanged. In the course of modeling, the relative value of the anisotropy K/K_0 (where K_0 is the K value at $T = 293$ K) decreased from 1 to 0.01 and then increased to the initial value. The corresponding interval of temperature variation for $Nd_2Fe_{14}B$ is depicted in the figure [4].

The results of modeling showed that, as the temperature increases, the system acquired nonzero magnetization because vectors $\mathbf{M}$ of the layers with small anisotropy exhibited rotation to become parallel to these layers. This rotation corresponded to a decrease in the free energy of the system due to a significant reduction in the magnetostatic energy component even at a certain increase in the anisotropy energy (see figure). As the temperature was increased further, the magnetization vectors $\mathbf{M}$ of the layers with large anisotropy also exhibited rotation and acquired the in-plane orientation. As a result, the sample became completely demagnetized. In the course of cooling, orientations of the magnetization vectors of neighboring layers change in the reverse direction, but a nonzero magnetization is observed in a much wider temperature interval. Eventually, the system returns to the initial demagnetized state. The reason for this behavior is that the states in which the magnetization vectors of the adjacent layers are oriented in the opposite directions are energetically more favorable than the states with their parallel orientation. Therefore, the mechanism according to which the magnetization of low-anisotropy layers tends to align in the direction of magnetization of the high-anisotropy layers in not operative in the system studied. The behavior analogous to those depicted in the figure was also observed for the systems with layer thicknesses $d = 5.37$ and 10.74 nm.

REFERENCES

1. A. A. Zaĭtsev, A. S. Lileev, and V. A. Sein, Izv. Vyssh. Uchebn. Zaved., Chern. Metall., No. 11, 82 (1988).

2. B. G. Livshits, A. S. Lileev, G. V. Abal'yan, *et al.*, Izv. Vyssh. Uchebn. Zaved., Chern. Metall., No. 11, 131 (1976).

3. N. A. Manakov, M. V. Pletneva, and Yu. V. Tolstobrov, Fiz. Met. Metalloved. **99** (1), 14 (2005).

4. A. Higuchi and H. Satoshi, IEEE Trans. Magn. **25**, 3555 (1989).

Translated by P. Pozdeev

Generator of Quasi-Periodic Oscillations Featuring Two-Dimensional Torus Doubling Bifurcations

V. S. Anishchenko* and S. M. Nikolaev

Saratov State University, Saratov, Russia

* *e-mail: wadim@chaos.ssu.runnet.ru*

Received April 8, 2005

Abstract—A new autonomous differential dynamical system with dimension $N = 4$ is introduced, which has solutions in the form of stable two-frequency oscillations and features a sequence of period-doubling bifurcations of two-dimensional ergodic tori. At the points of period-doubling bifurcations, no resonances are observed on a torus and only ergodic tori exhibit doubling. © *2005 Pleiades Publishing, Inc.*

Investigation into bifurcations of quasi-periodic oscillations and the transitions to chaos as a result of their breakage is an important direction of research in modern nonlinear dynamics. Details of the transition to chaos via multifrequency oscillations can be described using the classical mechanisms of Landau–Hopf [1, 2], Ruelle–Takens [3, 4], and Afraimovich–Shil'nikov [5]. The problem has been analyzed in application to a broad class of both real and model dynamical systems [6]. The regimes of quasi-periodic oscillations are most frequently described using discrete and differential systems with external periodic excitation (i.e., nonautonomous systems).

This study was aimed at finding the simplest autonomous differential system admitting solutions in the form of stable two-frequency oscillations and featuring the main bifurcation mechanisms of their breakage, including period-doubling bifurcations. Although the doubling of a two-dimensional (3D) torus was discovered many years ago [7–9], details of the bifurcation mechanisms of ergodic torus doubling are still incompletely clear. A 2D torus can be realized in a 3D autonomous dissipative system as demonstrated, for example, in [10]. However, realization of the torus-doubling bifurcation requires the system dimension to be increased to $N \geq 4$.

This Letter proposes the simplest autonomous dynamical system with $N = 4$, which features the regime of a stable 2D torus, admits bifurcations of torus doubling, and exhibits the transition to chaos via its breakage. The proposed model will be used to study some details of the bifurcation mechanism of ergodic 2D torus doubling.

The initial system represents the known oscillator model [11]:

$$\dot{x} = mx + y - xz - dx^3,$$
$$\dot{y} = -x, \qquad (1)$$
$$\dot{z} = -gz + g\Phi(x).$$

The first two equations in system (1) describe the van der Pol oscillator. At a finite g value, the system reveals an inertial character of action on the amplifying circuit of this oscillator, which is the main factor responsible for the appearance of chaotic oscillations. Indeed, the third equation in (1) describes an additional inertial (delayed) feedback chain, including the nonlinear transformation $\Phi(x)$, which can be set by a function of the type $e^x - 1$ or $I(x)x^2$, where $I(x) = 1$ ($x > 0$) and $I(x) = 0$ ($x \leq 0$).

In order to provide for the required properties of the system, let us change the inertial feedback circuit so as to increase the system dimension:

$$\dot{z} = \varphi,$$
$$\dot{\varphi} = -\gamma\varphi + \gamma\Phi(x) - gz. \qquad (2)$$

Here, γ is the damping parameter of the new filter and g is still the parameter characterizing the inertia. Equations (2) describe a dissipative circuit in the regime of induced oscillations:

$$\ddot{z} + \gamma\dot{z} + gz = \gamma\Phi(x). \qquad (3)$$

Analysis showed that, in order to provide for the regime of self-sustaining autonomous oscillations, it is sufficient to replace the control signal $z(t)$ in Eqs. (1)
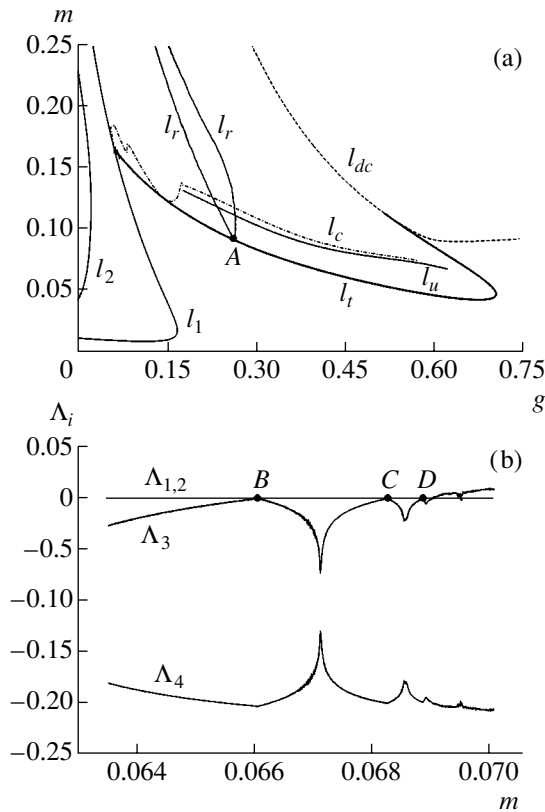
Fig. 1. (a) Bifurcation diagram of regimes of the proposed generator ($\gamma = 0.2$, $d = 0.001$) showing the curves of cycle period-doubling bifurcations (l_1, l_2), torus formation (l_t), torus breakage (l_u), and chaotic attractor breakage (l_c) and the boundaries of 1 : 4 resonance on the torus (l_r) (A is the point of codimension 2 corresponding to $\phi = 1 : 4$); (b) plots of the Lyapunov exponent versus m ($d = 0.001$, $\gamma = 0.2$, $g = 0.5$) in the region of parameters between curves l_t and l_u (B, C, D are the points of torus doubling bifurcations).

with its derivative $\dot{z}(t) = \varphi(t)$. Thus, the modified oscillator is described by the following equations:

$$
\begin{aligned}
\dot{x} &= mx + y - x\varphi - dx^3, \\
\dot{y} &= -x, \\
\dot{z} &= \varphi, \\
\dot{\varphi} &= -\gamma\varphi + \gamma\Phi(z) - gz.
\end{aligned}
\tag{4}
$$

Equations (4) represent a nonlinear dissipative dynamical system with $N = 4$, which is characterized by four parameters: m (excitation parameter), d (nonlinear dissipation parameter), γ (damping parameter), and g (inertial parameter).

The results of numerical experiments showed that system (4) features the regime of stable 2D torus, doubling bifurcations, and breakage of the torus with the transition to chaos. In addition, system (4) with small g

(i.e., a system close to (1)) exhibits bifurcations of cycle period doubling and the transition to chaos, thus showing a behavior analogous to that of system (1).

Figure 1a presents a bifurcation diagram of regimes for system (4) on the plane of control parameters m and g for fixed values of the two other parameters ($\gamma = 0.2$ and $d = 0.001$) and $\Phi(x) = I(x)x^2$. Here, line $m = 0$ shows the appearance (via a soft Andronov–Hopf bifurcation) of a stable limiting cycle T_0. Upon crossing the bifurcation curve l_1, this cycle exhibits a period-doubling bifurcation. The cycle appearing on curve l_1 exhibits a period-doubling bifurcation on curve l_2. The bifurcation curve l_t corresponds to the conditions under which the pair of complex-conjugate multiplicators of cycle T_0 attain the unit circle and a 2D torus ($m_{1,2} = e^{\pm j\phi}$) is softly born. Naturally, on the passage along curve l_t, the angle ϕ value runs through a set of rational values corresponding to resonances on the torus. As an example, Fig. 1a shows the region of resonance $\phi = 1:4$ bounded by curves l_r originating from point A with codimension 2. Crossing the curve l_u, situated above the torus formation curve l_t, corresponds to the transition to chaos via breakage of the quasi-periodic oscillations. Curve l_c corresponds to the crisis (breakage) of the chaotic attractor formed on curve l_u. Curve l_{dc} reflects the bifurcation of merging and vanishing of a pair of saddle cycles, and the region between curves l_t and l_u corresponds to 2D torus doubling bifurcations.

Now let us fix the parameters $g = 0.5$, $d = 0.001$, and $\gamma = 0.2$ and consider the evolution of the torus in the region of parameters between curves l_t and l_u. Figures 2a–2f show the projections of attractors onto the z–Y plane corresponding to the passage of points of the 2D torus doubling bifurcations. The doubling is clearly evidenced by the structure of the Poincaré section and by the analysis of time series and the corresponding power spectra. Here, the tore period doubling bifurcation corresponds to the bifurcation of modulation period doubling (or the cycle period doubling in the Poincaré map).

From the standpoint of the bifurcation theory, it is important to know whether the ergodic torus exhibits doubling or a resonance initially takes place on the torus, which is followed by doubling of the resonance cycle and the double torus formation. In order to answer this question, we have calculated the complete spectrum of Lyapunov exponents corresponding to the passage of bifurcation points (Fig. 1b). As can be seen from Fig. 1b, all three major Lyapunov exponents vanish ($\Lambda_1 = \Lambda_2 = \Lambda_3 = 0$) at the points of bifurcations (B, C, D). The bifurcation transition is characterized by the following change in the signs of the characteristic Lyapunov exponents:

$$
\begin{array}{ccc}
0, 0, -, - \Rightarrow & 0, 0, 0, - \Rightarrow & 0, 0, -, -. \\
\text{torus}_2 & \text{torus}_3 & \text{torus}_2
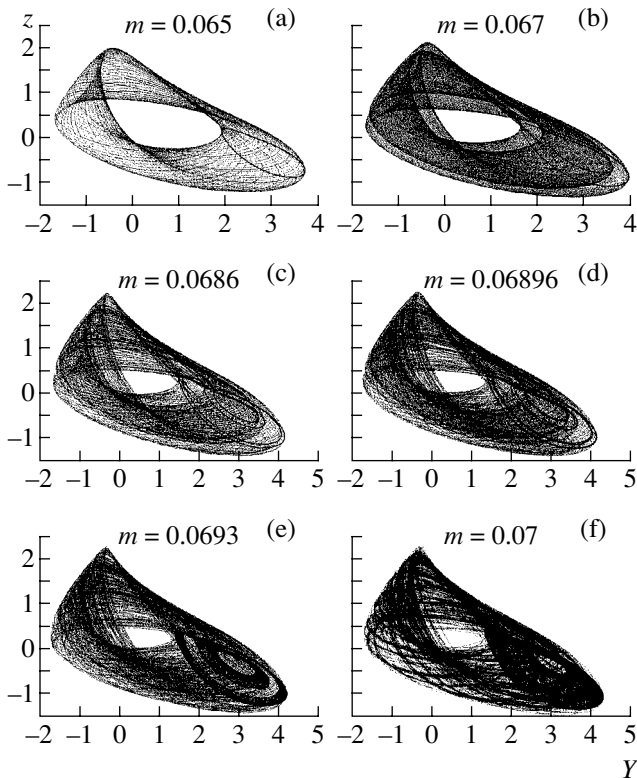\end{array}
$$

Fig. 2. Projections of the attractors of system (4) for $g = 0.125$ and the corresponding Poincaré sections on the z–Y plane for $d = 0.001$, $\gamma = 0.2$, $g = 0.5$ and various m values.

The results of calculations performed with a very small step in parameter m ($\Delta m = 3 \times 10^{-6}$) showed that the limiting cycle (with the spectrum of Lyapunov exponents 0, –, –, –) was not formed on the passage through the bifurcation point. At this point, we deal with a structurally unstable 3D torus, which gives rise to a stable double ergodic 2D torus. Thus, the above data confirm the results previously obtained in [12], where this conclusion was made for the first time. The period-doubling bifurcation takes place for the ergodic torus; no resonance cycles were observed in the numerical experiment.

Thus, the proposed dynamical system (4) actually makes possible the realization of a stable regime of ergodic two-frequency oscillations (2D torus regime) and exhibits modulation period-doubling (2D torus doubling) bifurcations. The autonomous system (4) offers the simplest model for investigations of the bifurcations of quasi-periodic oscillations with two independent frequencies. Detailed analysis of such regimes is beyond the scope of this study and will be performed in future work.

REFERENCES

1. L. D. Landau, Dokl. Akad. Nauk SSSR **44**, 339 (1944).
2. E. Hopf, Commun. Pure Appl. Math. **1**, 303 (1948).
3. D. Ruelle and F. Takens, in *Strange Attractors*, Ed. by Ya. G. Sinaǐ and L. P. Shilnikov (Mir, Moscow, 1981), pp. 117–151 [in Russian].
4. S. Newhouse, D. Ruelle, and F. Takens, Commun. Math. Phys. **64**, 35 (1978).
5. V. S. Afraimovich and L. P. Shilnikov, *Methods of the Qualitative Theory of Differential Equations* (Izd. Gorkovsk. Gos. Univ., Gorki, 1983), pp. 3–26 [in Russian].
6. V. S. Anishchenko, Zh. Tekh. Fiz. **56**, 225 (1986) [Sov. Phys. Tech. Phys. **31**, 137 (1986)].
7. V. S. Anishchenko, in *Proceedings of the 3rd All-Union Conference on Fluctuation Phenomena in Physical Systems, Vilnyus, 1982* (Izd. AN LitSSR, Vilnyus, 1983), pp. 24–26.
8. V. Franceschini, Physica D **6**, 285 (1983).
9. K. Kaneko, *Collapse of Tori and Genesis of Chaos in Dissipative Systems* (World Scientific, Singapore, 1986).
10. T. Matsumoto, L. O. Chua, and R. Tokunada, IEEE Trans. Circuits Syst. **34** (3) (1987).
11. V. S. Anishchenko, *Complex Oscillations in Simple Systems* (Nauka, Moscow, 1990) [in Russian].
12. V. S. Anishchenko, T. E. Letchford, and M. A. Safonova, Izv. Vyssh. Uchebn. Zaved., Radiofiz. **28**, 1112 (1985).

Translated by P. Pozdeev

Interaction between a Liquid and a Cylindrical Body Touching a Wall

V. L. Sennitskiĭ

Lavrentiev Institute of Hydrodynamics, Siberian Division, Russian Academy of Sciences, Novosibirsk, Russia
e-mail: igil@hydro.nsc.ru
Received April 12, 2005

Abstract—An exact solution is obtained for the problem of interaction between the ideal liquid homogeneously moving at infinity and streamlining a round cylinder touching a solid wall. © *2005 Pleiades Publishing, Inc.*

Determining a force acting upon a solid moving according to a preset law in a liquid medium is of independent basic interest and may favor finding new hydromechanical effects [1–4] (see also [5] and references therein).

This study is devoted to a description of the interaction between the ideal incompressible liquid homogeneously moving at infinity and streamlining an immobile hard round cylinder touching a solid wall. An exact solution of this problem is obtained, which shows that the cylinder exhibits repulsion from the wall.

We consider the ideal incompressible fluid, bounded by a hard flat wall, and a hard infinitely long round cylinder occurring in the liquid and touching the wall (see figure). The wall and the cylinder are in rest relative to the inertial Cartesian coordinate system XYZ. The wall surface coincides with the $Y = 0$ plane, and the cylinder touches this plane along the Z axis. The liquid occupies region Ω in the half-space $Y \geq 0$, is homogeneously moving at infinity with the velocity $\mathbf{V}_\infty = (V_\infty, 0, 0)$ along the X axis, and performs two-dimensional potential motion in the entire region Ω. The task is to describe the interaction between the liquid and the cylinder, that is, to determine the force $\mathbf{F}$ acting upon a part of the cylinder between two planes spaced by a unit distance in the flow (then, the force with which this part of the cylinder acts upon the liquid is $-\mathbf{F}$).

Let us introduce the polar coordinates (R, θ) in the plane $Z = 0$, which are related to the Cartesian coordinates (X, Y) as

$$X = -R\sin\theta, \quad Y = a + R\cos\theta; \qquad (1)$$

where a is the cylinder radius. In these coordinates, the force components F_x and F_y (the projections of $\mathbf{F}$ onto X and Y axes, respectively), the Cauchy–Lagrange integral I, the equation of continuity, and the boundary conditions at infinity and at the solid–liquid interface can be written as

$$F_x = a\int_{-\pi}^{\pi} P|_{R=a}\sin\theta\, d\theta; \qquad (2)$$

$$F_y = -a\int_{-\pi}^{\pi} P|_{R=a}\sin\theta\, d\theta; \qquad (3)$$

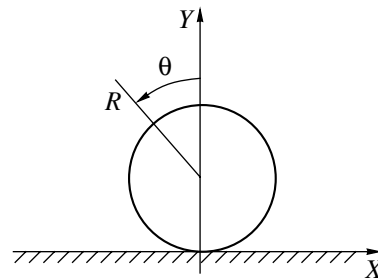$$\frac{\partial\Phi}{\partial t} + \frac{1}{2}(\nabla\Phi)^2 + \frac{P}{\rho} = I; \qquad (4)$$

$$\Delta\Phi = 0 \quad (a < R < \infty, \quad 0 < Y < \infty); \qquad (5)$$

$$\frac{\partial\Phi}{\partial Y} = 0 \text{ for } Y = 0,\ -\infty < X < 0 \text{ and } 0 < X < \infty; \qquad (6)$$

$$\frac{\partial\Phi}{\partial R} = 0 \text{ for } R = a, \quad -\pi < \theta < \pi; \qquad (7)$$

$$\Phi \sim V_\infty X \text{ for } R \longrightarrow \infty, \quad 0 \leq Y, \qquad (8)$$

where Φ is the velocity field potential in the liquid, ρ is the liquid density, P is the pressure in the liquid, and I is the function of time t.

Schematic diagram of the system under consideration.

It is convenient to introduce the coordinates (η, ξ) related to (X, Y) as

$$\eta = -2a\frac{X}{X^2 + Y^2}, \quad \xi = 2a\frac{Y}{X^2 + Y^2}. \quad (9)$$

The functions $\eta = \eta(X, Y)$ and $\xi = \xi(X, Y)$ defined by expressions (9) map the cross section of the region Ω with the plane $Z = 0$ into the band $-\infty \le \eta \le \infty$, $0 \le \xi \le 1$. Passing to the coordinates (η, ξ) in Eqs. (5)–(8), we eventually arrive at

$$\frac{\partial^2 \Phi}{\partial \eta^2} + \frac{\partial^2 \Phi}{\partial \xi^2} = 0 \; (-\infty < \eta < \infty, \; 0 < \xi < 1); \quad (10)$$

$$\frac{\partial \Phi}{\partial \xi} = 0 \text{ for } \xi = 0, \; -\infty < \eta < 0 \text{ and } 0 < \eta < \infty; \quad (11)$$

$$\frac{\partial \Phi}{\partial \xi} = 0 \text{ for } \xi = 1, \quad -\infty < \eta < \infty; \quad (12)$$

$$\Phi \sim -2aV_\infty \frac{\eta}{\eta^2 + \xi^2} \text{ for } \eta^2 + \xi^2 \longrightarrow 0, \quad 0 \le \xi. \quad (13)$$

Substituting in these relations

$$\Phi = \frac{\chi}{\cosh \pi \eta - \cos \pi \xi}, \quad (14)$$

we obtain a system of equations for χ:

$$\frac{\partial^2 \chi}{\partial \eta^2} + \frac{\partial^2 \chi}{\partial \xi^2} + \frac{\pi}{\cosh \pi \eta - \cos \pi \xi}$$

$$\times \left[-2\left(\sinh \pi \eta \frac{\partial \chi}{\partial \eta} + \sin \pi \xi \frac{\partial \chi}{\partial \xi} \right) \right. \quad (15)$$

$$\left. + \pi(\sinh \pi \eta + \cos \pi \xi)\chi \right] = 0$$

$$(-\infty < \eta < \infty, \quad 0 < \xi < 1);$$

$$\frac{\partial \chi}{\partial \xi} = 0 \text{ for } \xi = 0, \quad -\infty < \eta < 0 \text{ and } 0 < \eta < \infty; \quad (16)$$

$$\frac{\partial \chi}{\partial \xi} = 0 \text{ for } \xi = 1, \quad -\infty < \eta < \infty; \quad (17)$$

$$\frac{\chi}{\cosh \pi \eta - \cos \pi \xi} \sim -2aV_\infty \frac{\eta}{\eta^2 + \xi^2} \quad (18)$$

$$\text{for } \eta^2 + \xi^2 \longrightarrow 0, \quad 0 \le \xi.$$

The problem formulated by Eqs. (15)–(18) has the following solution:

$$\chi = -\pi a V_\infty \sinh \pi \eta. \quad (19)$$

Then, according to relations (14) and (19),

$$\Phi = -\pi a V_\infty \frac{\sinh \pi \eta}{\cosh \pi \eta - \cos \pi \xi}. \quad (20)$$

Using Eqs. (1)–(4), (9), and (20), we obtain

$$F_x = Aa^2\rho\frac{pV_\infty}{dt}, \quad F_y = Ba\rho V_\infty^2, \quad (21)$$

where

$$A = 2\pi \int_0^\pi \frac{\sinh[\pi \sin\theta/(1 + \cos\theta)]\sin\theta}{\cosh[\pi \sin\theta/(1 + \cos\theta)] + 1} d\theta; \quad (22)$$

$$B = \pi^4 \int_0^\pi \frac{\cos\theta}{\{\cosh[\pi \sin\theta/(1 + \cos\theta)] + 1\}^2(1 + \cos\theta)^2} d\theta.$$

Substituting into these expressions $\theta = \arccos\dfrac{\pi^2 - \varphi^2}{\pi^2 + \varphi^2}$ and taking into account the formula $\sum_{k=1}^\infty (-1)^k k^{-2} = -\pi^2/12$ (see [6]), one can readily show that $B = \dfrac{\pi}{9}(\pi^2 + 3)$ (numerical calculations yield $A \approx 10.34$ and $B \approx 4.49$).

Formulas (21) determine an exact solution to the problem of interaction between the liquid and the cylinder as formulated above. In particular, Eqs. (21) show that the cylinder exhibits repulsion from the wall, since the force **F** is directed toward the region Ω occupied by the liquid.

Let the liquid at infinity perform periodic oscillations with the period T. Using formulas (21) to determine the time-average force acting upon the cylinder, we obtain

$$\langle F_x \rangle = 0, \quad \langle F_y \rangle = Ba\rho\langle V_\infty^2 \rangle, \quad (23)$$

where $\langle \ldots \rangle = \dfrac{1}{T}\int_T^{t+T} \ldots dt$. Expressions (23) indicate, in particular, that the average force $\langle \mathbf{F} \rangle$ directed toward the region Ω is perpendicular to the solid wall. It should be noted that the time-average force acting upon a body (round cylinder or ball) occurring far from the wall is such that the body is attracted to the wall [1–3].

The obtained results can be used in the investigation of phenomena involving liquid flows along interfaces in

the presence of surface roughnesses and foreign particles.

Acknowledgments. The author is grateful to N.A. Galeva for her help in calculating integrals.

REFERENCES

1. V. L. Sennitskiĭ, Prikl. Mekh. Tekh. Fiz., No. 5, 19 (1985).

2. B. A. Lugovtsov and V. L. Sennitskiĭ, Dokl. Akad. Nauk SSSR **289**, 314 (1986) [Sov. Phys. Dokl. **31**, 530 (1986)].

3. V. L. Sennitskiĭ, Prikl. Mekh. Tekh. Fiz., No. 4, 125 (1999).

4. V. L. Sennitskiĭ, Prikl. Mekh. Tekh. Fiz., No. 1, 57 (2000).

5. O. S. Pyatigorskaya and V. L. Sennitskiĭ, Prikl. Mekh. Tekh. Fiz., No. 4, 102 (2004).

6. L. Euler, *Introduction to the Analysis of Infinite Quantities* (Fizmatgiz, Moscow, 1961), Vol. 1 [in Russian].

Translated by P. Pozdeev

Nonequilibrium Heteroepitaxy of Silicon Carbide on Silicon

S. A. Kukushkin[a,*], A. V. Osipov[a], S. K. Gordeev[b], and S. B. Korchagina[b]

[a] *Institute for Problems of Mechanical Engineering, Russian Academy of Sciences, St. Petersburg, 199178 Russia*
[b] *Central Materials Research Institute, St. Petersburg, Russia*
* e-mail: ksa@phase.ipme.ru
Received May 25, 2005

Abstract—A method of silicon carbide (SiC) deposition onto silicon via a nonequilibrium disilicon carbide (Si_2C) vapor phase is proposed, theoretically described, and experimentally verified. Estimates obtained using thermochemical calculations show that a sufficiently large number of SiC molecules, which are transported by mobile Si_2C species, are obtained using this method on the silicon surface. It is established that homogeneous epitaxial SiC layers can be grown on a Si(111) substrate surface. © *2005 Pleiades Publishing, Inc.*

The high mobility of free electrons, high electric strength in combination with a sufficiently large bandgap width, and excellent thermomechanical characteristics make silicon carbide (SiC) a highly promising material for various semiconductor devices [1]. However, the realization of this potential is hindered by the absence of a technology of high-quality heteroepitaxial SiC layers. For this reason, much effort has been devoted in recent years to the investigation of SiC heteroepitaxy on silicon, which is related to the advantageous combination of the properties of these materials and the existence of a highly developed silicon technology [1]. In addition, SiC epilayers can be used as buffers for the growth of gallium nitride and aluminum nitride films.

Silicon carbide layers are most frequently obtained using three methods: deposition via sublimation in vacuum, molecular beam epitaxy (MBE), and chemical vapor deposition (CVD) (see, e.g., [1–6]). Each of these methods has certain advantages and disadvantages, but no SiC layers of the required quality have been obtained so far using either of these techniques. This is related primarily to the extremely low density of saturated vapor of both carbon and its carbide at a temperature of and below SiC melting. For this reason, the evaporation material exhibits immediate condensation and has a low mobility on the substrate surface, which leads to poor epitaxial growth [7]. In order to improve the epitaxy, it is necessary to increase the mobility of deposited particles from which the film is growing [7]. For the epitaxy of SiC, this implies that the film has to be grown under conditions of a high density of saturated vapor over the intrinsic crystal surface and a low energy of SiC binding to silicon. As is known, silicon carbide exhibits decomposition on sublimation with the formation of compounds such as SiC, Si, Si_2C, and SiC_2 in the vapor phase. However, the equilibrium vapor densities of Si and SiC in the gas phase over solid SiC at temperatures below 1400°C are extremely low.

Even the vapor densities of two other compounds, Si_2C and SiC_2, in equilibrium with solid SiC at $T = 1400$°C (albeit five orders of magnitude higher than that for SiC) are still insufficient to provide for any significant growth of SiC on the surface of silicon.

These circumstances lead to the idea of depositing silicon carbide under nonequilibrium conditions, whereby the density of vapor delivering the material possessing a sufficiently high mobility on silicon is many orders of magnitude higher than the equilibrium vapor density over solid SiC at a given substrate temperature. Among all compounds formed between silicon and carbon, the only volatile substance occurring in equilibrium with the solid phase at $T < 1400$°C is silicon. Thus, only silicon is capable of shifting the chemical reaction toward a regime in which the concentration of the reaction products would be higher than that under equilibrium conditions. In the presence of excess Si in the gas phase, the reaction of SiC dissociation into gaseous silicon and carbon, as well as the reaction of SiC_2 formation, will be suppressed according to Le Chatelier's principle. In particular, only gaseous Si_2C will be formed in the reaction between gaseous Si and solid carbon.

Thus, gaseous Si will significantly increase the concentration of only one gaseous reaction product:

$$2Si_{(v)} + C_{(s)} \rightleftharpoons Si_2C_{(v)} + \Delta Q, \tag{1}$$
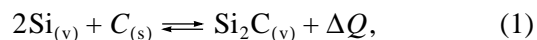
where ΔQ is the heat of formation of Si_2C. An increase in the concentration [Si] of the gaseous reagent (e.g., via evaporation from the substrate) will shift reaction (1) toward the right-hand side thus increasing the gaseous product concentration $[Si_2C]$. According to equation (1), the concentration $[Si_2C]$ is proportional to the square of the silicon concentration [Si] in the gas phase: $[Si_2C] = K[Si]^2$, where K is the equilibrium constant of reaction (1). This reaction is highly effective as a means of delivering material for the growth of SiC, because the product

(Si$_2$C) formation is accompanied by the evolution of a considerable amount of heat. The results of thermochemical calculations show that, for example, $\Delta Q \approx$ 360 kJ/mol at $T = 1250°C$. For comparison, note that the heat of formation of Si$_2$C via the reaction Si$_{(v)}$ + SiC$_{(s)}$ $\Longleftrightarrow$ Si$_2$C$_{(v)}$ + ΔQ is negative and amounts to $\Delta Q = -160$ kJ/mol at $T = 1250°C$. As a result, the product concentration [Si$_2$C] is about seven orders of magnitude lower than that in reaction (1) for the gaseous silicon concentration [Si] in equilibrium with solid Si at a given temperature. By the same token, the concentration of another product, SiC$_2$, formed in the reaction Si$_{(v)}$ + 2C$_{(s)}$ $\Longleftrightarrow$ SiC$_{2(v)}$ – 167 kJ/mol is about four orders of magnitude lower than the concentration of Si$_2$C formed in reaction (1).

Let us evaluate the nonequilibrium flux of Si$_2$C from the gas phase to the substrate. The pressure p of Si$_2$C vapor formed as a result of reaction (1) where silicon in the gas phase is in equilibrium with solid silicon (i.e., its pressure is equal to the equilibrium value p_e) is

$$p = K \frac{p_e^2}{p_0}, \qquad (2)$$

where $p_0 = 1$ bar is the base pressure in the ground state adopted in thermochemical calculations. The equilibrium constant of reaction (1) is

$$K = \exp \frac{T\Delta S - \Delta H}{RT}, \qquad (3)$$

where R is the universal gas constant and ΔS and ΔH are the changes in the system entropy and enthalpy upon the reaction, respectively. Calculation of the ΔS and ΔH values using reference data [8] for $T = 1250°C$ yields $T\Delta S = -153$ kJ /mol, $\Delta H = -360$ kJ/mol, and $K = 1.3 \times 10^7$. For these values, formula (2) yields an estimate for the Si$_2$C pressure: $p = 15$ Pa. Since solid Si$_2$C does not exist and, hence, cannot condense from the gas phase, the energy of Si$_2$C binding to silicon is much lower than that for C or SiC. Therefore, Si$_2$C molecules must possess sufficiently high mobility for a good epitaxial growth.

The flux of Si$_2$C molecules to a substrate can reach a level of

$$J = \frac{p}{\sqrt{2\pi m k_B T}}, \qquad (4)$$

where m is the molecular weight of Si$_2$C and k_B is the Boltzmann constant. For $p = 15$ Pa and $T = 1250°C$, formula (4) yields $J = 5 \times 10^{20}$ cm^{-2} s^{-1}. This is a sufficiently large flux of molecules that provides, even at a rather short lifetime in the adsorbed state, the presence of a relatively dense Si$_2$C adsorbate featuring the decomposition reaction

$$Si_2C_{(v)} \Longleftrightarrow SiC_{(v)} + Si_{(v)}. \qquad (5)$$
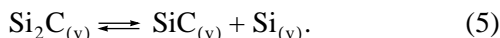
Gaseous SiC formed in this reaction immediately attaches to the solid phase or decomposes because its equilibrium vapor density is extremely low. The resulting silicon also either incorporates into the substrate or evaporates. It is important to note that both solid Si and SiC serve as active catalysts in the decomposition reaction (5).

In order to realize the proposed mechanism of SiC deposition, it is necessary to provide for the depot of silicon involved in reaction (1). In this study, we used the following patented method [9, 10]. A three-inch Si(111) substrate plate is placed at a distance of 1–10 μm from a parallel, ground, and mirror-polished surface of a 3-mm-thick porous carbon plate prepared as described in [11]. This system is placed into a vacuum furnace and treated for 5–60 min at 1100–1400°C and a residual air pressure of ~10 Pa. During this treatment, silicon initially evaporates from the substrate surface and penetrates into the porous carbon "sponge" to an average depth of about 0.2 mm. Then, silicon vapor occurring in equilibrium with solid silicon both in the substrate and in porous carbon enters into the chemical reaction with carbon according to equation (1). This reaction leads to the formation of Si$_2$C molecules in the gas phase, which adsorb on the silicon substrate. These high-mobility adsorbed Si$_2$C species exhibit rapid decomposition with the formation of gaseous SiC, which results in the instantaneous nucleation and growth of a solid SiC phase on the substrate surface. According to the general theory of nucleation [7], this process decreases supersaturation and renders it nonequilibrium. The SiC nuclei grow and merge together, thus forming a continuous film on the substrate surface, which takes about 5–10 min at a substrate temperature of 1250°C. At a higher temperature, the time necessary for the formation of a continuous coating decreases, while at a lower temperature this time increases. Once such a continuous film is formed, the evaporation of Si from the substrate surface ceases and the growth proceeds only at the expense of silicon accumulated in porous carbon. In some time, this source is exhausted and the process of silicon carbide film growth is terminated.

Figure 1 shows a micrograph of SiC nuclei on Si(111) formed within 5 min of heating at 1250°C. The results of X-ray diffraction and electron diffraction investigation showed that SiC layers grown on Si(111) substrates using the method described above are epitaxial and homogeneous over the entire substrate surface. Figure 2 presents the typical X-ray diffractogram and the pattern of electron diffraction for a SiC layer grown for 20 min at 1250°C.

Investigations of the SiC film thickness as a function of the temperature of epitaxial growth in the interval from 1100 to 1400°C showed that this temperature dependence is well described by the Arrhenius curve with an activation energy of ~2.5 eV (for approximately ~50-nm-thick film grown at 1250°C). This activation
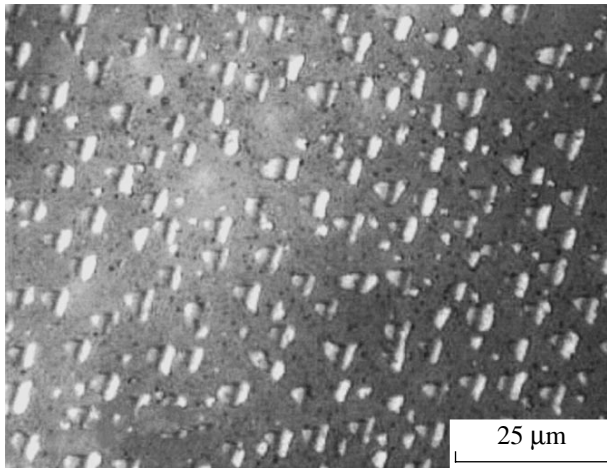
Fig. 1. Microphotograph of SiC nuclei formed on Si(111) for 5 min at 1250°C.
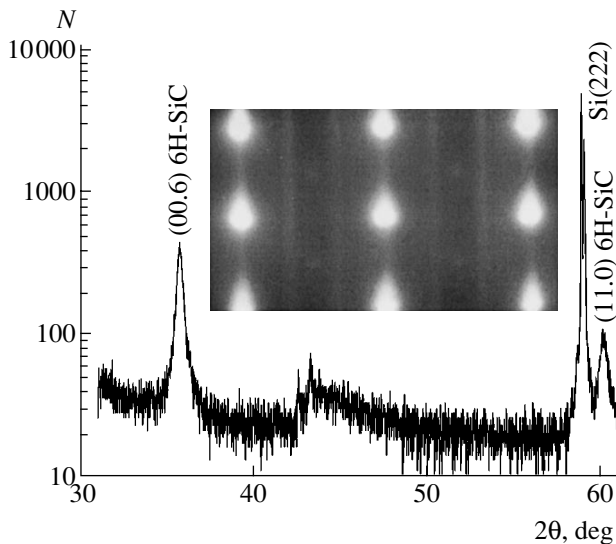

Fig. 2. The typical X-ray diffractogram and an electron diffraction pattern (inset) of a SiC film grown on Si(111) for 20 min at 1250°C. The X-ray diffraction measurements were performed on a Geigerflex D/max-RC diffractometer (Rigaku, Japan) using CuK_α radiation ($\lambda = 1.54056$ Å; angular step, 0.01°; detection time, 1 s). The rocking curves were measured in the two-crystal diffraction scheme (ω scan mode). The electron diffraction measurements were performed in the reflection mode on an EMR-100 electronograph operating at an accelerating voltage of 75 keV.

energy is close to the activation energy of desorption (~2.6 eV) from silicon surface, which is indirect evidence for the proposed mechanism of epitaxial growth. The maximum surface density of SiC islands as a function of the temperature is also well described by the Arrhenius curve, which is characterized by an activation energy of ~1.5 eV.

Thus, using the proposed method of silicon carbide deposition on silicon via a nonequilibrium Si_2C vapor phase, it is possible to obtain homogeneous epitaxial SiC layers on Si(111) substrates. The main advantage of this method is that it employs nonequilibrium Si_2C gas-phase species possessing high mobility and a sufficiently large density. Homogeneous evaporation of silicon from the substrate surface provides for a highly uniform flux of Si_2C species and, hence, for the homogenous growth of SiC.

REFERENCES

1. *Silicon Carbide. A Review of Fundamental Questions and Applications to Current Device Technology*, Ed. by W. J. Choyke, H. M. Matsunami, and G. Pensl (Akademie, Berlin, 1998), Vols. 1–2.

2. A. Fissel, Phys. Rep. **379**, 149 (2003).

3. Yu. V. Trushin, E. E. Zhurkin, K. L. Safonov, *et al.*, Pis'ma Zh. Tekh. Fiz. **30** (15), 48 (2004) [Tech. Phys. Lett. **30**, 641 (2004)].

4. A. N. Andreev, N. Yu. Smirnova, A. S. Tregugova, *et al.*, Fiz. Tekh. Poluprovodn. (St. Petersburg) **31**, 285 (1997) [Semiconductors **31**, 232 (1997)].

5. V. V. Zelenin, M. L. Korogodskiĭ, and A. A. Lebedev, Fiz. Tekh. Poluprovodn. (St. Petersburg) **35**, 1172 (2001) [Semiconductors **35**, 1120 (2001)].

6. E. V. Bogdanova, A. A. Volkova, A. E. Cherenkova, *et al.*, Fiz. Tekh. Poluprovodn. (St. Petersburg) **39**, 762 (2005) [Semiconductors **39**, 730 (2005)].

7. S. A. Kukushkin and A. V. Osipov, Usp. Fiz. Nauk **168**, 1084 (1998) [Phys. Usp. **41**, 983 (1998)].

8. *A Handbook of Thermodynamic Properties of Individual Substances*, Ed. by V. P. Glushko (Nauka, Moscow, 1979), Vols. 1–2 [in Russian]; *Thermodynamic Properties of Individual Substances*, Ed. by L. V. Gurvich, I. V. Veyts, and C. B. Alcock (Hemisphere, New York, 1989–1994).

9. S. K. Gordeev, S. B. Korchagina, S. A. Kukushkin, and A. V. Osipov, RF Patent Appl. No. 2005103321 (February 10, 2005).

10. S. K. Gordeev, S. B. Korchagina, S. A. Kukushkin, and A. V. Osipov, RF Patent Appl. No. 2005103322 (February 10, 2005).

11. S. K. Gordeev, in *Nanostructured Carbon for Advanced Applications*, Ed. by G. Benedek, P. Milani, and V. G. Ralchenko (Kluwer, Dordrecht, 2001), pp. 71–88.

Translated by P. Pozdeev

An Exact Particular Solution
for an Equilibrium Uncharged Conducting Jet Configuration
in a Transverse Electric Field

N. M. Zubarev* and O. V. Zubareva

Institute of Electrophysics, Ural Division, Russian Academy of Sciences, Yekaterinburg, 620219 Russia
* e-mail: nick@ami.uran.ru
Received May 18, 2005

Abstract—The problem concerning the equilibrium configurations of the surface of an uncharged conducting jet in a transverse electric field has been considered. It is established that this electrostatic problem is analogous to the problem of the potential streamlining of a two-dimensional gas bubble by the ideal liquid, for which effective analytical solution methods are available. Using this analogy, an exact solution for the jet shape has been constructed and studied with respect to stability in the particular case in which the difference of pressures inside and outside the jet is zero. This solution is characterized by a significant degree of deformation, whereby the aspect ratio of the jet cross section amounts to 23/4. © 2005 Pleiades Publishing, Inc.

In the absence of an external electric field, the only stable equilibrium jet configuration is a round cylinder. Let us consider a jet of conducting fluid in an electric field of strength E, which is oriented perpendicularly to the jet axis. Since the applied field does not penetrate inside the conducting fluid, it induces charging of the jet surface. The force with which the electric field acts on the surface charge will produce azimuthal deformation of the jet surface and stretch it along the field. Compensation of the electrostatic forces by the surface tension will lead to a new equilibrium configuration of the jet surface.

As is known, capillary effects (in the absence of electric fields) lead to the development of the so-called Rayleigh instability of a round cylindrical jet, which is manifested by the growth of small longitudinal perturbations with a characteristic wavelength exceeding the circumference length [1]. In order to analyze the stability of a jet occurring in an electric field, it is necessary first to find a solution of the problem for the unperturbed state. This solution is no longer represented by a round cylinder and, hence, we have to study how the jet cross section is deformed under the action of electrostatic forces.

In this Letter, we describe a particular solution for the special case in which the difference P of pressures inside and outside the jet is zero and consider the conditions of existence of stable solutions for arbitrary P values. Previously, a broad class of exact solutions was found [2, 3] for an analogous problem concerning the configuration of a charged jet of conducting fluid.

Let us assume that the jet cross section remains constant and the fluid occurs in rest in the frame of reference moving with the jet. Then, the electric field potential φ in the jet cross section plane $\{x, y\}$ is described by the two-dimensional Laplace equation

$$\varphi_{xx} + \varphi_{yy} = 0.$$

This equation has to be solved together with the equipotential condition $\varphi = 0$ on the conductor surface. Another boundary condition corresponds to the homogeneity of the electric field at infinity:

$$\varphi \longrightarrow -Ey, \quad x^2 + y^2 \longrightarrow \infty.$$

The equilibrium relief of the surface of a conducting fluid is determined by the condition of balance for the forces acting on this charged surface:

$$(8\pi)^{-1}(\nabla\varphi)^2_{\varphi=0} + \alpha K + P = 0, \tag{1}$$

where the first term describes the electrostatic pressure at the liquid boundary and the second term describes the surface pressure (α is the surface tension coefficient and K is the local curvature of the surface).

A comparison of Eq. (1) with equations describing the shape of a gas bubble moving in the ideal liquid [4] shows that these expressions coincide to within the following substitution:

$$E \longrightarrow -\sqrt{4\pi\rho}V, \quad \varphi \longrightarrow \sqrt{4\pi\rho}\psi,$$

where V is the velocity of liquid streamlining the bubble, ρ is the density of this liquid, and ψ is the current function. Rewritten in terms of these variables, Eq. (1) becomes the stationary Bernoulli equation for the bubble surface, in which the constant P describes the difference between the pressure inside the bubble and the energy density in the liquid at infinity.

An exact solution for the bubble shape in the particular case of $P = 0$ was obtained by McLeod [4], and the

jet shape corresponding to this partial solution is described by the following expressions:

$$x = \frac{8\pi\alpha}{9E^2}\left(\cos s - \frac{1}{9}\cos 3s\right), \qquad (2)$$

$$y = \frac{8\pi\alpha}{9E^2}\left(5\sin s - \frac{1}{9}\sin 3s\right), \qquad (3)$$

where s is a parameter varying within the interval $0 < s \le 2\pi$. As can be seen from these formulas, the electric field produces a strong deformation of the jet, whereby the ratio of characteristic dimensions of the jet cross section (aspect ratio) is 23/4.

Now we will show that the above solution is unstable with respect to azimuthal deformations of the jet surface. Let us construct a family of "perturbed" solutions for the equilibrium jet configurations corresponding to small nonzero differences P of the pressures inside and outside the jet. Restricting our consideration to the terms of the zeroth and first order of smallness with respect to the small dimensionless parameter $p = 8\pi P/(81E^2)$, we obtain the following expressions for the shape of the jet cross section:

$$x = \frac{8\pi\alpha}{9E^2}\left((1 + 113p)\cos s - \frac{1 - 133p}{9}\cos 3s \right.$$
$$\left. + \frac{2p}{5}\cos 5s\right), \qquad (4)$$

$$y = \frac{8\pi\alpha}{9E^2}\left((5 + 119p)\sin s + \frac{1 - 133p}{9}\sin 3s \right.$$
$$\left. - \frac{2p}{5}\sin 5s\right). \qquad (5)$$

It should be noted that similar expansions for two-dimensional bubbles were considered by Shankar [5].

The degree of deformation of the jet surface is conveniently characterized in terms of the aspect ratio defined as the ratio of characteristic cross section dimensions along the y and x axes:

$$\frac{y_{max}}{x_{max}} \approx \frac{23}{4} - \frac{9801}{10}p. \qquad (6)$$

This formula shows that an increase in the p value leads to contraction, while a decrease in p results in an extension of the jet cross section along the field.

The jet cross section area for the perturbed solution given by formulas (4) and (5) is

$$S \approx \frac{2^8\pi^3\alpha^2}{3^6 E^4}(67 + 6154p). \qquad (7)$$

As can be seen from this relation, an increase (decrease) in the electric field strength for a constant S leads to a corresponding increase (decrease) in p and, according to (6), to contraction (extension) of the jet cross section in the field direction (e.g., along the y axis). This result immediately implies that the solution given by Eqs. (2) and (3) is unstable with respect to small surface perturbations. In the domain of stability, an increase in the electric field strength (and, hence, in the force deforming the jet) must lead to an extension of the jet cross section. This means that stable configurations correspond to deformations leading to the aspect ratios significantly below 23/4.

The monotonic character of the dependence of E on p determined by relation (7) must be violated at rather large p values, that is, outside the domain of applicability of expressions (4) and (5). Indeed, in the absence of the field ($E = 0$), the jet will have a round cross section. The force balance condition (1) shows that the pressure difference for such a round jet is finite: $P = \alpha\sqrt{\pi/S}$. In this case, $E \longrightarrow 0$ for $p \longrightarrow \infty$. As a result, the E versus p curve must exhibit an extremum E_{max}, which coincides in the order of magnitude with the field corresponding to the exact solution given by Eqs. (2) and (3):

$$E_{max}^4 \propto \alpha^2 S^{-1}.$$

The existence of equilibrium jet configurations is principally impossible for the field strengths above this threshold. An analogous criterion is known for the uncharged drop of a conducting liquid occurring in an electric field [6, 7].

REFERENCES

1. Lord Rayleigh, Proc. London Math. Soc. **10**, 4 (1878).
2. N. M. Zubarev and O. V. Zubareva, Pis'ma Zh. Tekh. Fiz. **30** (1), 51 (2004) [Tech. Phys. Lett. **30**, 23 (2004)].
3. N. M. Zubarev, Phys. Rev. E **71**, 016307 (2005).
4. E. B. McLeod, Arch. Ration. Mech. Anal. **4**, 557 (1955).
5. P. N. Shankar, J. Fluid Mech. **244**, 187 (1992).
6. G. Taylor, Proc. R. Soc. London, Ser. A **280**, 383 (1964).
7. A. I. Grigor'ev and S. O. Shiryaeva, Zh. Tekh. Fiz. **57**, 1706 (1987) [Sov. Phys. Tech. Phys. **32**, 1020 (1987)].

Translated by P. Pozdeev

Multilayer AlN/AlGaN/GaN/AlGaN Heterostructures for High-Power Field-Effect Transistors Grown by Ammonia MBE

A. N. Alekseev*, S. B. Aleksandrov, A. É. Byrnaz, L. É. Velikovskiĭ, I. É. Velikovskiĭ, D. M. Krasovitskiĭ, M. V. Pavlenko, S. I. Petrov, Yu. V. Pogorel'skiĭ, I. A. Sokolov, M. A. Sokolov, M. V. Stepanov, A. G. Tkachenko, A. P. Shkurko, and V. P. Chalyĭ

Svetlana–ROST Corporation, St. Petersburg, Russia
* e-mail: support@semiteq.ru
Received May 16, 2005

Abstract—The results of the optimization of the ammonia MBE technology of AlN/AlGaN/GaN/AlGaN heterostructures for high-power microwave field-effect transistors (FETs) are presented. The creation of technological systems of the EPN type for the deposition of group III nitrides by ammonia MBE, in combination with the development of optimum growth and postgrowth processes, make it possible to obtain AlN/AlGaN/GaN/AlGaN based heterostructures for high-power microwave FETs with the output static characteristics on the world best level. One of the main fields of application of the semiconductor heterostructures based on group III nitrides is the technology of high electron mobility transistors (HEMTs). Most investigations in this field have been devoted to the classical GaN/AlGaN structures with a single heterojunction. An alternative approach based on the use of double heterostructures with improved two-dimensional electron gas (2DEG) confinement offers a number of advantages, but such structures are usually characterized by a lower carrier mobility as compared to that in the single-junction structures. We succeeded in optimizing the double heterostructure parameters and growth conditions so as to obtain conducting channels with a 2DEG carrier mobility of 1450, 1350, and 1000 $cm^2/(V \cdot s)$ and a sheet electron density of 1.3×10^{13}, 1.6×10^{13}, and 2.0×10^{13} cm^{-2}, respectively. Experimental HEMTs with 1-μm-long gates based on the obtained multilayer heterostructure with a doped upper barrier layer exhibit stable current–voltage characteristics with maximum saturation current densities of about 1 A/mm and a transconductance of up to 180 mS/mm. © 2005 Pleiades Publishing, Inc.

Introduction. With respect to the combination of working parameters, field-effect transistors (FETs) based on GaN/AlGaN heterostructures occupy an exceptional position in the series of analogous microwave devices based on traditional semiconductors. In particular, GaN based high electron mobility transistors (HEMTs) have recently been created that are capable of operating at a power density of up to 32 W/mm in a discrete form [1] and at a total power in excess of 150 W in the form of integrated amplifiers [2]. However, most of these devices are based on the classical GaN/AlGaN structures with a single heterojunction featuring a two-dimensional electron gas (2DEG) with a sheet electron density on the order of 10^{13} cm^{-2}. The mobility of electrons in 2DEG significantly depends on the degree of perfection of the heterostructure and may reach about 2000 $cm^2/(V \cdot s)$ at 300 K [3], although most typical devices are characterized by room-temperature mobilities within 1000–1500 $cm^2/(V \cdot s)$. FETs based on such single-junction heterostructures usually exhibit a saturation current density of 0.6–1.2 A/mm and a transconductance in the interval from 120 to 200 mS/mm. A disadvantage of the classical GaN/AlGaN structures is the limited potential for increasing the properties of related

devices, which practically reduces to thorough optimization of the growth technology and the postgrowth treatment conditions.

An alternative approach is related to the use of double heterostructures (DHSs) with improved 2DEG confinement, which are widely employed in the traditional semiconductor systems [4] and offer a number of advantages, including the possibility of two-sided doping of the conducting channels. In application to group III nitrides, the use of this approach in the form of AlGaN layers in the buffer part of heterostructures prevents the upper barrier AlGaN layers from cracking (which frequently takes place in the classical structures under the action of tensile stresses [5]) and ensures excellent insulating properties of the buffer layer (which are difficult to provide in the classical heterostructures).

Although the number of communications concerning the growth of DHSs with improved 2DEG confinement in the Al–Ga–N system is very restricted, this approach has already been implemented at the device level. In particular, a DHS doped on both sides from a 250-Å-thick GaN channel obtained by Maeda *et al.* [6] was characterized by sheet electron densities up to 3×10^{13} cm^{-2} at a 2DEG carrier mobility of ~ 800 $cm^2/(V \cdot s)$.

HEMTs with 1.5-μm-long gates based on these DHSs exhibited a maximum saturation current density of 1.2 A/mm and a transconductance of 200 mS/mm. Chen *et al.* [7] showed that, by adjusting the AlGaN layer thicknesses and compositions in a DHS with 200-Å-thick GaN channel, it is possible to increase the 2DEG mobility to 1150 cm^2/(V s) at a sheet carrier density of ~1.1×10^{-13} cm^{-2}. The related transistors with 1-μm-long gates exhibited saturation current densities within 0.6–0.8 A/mm, which is comparable with the analogous values for the classical HEMTs. Previously, we also reported on the fabrication of a test series of FETs based on DHSs of the AlGaN/GaN/AlGaN type with modulation-doped upper barrier layer. In the static test regime, the obtained structures were characterized by saturation current densities up to 0.6 A/mm at a transconductance of up to 100 mS/mm and could operate in the small microwave signal regime at 8.15 GHz. Test devices based on the otherwise analogous undoped DHSs exhibited maximum saturation current densities of about 0.35 A/mm [9].

This Letter presents the results of the optimization of the design and technology of multilayer heterostructures based on Al$_x$Ga$_{1-x}$N compounds, with either undoped or modulation-doped upper barrier layers, which allowed us to obtain a 2DEG mobility of no less than 1300 cm^2/(V s) at a sheet carrier density of no less than 1.6×10^{13} cm^{-2}. The test HEMTs with 1-μm-long gates, based on the DHSs with a carrier mobility of about 1000 cm^2/(V s) and a sheet carrier density of 1.3×10^{13} cm^{-2}, exhibited a maximum saturation current density of about 1.0 A/mm and a transconductance of 180 mS/mm. These characteristics are comparable with the values reported for the modern classical single-junction heterostructures and related devices.

Experimental. Multilayer AlN/AlGaN/GaN/AlGaN heterostructures on (0001)-oriented sapphire substrates were grown using EPN type setups specially designed for the molecular beam epitaxy (MBE) of group III nitrides with ammonia as the source of active nitrogen. These technological systems are capable, in particular, of maintaining the substrate temperature at the level of 1100°C, which has proved to be a significant condition for the growth of high-quality Al$_x$Ga$_{1-x}$N layers with $x > 0.5$. The typical deposition rates were within 0.5–1.0 μm/h. The *in situ* monitoring of the growth temperature and the growth rate was provided by a universal device combining a pyrometer and a He–Ne laser interferometer. The state of the growth surface was studied by means of reflection high-energy electron diffraction (RHEED).

Prior to DHS growth, the sapphire substrates were degreased by standard methods, annealed for 1 h at 1100°C in vacuum, and nitrided for 10 min at 850°C in a flow of ammonia. The main distinction between our heterostructures [10] and the most widely used classical HEMT configuration is the presence of a relatively

thick Al$_x$Ga$_{1-x}$N ($0.3 < x < 1.0$) buffer with a total thickness of 0.8 μm, which ensures high (above 200 V) breakdown voltages of the device insulation [8, 9]. This layer is followed by a 2500-Å-thick undoped GaN layer covered by an undoped or Si-modulation-doped Al$_x$Ga$_{1-x}$N ($0.25 < x < 0.35$) layer with a total thickness of 250 Å. In the structures with doped upper barriers, we used a scheme with spacer, doped, and barrier AlGaN sublayers (30, 100, and 120 Å thick, respectively).

The properties of separate layers and multilayer heterostructures were studied using Hall effect measurements, atomic force microscopy (AFM), and X-ray diffraction (XRD). Some of the heterostructures represented test modules with dimensions 6×6 mm, which contained regions for determining the properties of carriers (Hall effect measurements), the electrical parameters of ohmic contacts (long line technique), and the breakdown voltage of the device insulation (buffer layer), as well as the test FETs with a source–drain distance of 4 μm and a 1-μm-long gate for the primary evaluation of current–voltage characteristics of the two-dimensional conducting channel. The electric insulation between elements of the mesa structure was provided by reactive ion etching in SiCl$_4$ plasma through a photoresist mask. The ohmic contacts consisting of Ti/Al/Ni/Au layers were fused by rapid (40 s) thermal annealing at 820°C. The 1-μm long gates were formed by means of explosive photolithography using Ni/Au composite metallization.

Results and discussion. The most difficult problems encountered in the optimization of multilayer heterostructures in the Al$_x$Ga$_{1-x}$N/GaN system are related to the growth of GaN, since this material is always strongly stressed being surrounded by relatively thick Al$_x$Ga$_{1-x}$N layers with a high Al content. The transport properties of carriers in the 2DEG are determined by the perfection of the GaN layer and by the quality of its boundaries with the AlGaN barrier layer.

The MBE-grown GaN layers typically possess a developed mosaic structure with a pronounced surface roughness, which usually increases with the layer thickness [11]. The density of dislocations of such GaN layers is also higher (on the average, by one to one and a half order of magnitude) than the analogous parameter of layers grown by metalorganic vapor phase epitaxy (MOVPE). The most probable factor responsible for these features is the relatively low surface mobility of atoms at a typical MBE growth temperature, which is insufficient for the effective coalescence of nucleated blocks. In particular, it was established that the character of the surface morphology of MBE-grown GaN layers exhibited a significant change in the course of their subsequent postgrowth annealing under the conditions characteristic of MOVPE (substrate temperature, 1000°C; ammonia pressure, 100 Torr). It should also be noted that competitive optoelectronic devices, whose
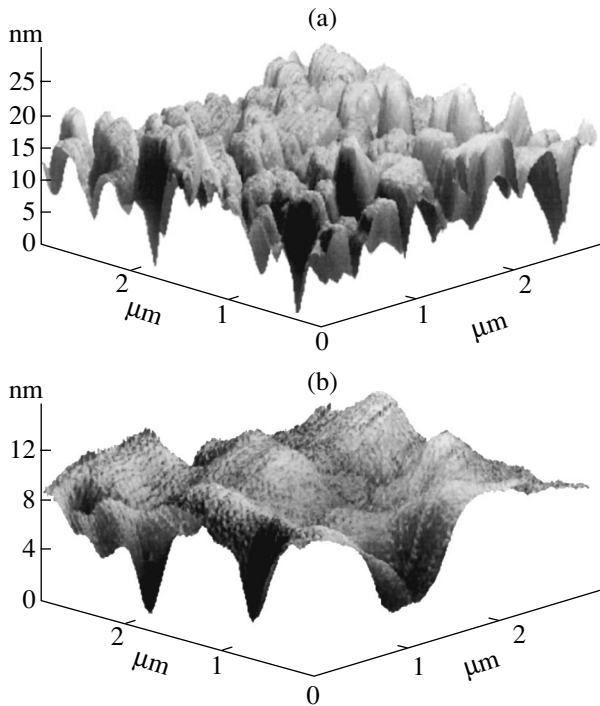
Fig. 1. AFM images of a 3×3 μm surface area scanned in (a) AlGaN/GaN/AlGaN (rms roughness, 34 Å) and (b) AlN/AlGaN/GaN/AlGaN (rms roughness, 17 Å) heterostructures.
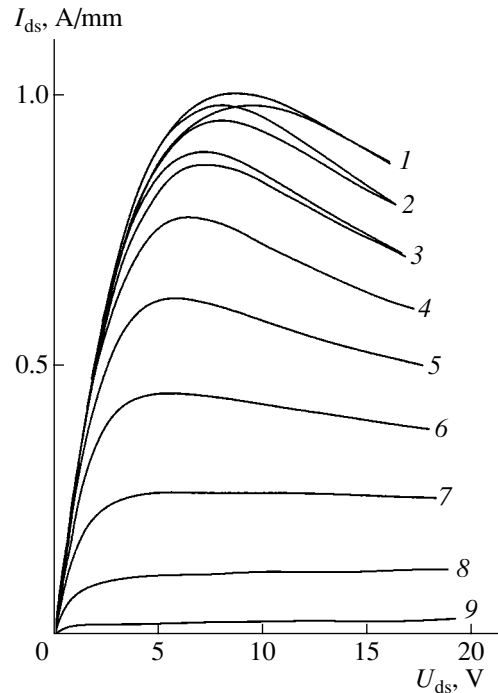

Fig. 2. Static current–voltage characteristics of a test field-effect transistor based on an AlN/AlGaN/GaN/AlGaN heterostructure measured at a gate voltage of $U_g = 1$ (*1*), 0 (*2*), –1 (*3*), –2 (*4*), –3 (*5*), –4 (*6*), –5 (*7*), –6 (*8*), and –7 V (*9*).

efficiency also depends on the density of dislocations in nitride based materials, can be obtained by MBE only on the commercially available quasi-GaN substrates (templates) manufactured by MOVPE [12–14]. On the other hand, it has sometimes been pointed out that the properties of device heterostructures are improved in the case of AlN templates [15].

Taking into account all these circumstances, we paid special attention to the initial stages of MBE growth of the nitride based heterostructures. In contrast to the case of the traditional relatively thin (~20 nm) nucleation layers widely used all over the world for the initiation of growth on sapphire substrates, we have used relatively thick (in excess of 100 nm) AlN buffer layers grown at unusually high (for MBE) substrate temperatures above 1000°C. This approach ensured the sufficiently high surface mobility of atoms that is necessary for the coalescence of nuclei without the risk of material decomposition (because the thermal stability of AlN is much higher than that of GaN). In addition, the use of relatively thick AlN layers is advantageous for the subsequent growth of $Al_xGa_{1-x}N$ layers with a high Al content. The result of our investigations showed that the optimum growth conditions correspond to a substrate temperature of 1070°C, an ammonia flow rate of 3 sccm, and an AlN growth rate of 0.5 μm/h. The 0.2-μm-thick AlN layers grown under these conditions exhibit a surface roughness comparable with that of the initial sapphire substrates (rms size, ≈4.7 Å) and exhibit

a clear 2×2 RHEED pattern characteristic of a metal surface [16].

It was established that the formation of such an AlN template in the initial stage of the multilayer heterostructure technology substantially improves the structure and reduces the surface roughness of GaN layers, which improves the quality of the GaN/AlGaN interfaces and eventually significantly increases the 2DEG mobility. In particular, the full width at half maximum (FWHM) of the (0002) reflections corresponding to GaN in the ω scan mode decreased from ≈800 to 350 and 500 seconds of arc for 1-μm- and 0.2-μm-thick GaN layers. The total roughness of the obtained heterostructures also decreased practically by half with a simultaneous increase in the lateral size of separate "hills" (Fig. 1). The 2DEG parameters of the optimized multilayer heterostructures in comparison to those of the initial DHSs grown on a thin nucleation layer are presented in the table.

All multilayer heterostructures exhibited a significant increase in the carrier mobility when the temperature was decreased from 300 to 77 K, while the sheet electron density remained virtually unchanged (which was evidence of a complete localization of conduction electrons in the two-dimensional channel). The test transistors with 1-μm-long gates exhibited maximum values of the saturation current density (about 1 A/mm) and transconductance (≈180 mS/mm) already for a car-

Some 2DEG characteristics of initial and optimized multilayer heterostructures

No.	Buffer layer	Barrier layer	Sheet electron density, 10^{13} cm^{-2} 300 K/77 K	Electron mobility, cm^2/(V s) 300 K/77 K
1	Al$_x$Ga$_{1-x}$N	Undoped	1.3/1.2	500/1200
2	AlN/Al$_x$Ga$_{1-x}$N	Undoped	1.3/1.3	1450/4650
3	AlN/Al$_x$Ga$_{1-x}$N	Doped	1.6/1.6	1350/3980
4	AlN/Al$_x$Ga$_{1-x}$N	Doped	2.0/2.0	1000/2200

rier mobility of 1000 cm^2/(V s) and a sheet carrier density of $\approx 1.3 \times 10^{13}$ cm^{-2} (Fig. 2).

Conclusion. Optimization of the design and technology of multilayer heterostructures in the Al$_x$Ga$_{1-x}$N/GaN system ($0 < x < 1$) significantly improved the crystal perfection and reduced the roughness of GaN layers between the lower and upper Al-containing barrier layers. As a result, the room-temperature 2DEG carrier mobility in undoped heterostructures with $x_{Al} \approx 0.3$–0.35 in the upper barrier layer reached 1450 cm^2/(V s) at a sheet electron density of 1.3×10^{13} cm^{-2}. In heterostructures with a Si-modulation-doped barrier layer of the same composition, the mobility decreases to 1350 and 1000 cm^2/(V s) at a sheet electron density of 1.6×10^{13} and 2.0×10^{13} cm^{-2}, respectively. The experimental HEMTs with 1-μm-long gates based on the obtained multilayer heterostructures with a doped upper barrier layer exhibit stable current–voltage characteristics with maximum saturation current densities about 1 A/mm and a transconductance of up to 180 mS/mm. These 2DEG characteristics are comparable with the best data published for the classical structures with a single GaN/AlGaN heterojunction.

REFERENCES

1. Y. F. Wu *et al.*, IEEE Electron Device Lett. **25**, 117 (2004).

2. T. Kikkawa, E. Mitani, K. Joshin, *et al.*, *An Over 100 W CW Output Power Amplifier Using AlGaN/GaN HEMTs*, in *Proceedings of the International Conference on Compound Semiconductor Manufacturing Technology (GaAs MANTECH), New Orleans, 2004.*

3. R. Gaska, M. S. Shur, A. D. Bykhovski, *et al.*, Appl. Phys. Lett. **74**, 287 (1999).

4. R. A. Kiehl, P. M. Solomon, and D. J. Frank, IBM J. Res. Dev. **34**, 506 (1990).

5. Z. Bougrioua, I. Moerman, L. Nistor, *et al.*, Phys. Status Solidi A **195**, 93 (2003).

6. N. Maeda, K. Tsubaki, T. Saitoh, *et al.*, Mater. Res. Soc. Symp. Proc. **743**, L9.3.1 (2003).

7. C. Q. Chen, J. P. Zhang, V. Adivarahan, *et al.*, Appl. Phys. Lett. **82**, 4593 (2003).

8. S. B. Aleksandrov *et al.*, Fiz. Tekh. Poluprovodn. (St. Petersburg) **38**, 1275 (2004) [Semiconductors **38**, 1235 (2004)].

9. V. V. Volkov *et al.*, Pis'ma Zh. Tekh. Fiz. **30** (5), 63 (2004) [Tech. Phys. Lett. **30**, 380 (2004)].

10. RF Patent No. 2222845 (2003).

11. S. Vezian, F. Natali, F. Semond, *et al.*, Phys. Rev. B **69**, 125329 (2004).

12. D. F. Storm, D. S. Katzer, S. C. Binari, *et al.*, Electron. Lett. (2005) (in press).

13. P. Waltereit, H. Sato, C. Poblenz, *et al.*, Appl. Phys. Lett. **84**, 2748 (2004).

14. S. E. Hooper, M. Kauer, V. Bousquet, *et al.*, Electron. Lett. **40**, 33 (2004).

15. S. Arulkumaran, M. Sakai, T. Egawa, *et al.*, Appl. Phys. Lett. **81**, 1131 (2002).

16. A. R. Smith, R. M. Feenstra, D. W. Greve, *et al.*, Appl. Phys. Lett. **72**, 2114 (1998).

Translated by P. Pozdeev

Light-Induced Changes
in the Photomodulated Absorption Spectra
of Quantum-Dimensional CdSe/Dielectric Structures

V. G. Guzovskiĭ and A. I. Voĭtenkov

Institute of Metal Technology, National Academy of Sciences of Belarus, Mogilev, Belarus
e-mail: iponanb@mogilev.by
Received April 18, 2005; in final form, June 3, 2005

Abstract—The effect of additional illumination on the photomodulated absorption spectra of quantum-dimensional CdSe/dielectric structures has been studied. Using this method, it is possible to reveal additional absorption bands inside the bandgap of semiconductor nanoparticles. © *2005 Pleiades Publishing, Inc.*

The energy band structure of semiconductors (including quantum-dimensional systems) is frequently studied using modulation spectroscopy techniques [1]. These techniques are highly sensitive to optical transitions and allow their energies to be determined with high precision (to within several millielectronvolts). The methods and mechanism of electromodulation have been thoroughly studied and are described in much detail [2]. At the same time, the nature of photomodulated spectra is still incompletely clear, since the action of light leads to both electron and thermal processes in a sample. This paper demonstrates the possibility of separating the contributions of these processes by probing electron states in the bandgap of semiconductor nanoparticles using photomodulated absorption spectroscopy with additional illumination (three-beam technique).

We have studied CdSe/dielectric thin-film structures prepared by the alternating deposition of components in vacuum onto glass substrates. The structures comprised semiconductor (CdSe) inclusions in a dielectric matrix of poly(ethylene terephthalate) (PETP). The semiconductor content in the film was about 50 vol %. The bandgap of the semiconductor inclusions was $E_g = 2.0$ eV. These inclusions had the form of nanograins with an average diameter of ~6 nm [5], as evaluated from the "blue" shift in the optical absorption spectra [3]. The sample film thickness was about 0.8 μm.

The photomodulated absorption spectra were measured using the standard method [4]. The source of modulated pumping radiation was a He–Ne laser operating at $\lambda_{pump} = 633$ nm. The laser beam power density on the sample surface was 0.6 W/cm^2. The modulation frequency (43 Hz) was selected so as to provide for the best signal to noise ratio. In order to exclude the influence of nonuniform illumination on the results of absorption measurements, the laser beam diameter was several times that of the probing light beam. The sample was oriented at a Brewster angle relative to the probing beam, which excluded interference oscillations in the photomodulated transmission $\Delta T/T$ [4, 5]. The pumping and additional nonmodulated radiation beams were incident on the sample at an angle close to the normal. The constant nonmodulated illumination was provided by semiconductor lasers operating at $\lambda_{L1} = 635$ nm and $\lambda_{L2} = 670$ nm, while the illumination at $\lambda_{L3} \geq 700$ nm was ensured by an incandescent lamp with a color filter (KS19). The power of the additional nonmodulated illumination was about one-tenth of the excitation beam power. The measurements were performed at room temperature.

Figure 1 shows the spectra of photomodulated transmission $\Delta T/T$ measured with and without additional illumination at various wavelengths. The peak of $\Delta T/T$ at $h\nu = 2.0$ eV corresponds to the bandgap of semiconductor nanoparticles. The width of this peak can serve as a measure of the dimensional homogeneity of the nanostructure [5]. The second maximum observed at $h\nu = E_g - 0.2$ eV is probably related to cadmium vacancies [5, 6], which is confirmed by data on the temperature quenching of the photocurrent in CdSe films [7]. Of special interest in this study is the broad, weakly structured modulation signal observed in the range of energies significantly below E_g (Fig. 1). The photoinduced absorption in this spectral range can be explained by the trapping of photogenerated charge carriers on various structural defects, surface states of the nanoparticles, and dielectric matrix.

The effect of additional illumination was substantially selective depending on the wavelength (Fig. 1). Figure 2 shows the spectra of a relative change in the photoinduced absorption $\delta\alpha = (\Delta\alpha - \Delta\alpha_0)/\Delta\alpha_0$, where $\Delta\alpha$ and $\Delta\alpha_0$ are the values of photoinduced absorption with and without additional illumination, respectively. As can be seen, the illumination of a sample by the light with $h\nu \geq E_g$ and even with a photon energy below (but

close to) E_g (as in Fig. 2, curve *2*) decreases the photo-induced absorption in the entire wavelength range studied. One possible reason for this behavior is the limited total number of photogenerated carriers in quantum-dimensional nanoparticles. For comparable powers of the pumping and additional illumination, the latter is competitive with the exciting radiation. The additional illumination at $\lambda_{L2} = 670$ nm increases the photoinduced absorption in the region of $h\nu = E_g - 0.2$ eV, while decreasing it in all other regions (Fig. 2, curve *1*). At a constant illumination by the incandescent lamp with the KS19 filter transmitting light with $\lambda_{L3} > 700$ nm, the spectrum exhibited an additional maximum at $h\nu = E_g - 0.7$ eV (Fig. 2, curve *3*), which was not observed on the photomodulated absorption spectrum (Fig. 1). A shift of the peak from $h\nu = E_g - 0.2$ eV toward longer wavelengths with an increase in the wavelength of additional illumination is probably related to a broad absorption band (on the order of 0.25 eV) featuring a redistribution of the electron states populated by carriers generated by the additional illumination.

Let us consider the spectral region near $h\nu = E_g$ (Fig. 1), which is related to the fundamental absorption of semiconductor nanoparticles. In this region, the effect of additional illumination is manifested by a decrease in the photomodulated absorption signal. The shorter the wavelength of additional light, the greater the decrease in this signal. If the photomodulated absorption were entirely related to the thermal mechanism, the observed decrease in $\Delta\alpha$ under additional illumination could be explained only by assuming that the modulation effect occurs in a nonlinear regime (approaching saturation). However, investigations of the photoinduced absorption as a function of the pumping intensity showed that this dependence in the spectral region near $h\nu = E_g$ is linear for pumping powers up to 0.8 W/cm². Moreover, the additional illumination always changed the photomodulated absorption signal by the same value irrespective of the pumping power. These facts indicate that $\Delta\alpha$ is determined by both thermal and electron processes, which decrease the photoinduced absorption. Taking into account the small values of changes in the photoinduced absorption, we may express this effect as

$$\Delta\alpha(\lambda) = \Delta\alpha_T(\lambda) - \Delta\alpha_{el}(\lambda), \qquad (1)$$

where $\Delta\alpha_T(\lambda)$ is the thermal component and $\Delta\alpha_{el}(\lambda)$ is the electron component of changes in the photoinduced absorption. The choice of signs corresponds to the assumption that the temperature produces a "red" shift of the bandgap edge, thus increasing the photoinduced absorption, whereas the electron component produces a "blue" shift of this edge and decreases the photoinduced absorption [8].

Now let us proceed to the spectral region near $h\nu = E_g - 0.2$ eV, where an additional photoinduced absorp-
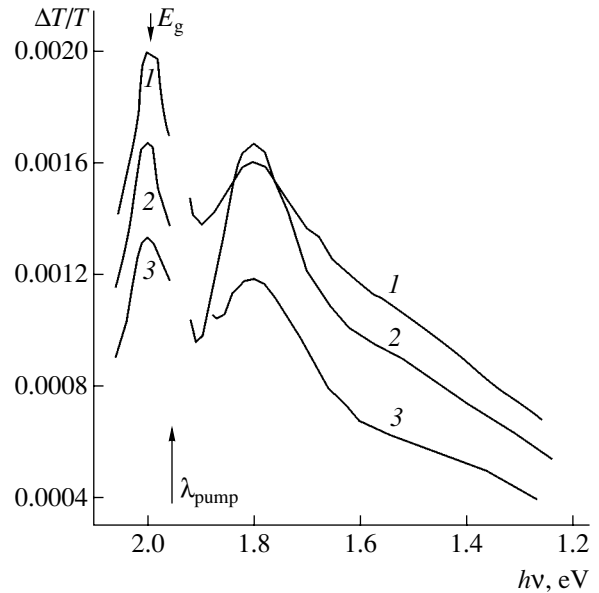

Fig. 1. The spectra of photomodulated transmission $\Delta T/T$ of a CdSe/PETP thin-film structure measured without additional illumination of the sample (curve *1*) and with such illumination at $\lambda_{L2} = 670$ nm (curve *2*) and $\lambda_{L1} = 635$ nm (curve *3*). E_g is the bandgap width of CdSe; λ_{pump} is the modulated pumping radiation wavelength.
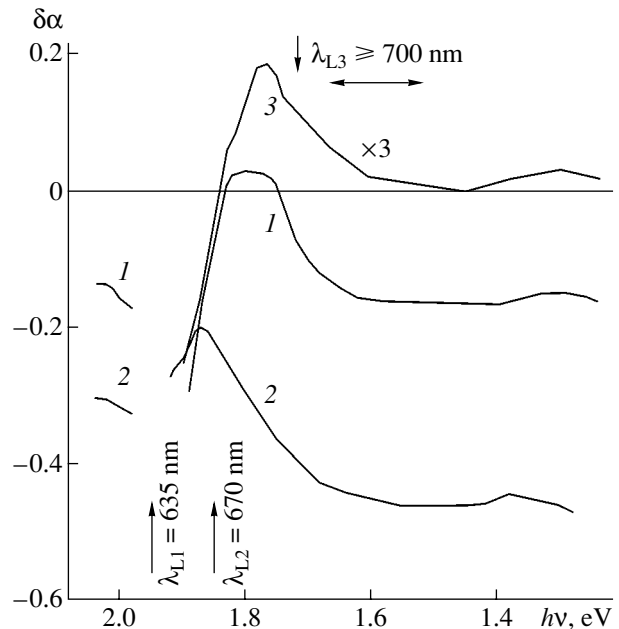

Fig. 2. The spectra of the change $\delta\alpha$ in the photoinduced absorption T of a CdSe/PETP thin-film structure measured with additional illumination of the sample at 670 nm (curve *1*), 635 nm (curve *2*), and ≥700 nm (curve *3*). The ordinate scale for curve *3* is multiplied by a factor of 3.

tion maximum is observed (Figs. 1 and 2). As was noted above, this maximum can be attributed to the absorption of light by electrons occurring on the energy levels formed by cadmium vacancies. An increase in the pho-

toinduced absorption in the presence of additional illumination at $\lambda_{L2} = 670$ nm is probably related to an increase in the slope of $\alpha(\lambda)$ in this region of wavelengths. This, in turn, is due to a decrease in the total number of optical transitions from these energy levels. Since this energy region (in contrast to that where $h\nu > E_g$) contains a lower density of electron states, the additional illumination saturates the electron transition and excludes it from the pumping–probing scheme. In terms of Eq. (1), this is manifested by a decrease in the electron contribution $\Delta\alpha_{el}$ to the total photomodulated absorption signal (since the constant illumination does not influence the thermal component).

The additional maximum in the change of photoinduced absorption at $h\nu = E_g - 0.7$ eV, which is observed for the additional illumination at $\lambda_{L3} \geq 700$ nm, is probably also explained by the factors considered above. Data on the optical quenching of a photocurrent in CdSe films showed that the behavior in this spectral region is influenced by the so-called slow recombination centers, which represent complex defects including cadmium and selenium vacancies [7]. It should also be noted that the additional nonmodulated illumination (continuous in a broad wavelength range) decreases the photoinduced absorption and reveals no additional features in the bandgap.

In concluding, an additional nonmodulated illumination makes it possible to act upon the electron component of the photoinduced absorption at low modulation frequencies (<1 kHz). The use of such additional illumination at various fixed wavelengths in the course of photomodulated absorption measurements provides new possibilities in the investigation of features of the energy band structure of semiconductor (CdSe) nanoparticles.

REFERENCES

1. V. L. Colvin, K. L. Cunningham, and A. P. Alivisatos, J. Chem. Phys. **101**, 7122 (1994).

2. Y. S. Tang, J. Appl. Phys. **69**, 8298 (1991).

3. A. S. Borbitskiĭ, A. I. Voitenkov, and V. P. Red'ko, Pis'ma Zh. Tekh. Fiz. **22** (13), 1 (1996) [Tech. Phys. Lett. **22**, 517 (1996)].

4. M. Cardona, *Modulation Spectroscopy* (Academic Press, New York, 1969).

5. A. I. Voitenkov and V. G. Guzovski, in *Proceedings of the Belarus–Russia Seminar "Nanostructural Materials-2000," Minsk, 2000*, pp. 115–118.

6. A. I. Voitenkov and V. G. Guzovski, in *Physics, Chemistry and Application of Nanostructures,* Ed. by V. E. Borisenko, A. B. Filonov, S. V. Gaponenko, and V. S. Gurin (World Scientific, Singapore, 1999), pp. 115–118.

7. V. S. Grinkevich *et al.*, Izv. Vyssh. Uchebn. Zaved., Fiz., No. 5, 106 (1990).

8. P. S. Kireev, *Semiconductor Physics* (Vysshaya Shkola, Moscow, 1969; Mir, Moscow, 1978).

Translated by P. Pozdeev

Two Universal Regimes of Adhesive Film Peeling

A. É. Filippov[a] and V. L. Popov[a,b,*]

[a] *Donetsk Physicotechnical Institute, Donetsk, Ukraine*
[b] *Berlin Technical University, Berlin, Germany*
* *e-mail: v.popov@tu-berlin.de*
Received May 17, 2005

Abstract—A numerical model describing the process of thin adhesive film peeling off a solid surface is considered. A qualitative distinction between the "microscopic" picture and the notions of the standard theory of adhesion (based on the energy balance) consists in that separate elements of the film peel off the surface along virtually the same trajectory irrespective of the direction of the external force action. A more thorough analysis shows that a fine difference between the scenarios of behavior in the vicinity of the touch point still exists, so that one can speak of two classes of universality, corresponding to $\alpha < \pi/2$ and $\alpha > \pi/2$. The results of analysis of the proposed microscopic model allow a more correct macroscopic criterion to be formulated for the adhesive surface peeling. © 2005 Pleiades Publishing, Inc.

Introduction. In recent years, increasing attention has been devoted to the phenomenon of adhesion in various fields, such as contact mechanics, tribology, and the technology of adhesives and, especially, of self-adhesive materials [1]. A large number of investigations have been devoted to theoretical aspects of the adhesive interactions as well as to their practical aspects [1–3]. One particular task of these investigations has been inspired by the need of robot technology in creating artificial surfaces of the gecko foot type capable of sticking (reversibly) to solid surfaces of various kinds. Theoretical investigations of the adhesive contacts usually proceed from the main idea of the classical Johnson–Kendall–Roberts (JKR) theory [4], which is based on an analysis of the balance of the elastic energy of deformation of contacting bodies and the contact surface energy. However, as will be shown below, this simple microscopic approach does not always provide for an adequate description of the laws of adhesion.

The simplest example of the application of the energy approach in the theory of adhesion is offered by a thin, flexible and nonstretchable film peeling off a flat solid surface (Fig. 1). The force per unit length of the peel-off line at an angle α relative to the substrate surface will be denoted $\mathbf{F} = \{F_x, F_z\} = \{F\cos\alpha, F\sin\alpha\}$, and the energy necessary to separate a unit film area from the substrate surface (i.e., the effective surface energy of interaction between the film and substrate) will be denoted γ. Let us calculate the angle α for which the peel-off line occurs in equilibrium. As the contact length between the film and the substrate surface increases by Δl, the film energy decreases by $\gamma\Delta l$, the end of the film travels over a certain distance s and performs the work Fs against the pull-off force F. In equilibrium, we have $Fs = \gamma\Delta l$. As can be readily shown, $s = \Delta l(1 - \cos\alpha)$ and, hence, $F_0(1 - \cos\alpha) = \gamma$. Here, F_0 is

the pull-off force, below which the film exhibits self-adhesion and above which the film peels off. Thus, the critical pull-off force is a monotonic function of the peeling angle:

$$F_0 = \gamma/(1 - \cos\alpha), \qquad (1)$$

which decreases from $F_0 \gg \gamma$ at small angles ($\alpha \ll 1$) to $F_0 = \gamma/2$ at $\alpha = \pi$.

Microscopic model. If the above standard energy considerations were correct, it would be possible to reproduce the result described by relation (1) in a microscopic model with a surface energy modeled by interactions between solids (of the van der Waals force type). However, the results of an analysis of the microscopic model described below show that direct modeling leads to behavior qualitatively different from that predicted by relation (1).
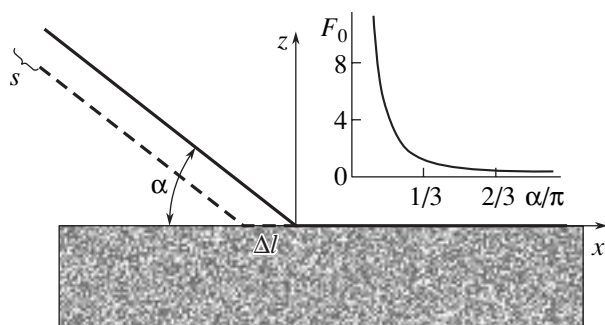

Fig. 1. Geometry of film peeling off a flat solid substrate surface (see the text for explanations). The inset shows a plot of the critical pull-off force F_0 versus angle α corresponding to formula (1).
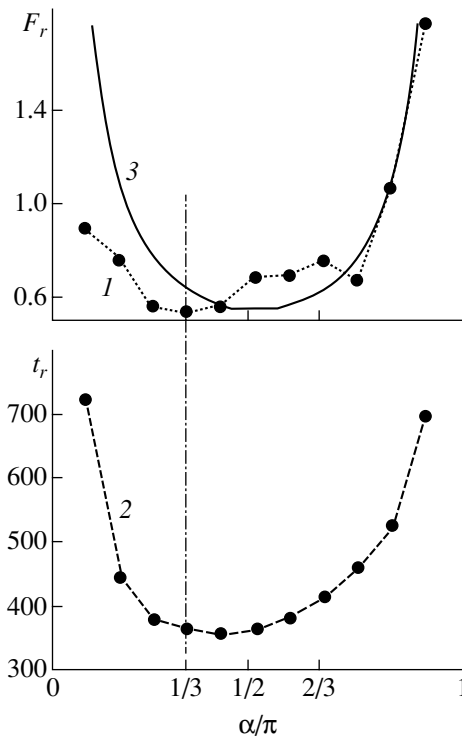
Fig. 2. Plots of (*1*) the critical pull-off force F_r for the film peeling and (*2*) the total peel-off time t_r versus angle α as determined by numerical calculations. Curve *3* corresponds to the macroscopic theory taking into account the work performed only by the vertical force component.

For the sake of simple and illustrative representation of results, our consideration below will be restricted to a one-dimensional elastic chain. However, the results of our additional numerical experiments showed that virtually all results obtained for this simple model can be reproduced in a more realistic model of a two-dimensional adhesive film. In constructing the simple microscopic model, we have to take into consideration at least the following factors: the elastic interaction between elements (segments) of the chain, their attraction to the surface of the substrate and repulsion from its deeper layers, and the external pull-off force.

In order to reproduce the elastic properties of a system, it is usually sufficient to restrict consideration to the linear elastic bonds in a sequence of "material points" spaced by dx, which represent the neighboring surface elements with the coordinates $z(x + dx)$ and $z(x)$: $K[z(x + dx) - z(x)]$, where K is the elastic constant characterizing the interaction between mobile elements in the elastic chain. However, the linear bonds cannot determine the distance between elements in cases where the chain is freely moving in space rather than being supported on a certain "substrate." For adequate modeling of such a chain, the elastic bonds should be nonlinear [5–7]. In a widely used simple variant (see, e.g., [8] and references therein), it is possible to restrict consideration to a fourth-order interaction potential of

the type $U^{\text{elastic}}(r) = r^2(1 - r^2/2)/2$, where $r^2 = dx^2 + [z(x + dx) - z(x)]^2$. Then, the required components $F_x^{\text{elastic}} = -\partial U^{\text{elastic}}/\partial x$ and $F_z^{\text{elastic}} = -\partial U^{\text{elastic}}/\partial z$ of the force of interaction between elements are characterized by the cubic nonlinearity that does not admit rupture of the chain and (for the elastic constant $K = 4$ used below) quite rigidly sets the distance between elements.

The surface acts upon each element in the chain with the van der Waals force with the components $F_x^{\text{adhesion}} = -\partial U^{\text{adhesion}}/\partial x$ and $F_z^{\text{adhesion}} = -\partial U^{\text{adhesion}}/\partial z$ corresponding to the adhesion potential U^{adhesion}. This potential can in most cases be represented by a pair of Gaussians with opposite signs and variable width, which describe the attraction partly compensated by the repulsion at short distances: $U^{\text{adhesion}}(r) = C\exp(-r^2/c) + D\exp(-r^2/d)$. This "seeding" potential (calculated for $C = 0.8$, $c = 0.2$, $D = -8$, and $d = 1$) is depicted by the thick gray curve in Fig. 4. Since this potential does not provide for a repulsion of the chain from the "bulk" substrate, it has to be supplemented with a δ-like term $U^{\text{bulk}} = U_0\delta(z)$ ($U_0 \gg D$; in the calculation, $U_0 = 300$), which represents a step force supporting the sticking chain on the substrate surface: $F_z^{\text{bulk}} = -\partial U^{\text{bulk}}/\partial z$.

For certainty, let us consider the case of a chain peeled off the surface by the external force $\mathbf{F}^{\text{ext}} = K^{\text{ext}}(\mathbf{V}t - \mathbf{r}_1)$, which is developed by a spring extended between the first chain segment $\mathbf{r}_1 = \{x_1, z_1\}$ and a holder moving away at the angle α with the velocity $\mathbf{V} = \{V_x, V_z\} = \{V\cos\alpha, V\sin\alpha\}$ (in the calculation, $V = 0.2$).

In the overdamped limit, the dynamic equations for the model described above appear as

$$\frac{\partial x}{\partial t} = F_x^{\text{elastic}} + F_x^{\text{adhesion}} + F_x^{\text{ext}};$$
$$\frac{\partial z}{\partial t} = F_z^{\text{elastic}} + F_z^{\text{adhesion}} + F_z^{\text{ext}} + F_z^{\text{bulk}}.$$
(2)

Results and discussion. The main results of numerical modeling using system (2) are presented in Fig. 2, which shows plots of the critical pull-off force F_r for the film peeling (curve *1*) and the total peel-off time t_r (curve *2*) as functions of the angle α. As can be seen, the obtained behavior of $F_r(\alpha)$ cannot be described using the function $\gamma/(1 - \cos\alpha)$ predicted by the macroscopic theory (see the inset in Fig. 1).

A qualitative distinction of the "microscopic" pattern from the simple geometry used to derive relation (1) consists in the fact that each segment of the elastic chain peels off the surface along virtually the same trajectory irrespective of the direction of the external force action. At the terminal touch point, the flat surface is tangent to this trajectory.
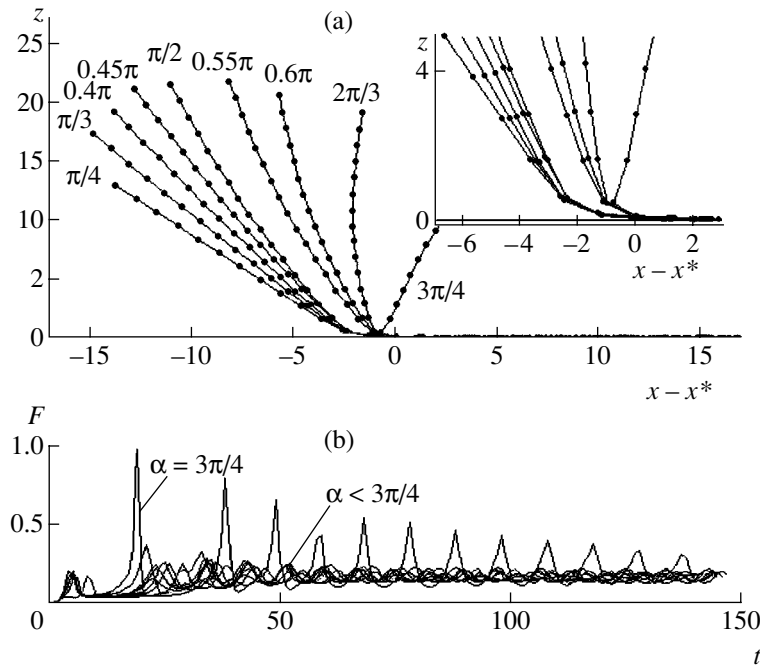
Fig. 3. Two types of the universal behavior at the point of film peeling off the substrate surface: (a) film configurations in the mobile frame related to the touch point $x = x^*$ for the peeling at various angles (the inset shows the vicinity of the touch point on a greater scale); (b) quasi-periodic time variation of the force acting on the segment at the touch point.

A more thorough analysis shows that a fine difference between the scenarios of behavior in the vicinity of the touch point still exists (see Fig. 3 and the legend to this figure), so that one can speak of two classes of universality, corresponding to $\alpha < \pi/2$ and $\alpha > \pi/2$. However, this difference is much smaller than might have been expected in the entire broad range of angles $0 < \alpha < \pi$.

As can be seen from Fig. 2, the critical force and the efficiency of work performed by this force (characterized by the total peel-off time for a chain of certain length) as functions of the angle α are almost symmetric relative to the vertical line $\alpha = \pi/2$. Taking this symmetry into account, we have to revise the process of a chain peeling off the substrate surface.

Since every sequential segment peels off the surface along the tangent, the horizontal component of the external force is "spent" to perform the work (against the elastic force) on elongating the chain segments in this direction. Therefore, only the vertical force component $F_x^{\text{ext}} = F\sin\alpha$ works against the adhesion potential U^{adhesion}. Over a distance on the order of the potential width d, this force has to perform a work sufficient to detach the chain segment: $F_r d\sin\alpha = U^{\text{adhesion}}|_{z=0}$. This corresponds to the angular dependence of the pull-off force $F_r \sim 1/\sin\alpha$, which provides a very good approximation (Fig. 2, curve *3*) of the results of numerical modeling.

In the discrete numerical description of the system (and in real molecular chains), this scenario of segment peeling off the surface must lead to an almost periodic step process. According to this scenario, each segment extends to a certain (nearly equilibrium) length and simultaneously peels off the surface. Subsequent extension involves the next element into this motion and so on. This process leads to a quasi-periodic time variation of the force $F(t)$ in the region of peeling (Fig. 3). As can be seen, the oscillations in $F(t)$ are most pronounced for the sliding angles close to $\alpha = \pi$. In the continuum limit (where the spacing of chain segments is much smaller than the characteristic width of the adhesion potential), $F(t)$ degenerates into a monotonic function.

The effective potential $U_{\text{eff}}^{(k)}(z)$, which acts upon an arbitrary inner kth segment in the chain at a distance z from the substrate surface, can be determined by a numerical integration of the vertical force component $F^z(z(t))$ over the time series $z(t)$:

$$U_{\text{eff}}^{(k)}(z) = \int F(z(t))dz(t). \qquad (3)$$

Figure 4 shows the results of such integration for various angles α. The obtained potential is in good agreement (with allowance for oscillations related to the detachment of sequential discrete segments) with the "seeding" adhesion potential. For relatively small deviations of α from $\pi/2$ ($\pi/4 < \alpha < 3\pi/4$), the effective potential is virtually independent of the external force direction. This behavior confirms the above assumption that, in most cases, the chain peels off the substrate in a
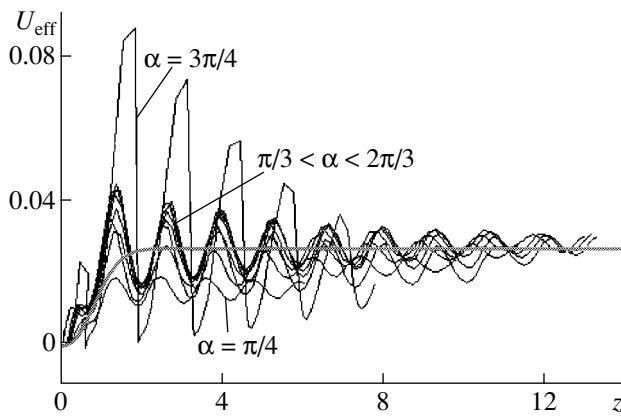
Fig. 4. The effective potential U_{eff} acting upon an arbitrary (inner) segment in the chain at a distance z from the substrate surface as determined by numerical integration of the vertical force component $F(z(t))$ over the time series $z(t)$ for various angles α. The thick gray solid curve shows the "seeding" adhesion potential entering into the equations of motion.

universal manner and the process rate is determined predominantly by the vertical force component.

The obtained results lead to the following conclusions.

(i) The microscopic process of adhesive bond rupture cannot be adequately described within the framework of the macroscopic approach based on the energy balance.

(ii) The most adequate macroscopic description with allowance for a real microscopic process can employ the principle of virtual work only for the vertical force component. The horizontal component apparently performs work against other forces, such as the force of friction in the adhesive contact, which are usually not taken into consideration in the macroscopic theory of adhesion.

REFERENCES

1. B. N. J. Persson, O. Albohr, U. Tartaglino, *et al.*, J. Phys.: Condens. Matter **17**, R1 (2005).

2. B. N. J. Persson and S. Gorb, J. Chem. Phys. **119**, 11437 (2003).

3. A. K. Geim, S. V. Dubonos, I. V. Grigorieva, *et al.*, Nature Mater. **2**, 641 (2003).

4. K. Johnson, *Contact Mechanics* (Cambridge Univ. Press, Cambridge, 1987).

5. E. Fermi, J. Pasta, S. Ulam, and M. Tsingou, Los Alamos Sci. Lab. Rep., LA-1940; E. Fermi, J. Pasta, and S. Ulam, *The Many-body Problem,* in *Encyclopedia of Exactly Solved Models in One Dimension*, Ed. by D. C. Mattis (World Scientific, Singapore, 1993).

6. J. Ford, Phys. Rep. **213**, 271 (1992).

7. A. J. Lichtenberg and M. A. Lieberman, *Regular and Chaotic Dynamics* (Springer, New York, 1992).

8. A. E. Fillipov, B. Hu, B. Li, and A. Zeltser, J. Phys. A **31**, 7719 (1998).

Translated by P. Pozdeev

Use of the Anisotropic Magnetoresistance Effect for Direct Measurement of the Coercivity and Exchange Bias Fields of Magnetization Reversal in Conducting Magnetic Films of Nanometer Thickness

A. V. Medved[a],*, R. G. Kryshtal[a], A. I. Krikunov[b], and S. I. Kasatkin[b],**

[a] *Institute of Radio Engineering and Electronics (Fryazino Branch), Russian Academy of Sciences,
Fryazino, Moscow oblast, Russia*
[b] *Institute for Control Problems, Russian Academy of Sciences, Moscow, Russia*
e-mail: * avm@ms.ire.rssi.ru; ** serkasat@ipu.rssi.ru
Received May 17, 2005

Abstract—The anisotropic magnetoresistance effect has been used for direct measurement of the coercivity and exchange bias fields of magnetization reversal in conducting ferromagnetic films of nanometer thickness and in sandwich structures containing such films, which are used in spin dependent tunneling junctions featuring colossal magnetoresistance. The measurements have been performed for 25-nm-thick permalloy (Py) films obtained by RF magnetron sputtering on oxidized silicon substrates and for FeMn(15 nm)/Py(10 nm)/SiC(1.5 nm)/Py(10 nm) structures on glass ceramic substrates. The results of measurements performed using the proposed method are in satisfactory agreement with the data obtained by the induction method. © 2005 Pleiades Publishing, Inc.

Important characteristics of the nanodimensional magnetic films used in spin dependent tunneling (SDT) magnetoresistive elements [1, 2] include the coercivity field and the magnetization reversal field bias caused by the exchange interaction in structures comprising ferromagnetic films and antiferromagnetic pinning layers [3]. The films in such elements usually have the shape of narrow stripes. For multilayer structures with films having the shape of disks or rectangles of relatively large size, these characteristics can be determined using the measurements of magnetization in an external magnetic field. Such measurements are performed using special setups (see, e.g., [4, 5]), which are not always suitable for the investigation of structures having relatively small lateral dimensions.

There are alternative techniques based on the anisotropic magnetoresistance (AMR) effect [6, 7]. The AMR phenomenon consists in the variation of the electric resistance R of a film depending on the direction of its magnetization vector rotated in an external magnetic field [6]:

$$R = R_0 + \Delta R_{AMR} \cos^2 \theta, \qquad (1)$$

where θ is the angle between the electric current direction and the magnetization vector in the sample, R_0 is the resistance at $\theta = \pi/2$, and ΔR_{AMR} is the maximum change in the sample resistance under the action of the applied magnetic field. Previously [6, 7], AMR mea-surements were performed for samples either possessing relatively large lateral dimensions or specially prepared so as to provide for a sufficiently high sensitivity. For this purpose, the samples were cut from a "wide" film so that the anisotropy axis made an angle of $\theta_a = 45°$ with the direction of current in the sample. In practice, the SDT magnetoresistive elements are usually made so that the anisotropy axis is oriented along the stripe ($\theta_a = 0$). The characteristics of such STD structures are calculated using experimental angular dependences of the magnetoresistance and formulas obtained within the framework of various theoretical models.

This Letter presents for the first time the results of the direct (not using theoretical models) determination of the exchange bias and coercivity fields in nanodimensional conducting magnetic films and related structures, in which the anisotropy axis coincides with the current direction. The measurements were performed for the samples with lateral dimensions on the same order of magnitude as those of the film elements used in SDT structures. We have measured the dependence of the resistance on the magnetic field, which was oriented parallel to the anisotropy axis in the sample. At first glance, the sample resistance in this geometry (where the anisotropy axis coincides with the direction of current and the magnetic field (1)) must not depend on the magnetic field because the angle between this field (and, hence, the magnetization vector) and the current remains unchanged. However, our experiments showed that the resistance exhibits a noticeable change
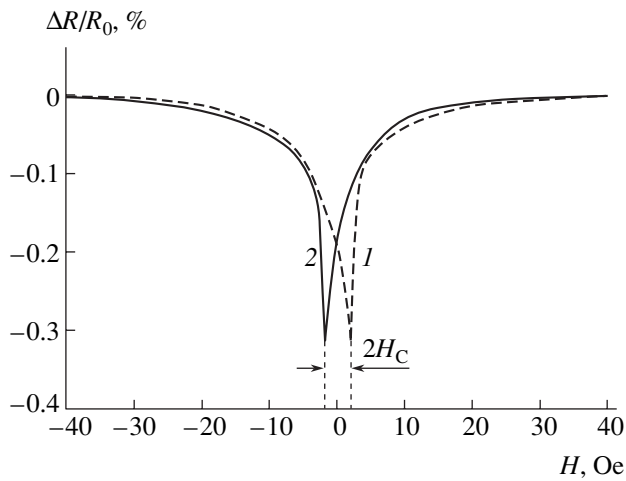
Fig. 1. Plots of the relative change $\Delta R/R_0$ in the sample resistance versus magnetic field H for a single permalloy film in the field oriented along the stripe and varied in the (*1*) increase and (*2*) decrease mode. H_C is the coercive force.
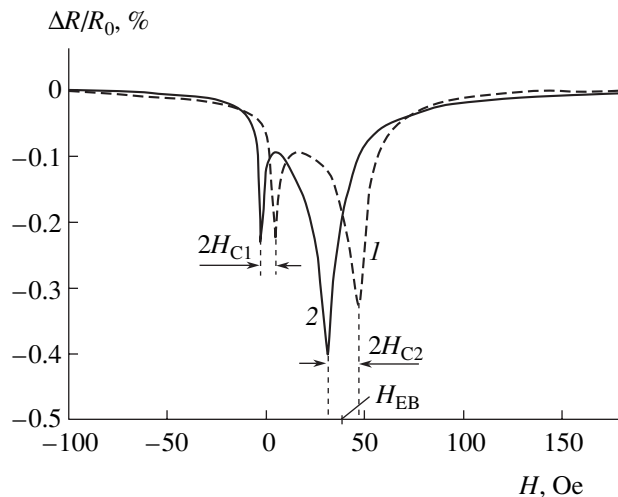

Fig. 2. Plots of the relative change $\Delta R/R_0$ in the sample resistance versus magnetic field H for a FeMn–Py–SiC–Py structure in the field oriented along the stripe and varied in the (*1*) increase and (*2*) decrease mode. H_{EB} and H_{C1} are the exchange bias and coercive force of the Py film contacting with the FeMn layer; H_{C1} is the coercive force of the Py film not contacting with the FeMn layer.

as a result of the motion of domain boundaries (where the magnetization vector changes its direction), since the volume of such domain boundaries can be sufficiently large. At a field strength close to the coercive force of the magnetic film, the volume of domain boundaries featuring the magnetization vector rotation sharply increases, the effective θ value becomes nonzero, and the resistance of the sample decreases. Thus, the determination of the external magnetic field corresponding to the maximum volume of domain

boundaries provides a means of directly measuring the coercive force and the exchange bias of the magnetization reversal field.

The samples of conducting magnetic fields with uniaxial anisotropy were prepared by the RF magnetron sputter deposition of 25-nm-thick permalloy (Py) layers on oxidized silicon substrates. The exchange bias of the magnetization reversal field was studied in FeMn(15 nm)/Py(10 nm)/SiC(1.5 nm)/Py(10 nm) structures grown by the same method on glass ceramic (Sitall) substrates. The films had the shape of 70-mm-long stripes with a width of 100 μm. The direction of magnetic anisotropy in the samples of both types was set by the orientation of external magnetic field in the course of film growth.

A sample was exposed to a magnetic field with constant orientation in the plane of the film, and the resistance R was measured as a function of the field strength H varied (in the monotonic increase and decrease modes) from −400 to +400 Oe. The measurements were performed at room temperature in the dc mode. The results of measurements were virtually the same over a range of dc currents from 1 to 100 μA.

Figure 1 shows plots of the relative change $\Delta R/R$ in the sample resistance versus magnetic field H for a single permalloy film measured in the field oriented along the stripe. As can be seen, $\Delta R/R \leq 0$ in the entire range of the magnetic field variation. When the field approaches the coercive force value H_C, the $\Delta R/R$ value exhibits a sharp decrease, which is manifested by narrow minima in the curves. The coercive force of a single Py film was found to be $H_C = 1.5$ Oe, which is in good agreement with the results of measurements performed by other methods.

Figure 2 presents the results of measurements for a multilayer structure in the field oriented along the stripe. As can be seen, each $\Delta R/R$ curve exhibits two narrow minima. One of these (H_{C1}) corresponds to the magnetization reversal in the Py film not contacting with the antiferromagnetic (FeMn) layer, and the second minimum (H_{C2}) reflects the magnetization reversal in the other Py film, which is biased due to the exchange interaction with the FeMn layer. The minima measured in the field increase and decrease mode exhibit relative shifts as a result of the coercivity. The experimental curves show that $H_{C1} = 4$ Oe, $H_{C2} = 7.5$ Oe, and the exchange bias is $H_{EB} = 39$ Oe. The coercivity and exchange bias of the magnetization reversal field in multilayer structures prior to the stripe patter formation were previously measured using the induction method [5]. With allowance for the demagnetization factor related to the sample shape and the zig-zag domain boundary pinning at the stripe edges, the results obtained by two methods show satisfactory agreement.

REFERENCES

1. V. I. Borisov, A. I. Krikunov, A. I. Chmil', *et al.*, Radiotekh. Élektron. (Moscow) **49**, 84 (2004).

2. D. Wang, C. Nordman, J. M. Daughton, *et al.*, IEEE Trans. Magn. **30**, 2269 (2004).

3. T. Zhao, K. Zhang, and H. Fujiwara, J. Appl. Phys. **91**, 6890 (2002).

4. V. Franco, J. Ramos-Martos, and A. Conde, Rev. Sci. Instrum. **67**, 4167 (1996).

5. A. M. Murav'ev, S. I. Kasatkin, and F. F. Popadinets, Zavod. Lab., No. 7, 23 (2001).

6. B. H. Miller and E. Dan Dahlberg, Appl. Phys. Lett. **69**, 3932 (1996).

7. K.-U. Barholz and R. Mattheis, IEEE Trans. Magn. **38**, 2767 (2002).

Translated by P. Pozdeev

Optical Properties of Interstellar Medium

S. G. Yastrebov* and V. I. Ivanov-Omskiĭ

Ioffe Physicotechnical Institute, Russian Academy of Sciences, St. Petersburg, 194021 Russia
* e-mail: yastrebov@mail.ioffe.ru
Received June 2, 2005

Abstract—The spectra of normalized extinction of electromagnetic radiation by the interstellar medium have been analyzed in terms of a model representing the total extinction as a sum of three absorption coefficients. The first coefficient is related to optical transitions of the π–π^* type and the second is related to those of the σ–σ^* type in amorphous carbon. The third term represents two absorption features occurring in the region of the π–π^* type transitions in the amorphous phase, which are satisfactorily described by the Gaussian contours peaked at 3.2 eV (385.6 nm) and 5.67 eV (217.5 nm). These contours are compared to published data on the absorption spectra of a copolymer composed of alternating triphenylamine and fluorene molecules. The results of this analysis confirm the hypothesis concerning the most probable chemical composition and physical state of particles of the interstellar medium. © 2005 Pleiades Publishing, Inc.

Investigations of the optical properties of the interstellar medium (ISM) [1, 2] are important for deeper insight into the nature of the particles constituting this medium. Primary attention in this paper is devoted to carbon as the most probable component of such particles. There are many hypotheses concerning the allotropic forms of carbon entering into ISM particles. However, we believe that, in view of the long-term irradiation of the interstellar dust particles by cosmic rays, only the amorphous carbon (a-C) can be considered as the most probable candidate structural material for the ISM among the numerous existing allotropic modifications of carbon, including graphite [3], fullerenes [4], carbon nanotubes and onions [5, 6], aromatic hydrocarbons [7, 8], and amorphous species [9]. As will be shown below, the hypothesis assuming an amorphous structure of the interstellar substance makes it possible to analyze details of the normalized interstellar extinction (NIE) spectrum and to refine the chemical composition and physical state of particles in the ISM.

The main idea of the proposed approach is to compare the NIE spectrum to the optical absorption spectrum of a-C. As is known, electrons of the two (π and σ) subsystems determine the contributions to the optical absorption of a-C in the partly overlapping spectral intervals [11]: the transitions of π electrons from occupied to vacant states (π–π^*) occur in the range of photon energies $0 \lesssim \varepsilon \lesssim 8$ eV, while transitions of the second type (σ–σ^*) are manifested at $\varepsilon \gtrsim 8$ eV [10]. This circumstance makes it possible to separate the two contributions in the dielectric response of a medium containing a-C. Accordingly, the total optical absorption coefficient α of a-C can be written as a sum

$$\alpha = \sum_{j=1}^{2} \alpha_j, \tag{1}$$

where $j = 1$ and 2 refers to transitions of the first and second type, respectively.

Previously, we demonstrated [12] that the absorption coefficient α_j as a function of the photon energy ε for a-C has the following form:

$$\alpha_j(\varepsilon) = \frac{A_j}{\varepsilon} \exp\left(-\frac{(2E_{Gj} + E_{gj} - \varepsilon)^2}{4s_j^2}\right) \mathrm{erf}\left(\frac{\varepsilon - E_{gj}}{2s_j}\right),$$
$$\varepsilon \geq E_{gj}. \tag{2}$$
$$\alpha_j(\varepsilon) = 0, \quad \varepsilon < E_{gi}.$$

Here, A_j is a constant factor, E_{Gj} is the energy corresponding to the maximum density of electron states, s_j is the characteristic of smearing of the density of states, and E_{gj} is the energy gap between occupied and vacant states in the electron energy spectrum [13]. Relations (1) and (2) can be used for evaluating the contribution due to a-C in the total NIE.

Figure 1 shows a dispersion of the normalized extinction α_{ist} reconstructed from the experimental NIE spectrum[1] $k(\lambda)$ [2] using the relations

$$\alpha_{ist}(\lambda) = k(\lambda) + C,$$
$$k(\lambda) = (E(\lambda - V)/E(B - V)). \tag{3}$$

Here, λ is the wavelength of absorbed photons, the expression in parentheses represents experimental NIE data (the function E and the quantities V and B are denoted as in [2]), and C is a constant term added to the experimental data so as to obey the condition $\alpha_{ist}(\varepsilon) \geq 0$ that is necessary for calculating the contributions $\alpha_1(\varepsilon)$ and $\alpha_2(\varepsilon)$ to the total dispersion $\alpha_{ist}(\varepsilon)$. The latter con-

---

[1] The original experimental data were kindly provided by D. Massa.

stant was selected using the asymptotic relation $C \approx k(\lambda \longrightarrow \infty)$.

The results of the calculation of $\alpha_1(\varepsilon)$ and $\alpha_2(\varepsilon)$ are also presented in Fig. 1. The values of variables A_j, E_{Gj}, s_j, and E_{gj} ($j = 1, 2$) entering into expressions (1) were determined by least squares through minimization of the variance functional

$$F(A_1, A_2, E_{G1}, E_{G2}, s_1, s_2, E_{g1}, E_{g2})$$

$$= \sum_i (\alpha_1(\varepsilon_i) + \alpha_2(\varepsilon_i) - \alpha_{ist}(\varepsilon_i))^2, \quad (4)$$

where i is the index of points on the experimental NIE curve ($i = 0–1200$). The values of parameters determined using this procedure are listed in the table (the curves of $\alpha_1(\varepsilon)$ and $\alpha_2(\varepsilon)$ corresponding to these values are depicted in Fig. 1). As can be seen from data in the table, the energy gap for transitions of the second type is $E_{g2} = 0$, which reflects a significant degree of amorphization of a-C particles in the ISM under the action of cosmic rays. Here, by amorphization we imply both disorder in the mutual arrangement of carbon atoms in the material and fluctuations of the interatomic distances and bond angles, as well as the presence of ruptured bonds between the nearest neighbors.

The value of E_{g1} can be used for estimating the number of graphene rings entering into compact clusters. Such clusters, representing incomplete fragments of graphite planes, can be elements of the a-C structure on the intermediate scale [11]. In order to obtain this estimate, we use the expression [11]

$$E_{g1} = 2|\beta|M^{-1/2}, \quad (5)$$

where M is the average number of graphene rings and $\beta \approx -1,4$ eV is the parameter characterizing the local interaction of π electrons in a cluster. Substituting the E_{g1} value from the table into relation (5), we estimate the average number of rings as $M \approx 27$.

Figure 2 presents a comparison of the experimental normalized extinction (points) to the sum of absorption coefficients $\alpha_1(\varepsilon) + \alpha_2(\varepsilon)$ depicted by the dashed curve. A difference between $\alpha_{ist}(\varepsilon)$ and the calculated sum clearly reveals two features in the extinction (Fig. 2, open squares). As can be seen, these features can be satisfactorily described by Gaussian profiles. A contribution to the FP feature [2] manifested by a shoulder in the absorption band is due to a π–π^* transition with an energy of about 3.2 eV.

For the further analysis of the features of ISM extinction, we have compared the absorption bands revealed in Fig. 2 to the absorption spectra of copolymers containing six-member graphene rings. The energies of maxima (3.2 and 5.67 eV) observed on this extinction curve exhibit a striking coincidence with the energy positions of the most intense bands in the absorption spectrum of a copolymer of triphenylamine
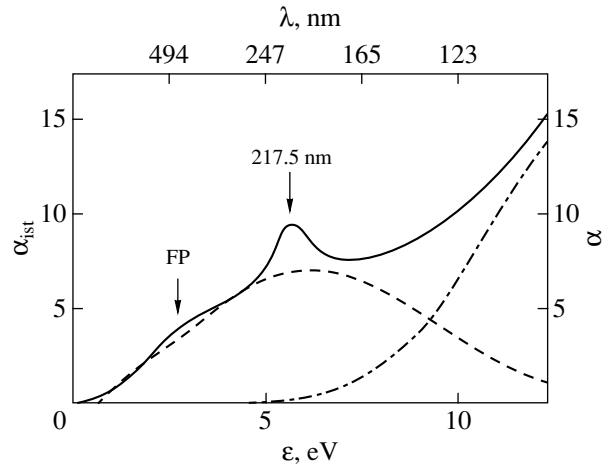

Fig. 1. Variation of the normalized extinction α_{ist} as a function of the absorbed photon energy (solid curve). Dashed and dash-dot curves show the $\alpha_1(\varepsilon)$ and $\alpha_2(\varepsilon)$ calculated using Eqs. (1) and (2) with the values of parameters listed in the table. The FP arrow indicates a shoulder in the NIE spectrum reported in [2].
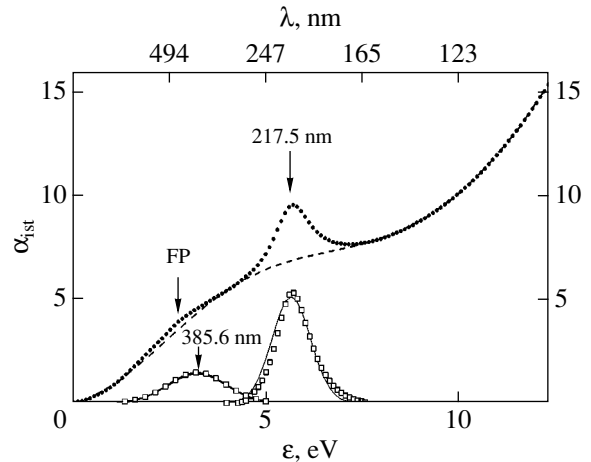

Fig. 2. A comparison of the experimental normalized extinction α_{ist} (points) and the sum of contributions $\alpha_1(\varepsilon)$ and $\alpha_2(\varepsilon)$ due to optical transitions of the first (π–π^*) and second (σ–σ^*) types (dashed curve). Open squares show a difference (multiplied by a factor of 2) between the experimental (α_{ist}) and calculated ($\alpha_1 + \alpha_2$) curves (solid curves show the best fit to Gaussian profiles). The FP arrow indicates a shoulder in the NIE spectrum reported in [2].

$(C_6H_5)_3N$ and fluorene $C_{13}H_{10}$ [14]. This coincidence is illustrated in Fig. 3, which shows a comparison of the experimental absorption spectrum of a triphenylamine–

The values of coefficients in Eq. (1) determined by least squares fitting to experimental NIE data [2]

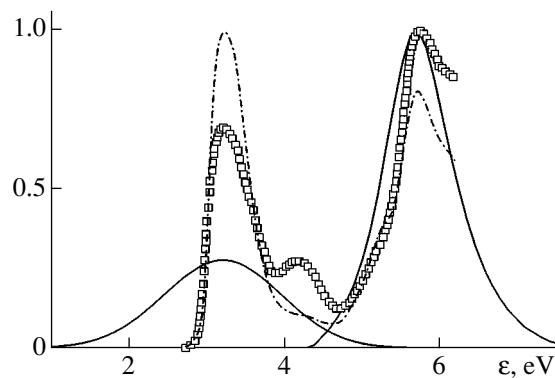| j	A_j, eV	E_{gj}, eV	E_{Gj}, eV	s_j, eV
1	49	0.54	3.36	2.29
2	215	0	7.1	1.95

Fig. 3. A comparison of the features (fitted by Gaussian profiles) revealed in Fig. 2 to the experimental optical absorption spectra of a copolymer composed of alternating triphenylamine and fluorene molecules (open squares) [14] and the spectrum of polyfluorene (dash–dot curve) [14]. Each spectrum is normalized to the maximum intensity.

fluorene copolymer [14] and the Gaussian contours separated in Fig. 2.

Fluorene belongs to the hydrocarbons widely occurring in nature [15]. This compound is formed upon the thermal decomposition of various carbon-containing substances and is well known as a chemically stable and active environmental pollutant [15, 16]. Moreover, the absorption spectrum of a fluorene-based polymer (polyfluorene) [14] also exhibits features in the same spectral regions where the extinction features are observed in Fig. 2. However, the relative intensities of the two main components in these cases exhibit opposite trends (Fig. 3). On the contrary, the spectrum of the triphenylamine–fluorene copolymer exhibits both the same positions of the main features and the same tendency in the peak intensity to increase with the energy (frequency) of absorbed photons. However, triphenylamine entering into this copolymer is not among the compounds widely occurring in nature. On the other hand, the C–N bond is chemically stable, for example, in amorphous carbon (a-C:N) formed in the course of carbon deposition in nitrogen-containing plasma under laboratory conditions [17]. Such bonds are typical of triphenylamine proper and of its precursors and derivatives. Therefore, triphenylamine copolymers (or their precursors) can also be present in a-C:N, probably, in the amorphized state. In comparison to the narrow bands observed in the spectra of copolymers (Fig. 3), the two features separated from the interstellar extinction curve can be inhomogeneously broadened as a result of amorphization caused, in particular, by long-term interaction with corpuscular cosmic radiation.

With allowance for the above considerations, the chemical composition of a-C particles in the ISM can be evaluated by assuming them to consist (like the above copolymer) of alternating coupled triphenylamine and fluorene molecules. As can be readily verified, this medium contains 58 at. % of carbon, 40 at. % of hydrogen, and 2 at. % of nitrogen.

According to the above considerations, the solid phase of the interstellar medium is an amorphous carbon-based substance with a certain degree of ordering. The amorphous character is evidenced by the similarity of the optical properties of ISM and a-C. The presence of an order is confirmed by two inhomogeneously broadened spectral features with the maxima at 3.2 and 5.67 eV contributing to the NIE spectrum, where the component at 3.2 eV was revealed for the first time.

REFERENCES

1. E. L. Fitzpatrick and D. L. Massa, Astrophys. J. Suppl. **72**, 163 (1990).
2. E. L. Fitzpatrick, Publ. Astron. Soc. Pac. **111**, 63 (1999).
3. B. T. Draine and H. M. Lee, Astrophys. J. **285**, 89 (1984).
4. W. Kratschmer, L. D. Lamb, K. Fostiropoulos, *et al.*, Nature **347**, 354 (1990).
5. H. W. Kroto and K. McKay, Nature **331**, 328 (1988).
6. W. A. de Heer and D. Ugarte, Chem. Phys. Lett. **207**, 480 (1993).
7. C. Joblin, A. L'Eger, and P. Martin, Astrophys. J. **393**, L79 (1992).
8. L. W. Beegle, T. J. Wdowiak, M. S. Robinson, *et al.*, Astrophys. J. **487**, 976 (1997).
9. W. W. Duley, Astrophys. J. **287**, 694 (1984).
10. J. Fink, Th. Müller-Heinzerling, J. Pflüger, *et al.*, Phys. Rev. B **30**, 4713 (1984).
11. J. Robertson and E. P. O'Reilly, Phys. Rev. B **35**, 2946 (1987).
12. V. I. Ivanov-Omski, A. Tagliaferro, G. Fanchini, *et al.*, Fiz. Tekh. Poluprovodn. (St. Petersburg) **36**, 117 (2002) [Semiconductors **36**, 110 (2002)].
13. N. F. Mott and E. A. Davis, *Electronic Processes in Non-Crystalline Materials* (Clarendon Press, Oxford, 1971; Mir, Moscow, 1974).
14. J. C. Sancho-Garcia, C. L. Foden, I. Grizzi, *et al.*, J. Phys. Chem. B **108**, 5594 (2004).
15. A. Kot-Wasik, Anal. Chim. Acta **505**, 289 (2004).
16. D. Garon, L. Sage, D. Wouessidjewe, *et al.*, Chemosphere **56**, 159 (2004).
17. J. Zhang, Sh. Fan, and Ch. M. Lieber, Appl. Phys. Lett. **66**, 3582 (1995).

Translated by P. Pozdeev

Stability of Quasi-Ballistic MESFETs
with Various Buffer Layer Structures under Irradiation
with Neutrons Possessing Different Energy Spectra

E. V. Kiseleva, S. V. Obolensky, M. A. Kitaev, O. V. Tkachev,
V. P. Shukaĭlo, and V. T. Gromov

Nizhni Novgorod State University, Nizhni Novgorod, Russia
Received May 19, 2005

Abstract—The effect of irradiation with neutrons possessing an average energy of 1.1 and 14 MeV on the characteristics of quasi-ballistic metal-Schottky-gate field-effect transistors (MESFETs) with various structures of the buffer layer has been studied. In the series of MESFETs with buffers based on a GaAs homostructure, AlGaAs-based heterostructure, and AlAs/GaAs superlattice, the radiation stability increases (on every passage, by a factor of 1.2–5) due to the compression of electron trajectories in the conducting channel and the gettering of radiation defects at a heteroboundary of the buffer layer. © *2005 Pleiades Publishing, Inc.*

As is known, the use of heterostructures improves the characteristics of field-effect transistors, in particular, with respect to the two-dimensional electron gas formation in high-electron mobility transistors (HEMTs) [1]. However, as the size of the active region in such devices is decreased to a level corresponding to collisionless flight, the advantages of HEMTs over the usual metal-Schottky-gate field-effect transistors (MESFETs) become less pronounced [2]. From this standpoint, good prospects are offered by MESFETs with a built-in energy barrier at the channel–buffer interface [3], which separates the active region from a substrate.

Under conditions of irradiation, the presence of any heteroboundary is an additional factor of risk for the transistor structure: ternary compounds are unstable and are susceptible to radiation-induced decomposition [4], while heteroboundaries can be the sites of defect accumulation [5]. The problem of defect formation at heteroboundaries is usually related to the radiation resistance of laser structures and heterobipolar transistors—devices in which the carriers move in the direction perpendicular to the interfaces between layers. In the case of field-effect transistors, it is important to consider changes in the parameters of heteroboundaries that significantly influence the lateral transport of electrons immediately at the barrier, in particular, in the investigation of the radiation resistance of HEMTs [6]. No such investigations have been performed previously for quasi-ballistic MESFETs based on heterostructures with buffer layers.

This Letter presents the results of investigations of a series of quasi-ballistic MESFETs with recessed (V-shaped) gates and buffer layers based on (i) a GaAs homostructure (Fig. 1a) [7], (ii) an AlGaAs-based het-erostructure (Fig. 1b), and (iii) an AlAs/GaAs superlattice (Fig. 1c) [3]. The superlattice period was optimized so as to provide for the maximum (~90%) coefficient of reflection for hot electrons. This was achieved due to a small width ($\approx$23 meV) of the first band of dimensional quantization in the Γ valley, which is situated $\approx$180 meV above the conduction band bottom in GaAs (this energy gap is much greater than the transverse energy component of electrons in the conducting channel). The first miniband of dimensional quantization in the X valley had a width not exceeding 5 meV. Owing to the special shape of the gate, the channel length in such MESFETs is within 30–100 nm [7], which provides for a quasi-ballistic character of electron motion in the active region. Since the structures of transistors in the series studied differed only in the type of buffer layer, all the radiation-induced changes in their characteristics must be related to the presence of heteroboundaries. Therefore, by comparing the parameters of MESFETs with homo- and heterobuffer layers, it is possible to extract information concerning radiation-induced changes in the electron transport along these heteroboundaries.

In this study, the drain–gate current–voltage (I–U) curves of MESFETs with homo- and heterobuffer layers were measured before and after irradiation with neutrons possessing different energy spectra. We have studied 30 devices of each type. The MESFETs with GaAs and AlGaAs buffers were irradiated from both the gate and substrate sides with neutrons possessing an average energy of 1.1 and 14 MeV, while the transistors with buffers based on the superlattice were exposed only to 1.1-MeV neutrons from the gate side. The samples were irradiated in a pulsed nuclear reactor producing 800-μs pulses of neutrons with a dome-shaped spectrum and an average energy of 1.1 MeV; the time
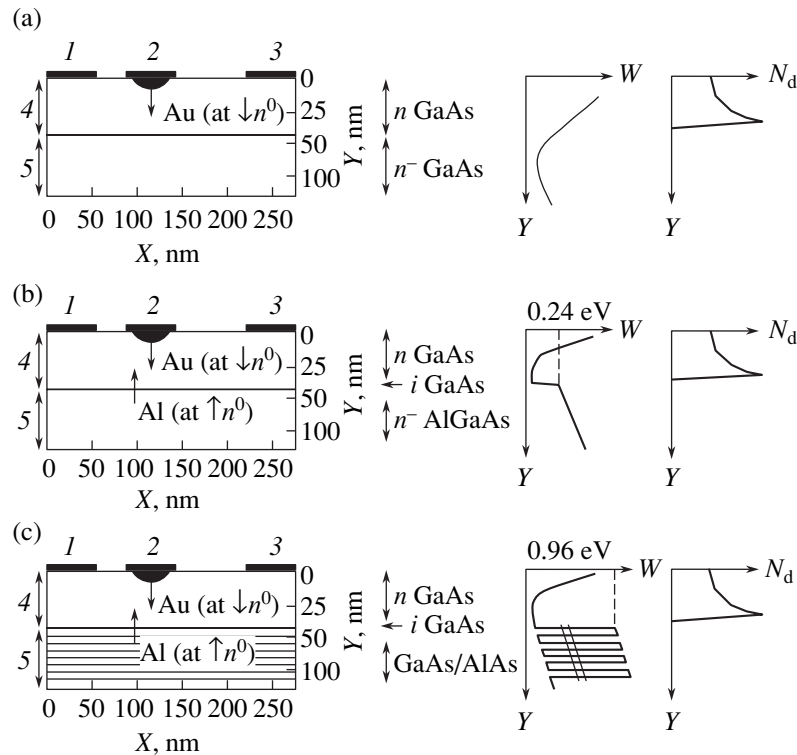
Fig. 1. Schematic diagrams showing the structures, conduction band bottom energy W profiles, and dopant concentration N_d profiles for quasi-ballistic MESFETs with buffer layers based on (a) a GaAs homostructure, (b) an AlGaAs-based heterostructure, and (c) an AlAs/GaAs superlattice: (*1*) source; (*2*) gate; (*3*) drain; (*4*) channel; (*5*) buffer. Arrows indicate the injection of Au atoms from the gate and Al atoms from the heterobuffer for various directions of neutron irradiation.

interval between pulses was one day. The MESFETs with superlattices were irradiated in a continuous regime, but at the same rate of accumulation of the neutron fluence. The beam of neutrons possessing an average energy of 14 MeV was obtained in an NG-12 neutron generator whose energy spectrum was close to monochromatic; the total fluence gained over a 10-h continuous operation period was about 10^{14} cm^{-2}.

We have studied relative changes in the threshold voltage $\Delta U/U_0 = (U_0 - U_F)/U_0$ and the *I–U* curve slope (transconductance) $\Delta g/g_0 = (g_0 - g_F)/g_0$ as functions of the neutron fluence F_n at different energies (Fig. 2). A change in the transconductance was determined primarily by defects contained in the channel, while changes in the threshold voltage were caused by the defects occurring at the channel–buffer interface.

The obtained experimental data were interpreted using a combination of two models. The first model [8] was based on a quasihydrodynamic approximation of the motion of carriers in the channel of transistors with buffer layers of different types, which were set by introducing an energy barrier of a corresponding shape into the potential profile at the channel–buffer interface. The second model [9] involved Monte Carlo simulation of the process of defect formation in the device structures under various conditions of neutron irradiation, with allowance for the injection of gold atoms knocked out

of the gate and aluminum atoms injected from the heterobuffer (Fig. 1).

The model calculations and experiments gave the following results.

(i) The presence of a heterobuffer leads to compression of the electron trajectories in the conducting channel, whereby most of the charge carriers move along short trajectories in a thin region of the channel at the heteroboundary. This circumstance explains the observed sequential two- to threefold decrease in the rate of change of the transistor parameters with increasing energy barrier at the channel–buffer interface in the series of heterostructures studied (Fig. 2).

(ii) The energy of electrons in the channel is 0.4–0.7 eV and, hence, the carriers are scattered predominantly on subclusters of the radiation defects [10], rather than on the whole clusters. In the samples irradiated with 14-MeV neutrons, the average size of such subclusters is approximately two times greater and their scatter is about 2.5 times greater than those in the samples irradiated at an average neutron energy of 1.1 MeV. This fact accounts for the observed sequential decrease by a factor of 1.2–2 in the rate of change in parameters of the transistors with homobuffers and a greater (on the average) scatter of their parameters observed upon the irradiation of 14-MeV neutrons (Fig. 2).
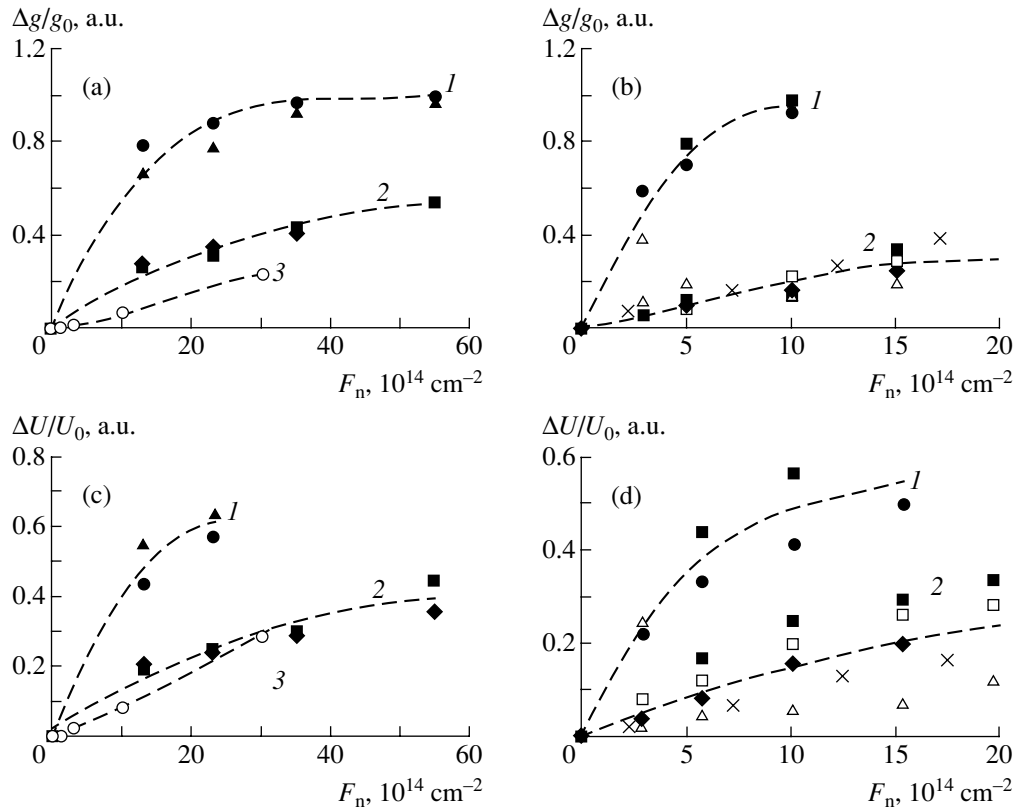
Fig. 2. Variation of the (a, b) transconductance and (c, d) threshold voltage of MESFETs with (*1*) GaAs, (*2*) AlGaAs, and (*3*) GaAs/AlAs buffer layers irradiated by neutrons with different spectra and average energies: (a, c) 1.1 MeV; (b, d) 14 MeV. The data are presented for the samples showing typical behavior in each series of devices of the *1–3* types.

(iii) The transconductance of the devices with homobuffers is sensitive to the direction of irradiation, which is related to the fact that the gold penetration depth was ≈40 nm for 1.1-MeV neutrons and ≈100 nm for 14-MeV neutrons. For this reason, only a small number of gold atoms is injected into the channel of devices irradiated with 1.1-MeV neutrons (most of the knocked out gold atoms are stopped in a titanium sublayer), although the number of injected gold clusters will increase with the neutron fluence. At the same time, the knocked out titanium atoms form defects outside the active region. The irradiation with 14-MeV neutrons from the gate side leads to the formation of gold subclusters in the channels of transistors of all types. In MESFETs with heterobuffers, this irradiation also leads to the injection of aluminum atoms knocked out of the heterobuffer, which is more pronounced in the case of irradiation via substrate and less pronounced for the irradiation from the gate side. In comparison with the influence of intrinsic Ga and Au atoms, the injected Al atoms (possessing a lower weight) produced a relatively smaller disorder in the channel, so that the injection of aluminum can be ignored (to the first approximation) for both neutron energies.

(iv) In the MESFETs with heterobuffers, a change in the transconductance does not depend on the direction of neutron irradiation (Fig. 2b). This is probably explained by a transformation or rearrangement of point defects formed in the active region. The stressed channel–buffer interface acts as a getter collecting a part of defects from the channel. This assumption is confirmed by two experimental facts. First, the threshold voltage of MESFETs with AlGaAs buffers is sensitive to the direction of neutron irradiation (Fig. 2d), and the scatter of cutoff voltages exceeds that of the transconductance. In the devices with superlattices, the rate of variation of the threshold voltage is 20–30% greater than that of the transconductance, which confirms the conclusion that defects are displaced toward the supertlattice. Second, the MESFETs with heterobuffers are insensitive to the neutron energy. Apparently, differences in the defect concentrations and topologies in the active regions of such devices lead to changes in the redistribution of these defects such that the effect of gettering in the case of irradiation with 14-MeV neutrons is more pronounced.

On the whole, a positive change (a two- to threefold increase) in the radiation resistance is produced by the compression of electron trajectories in the presence of an energy barrier for the charge carriers, and an additional positive effect (increase by a factor of 1.5–2) is related to the gettering of defects at a heteroboundary of

the buffer layer. The latter effect is more pronounced (due to the presence of several stressed interfaces) in MESFETs with AlAs/GaAs superlattices than in the devices with AlGaAs heterobuffers.

REFERENCES

1. Yu. Pozhela, *Physics of Fast Transistors* (Mokslas, Vil'nyus, 1989) [in Russian].
2. M. S. Shur, IEEE Electron Device Lett. **23**, 511 (2002).
3. P. A. Volchkov, K. S. Zhuravlev, M. A. Kitaev, *et al.*, Izv. Ross. Akad. Nauk, Ser. Fiz. **68**, 94 (2004).
4. V. S. Vavilov, *Effects of Radiation on Semiconductors* (Fizmatgiz, Moscow, 1963; Consultants Bureau, New York, 1965).
5. M. S. Shur, *GaAs Devices and Circuits* (Plenum, New York, 1987; Mir, Moscow, 1991).
6. A. E. Rengevich, Pis'ma Zh. Tekh. Fiz. **25** (8), 55 (1999) [Tech. Phys. Lett. **25**, 317 (1999)].
7. S. V. Obolenskiĭ and M. A. Kitaev, Pis'ma Zh. Tekh. Fiz. **26** (10), 13 (2000) [Tech. Phys. Lett. **26**, 408 (2000)].
8. S. V. Obolenskiĭ, Izv. Vyssh. Uchebn. Zaved., Élektronik., No. 6, 31 (2002).
9. J. P. Biersack, Nucl. Instrum. Methods Phys. Res. B **27**, 21 (1987).
10. E. V. Kiseleva and S. V. Obolensky, Vopr. At. Nauki Tekh., Ser.: Fiz. Radiats. Vozd. Radioélektron. Apparat., Nos. 1–2, 46 (2004).

Translated by P. Pozdeev

Field-Modulated Conductivity
in Quasi-One-Dimensional Molecular Conductors

I. I. Bobrinetskiĭ, V. K. Nevolin*, S. V. Khartov, and Yu. A. Chaplygin

Moscow State Institute of Electronic Engineering (Technical University), Zelenograd, Russia
* e-mail: vkn@miee.ru
Received June 7, 2005

Abstract—Planar molecular conductors between two carbon nanotubes in a polymer matrix have been created and studied. It is established that the conductivity of the obtained current channel can be modulated by the transverse electric field. A sharp variation of the transverse field can switch off the molecular channel, while the subsequent application of the longitudinal field to the channel switches it on again. In order to explain the observed behavior, it is necessary to consider the micromechanics of molecules in external electric fields. © 2005 Pleiades Publishing, Inc.

The creation and investigation of quasi-one-dimensional conductors (quantum wires) has received much attention because such materials can provide for substantial progress in the development of nanoelectronics [1], including new nanodimensional sensors of various physicochemical quantities [2]. One promising direction is related to the use of single polymer molecules—in particular, carbon nanotubes—as such quasi-one-dimensional conductors [3].

Previously, we created two-electrode elements with quasi-one-dimensional vertical polymer microconductors in a tunneling microscope and showed that these elements possess unique properties [4]. In particular, the obtained microconductors exhibited spontaneous quantization of the conductivity at room temperature. The quantum of resistance determined in experiment deviated from the theoretical value by no more than 20%. The polymer microconductors could pass currents up to 200 mA due to the ballistic transport of charge carriers. Apparently, these were the first elements created by means of probe nanotechnology.

In order to create quasi-one-dimensional conducting channels using dipole–dipole interactions of molecules in an external electric field, it is necessary to provide for several conditions. First, the dipole–dipole interaction energy must exceed the energy of thermal breakage of the conducting channel, which implies that there exists a critical field for the channel formation. Second, the electric field must have a "channel" configuration whereby the longitudinal field component is maximum at the axis and rapidly decays in the radial direction. Third, it is necessary that the linear molecules possess reactive ends and that they be capable of self-assembly with the formation of long conducting channels. Such

conditions were provided between a flat metal substrate surface and a tungsten point probe with a tip radius below 20 nm. By gradually moving the probe away from the surface, it was possible to grow vertical molecular conductors [5].

In order to obtain planar molecular conductors, we used multiwall carbon nanotubes (or their bundles) as electrodes so as to provide the conditions formulated
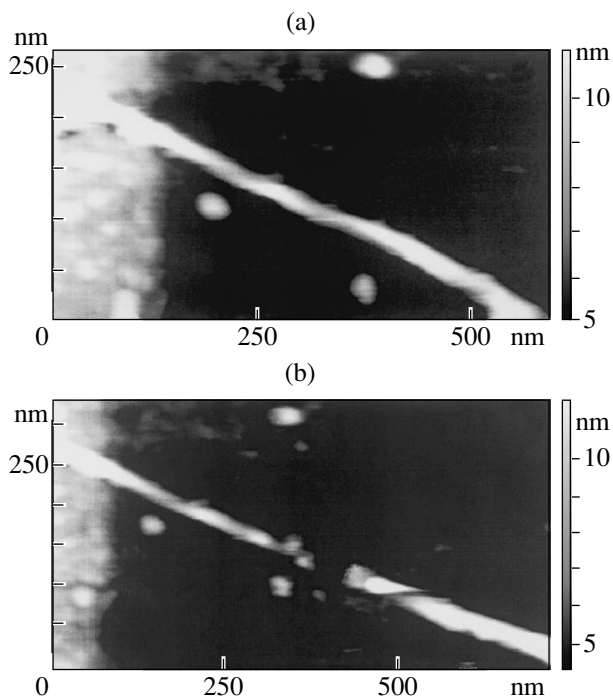

Fig. 1. Atomic force microscope images of a multiwall carbon nanotube (a) before and (b) after cutting (left-hand bright region corresponds to one of the conducting paths).
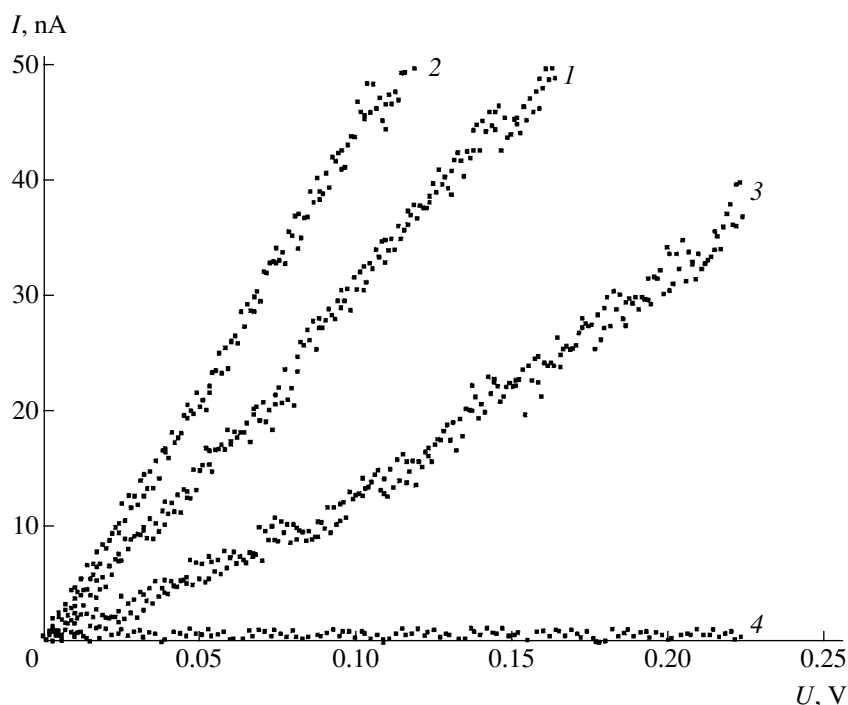
Fig. 2. A family of current–voltage characteristics of a circuit involving the molecular conductor between carbon nanotubes measured at various gate voltages $U_g = 0$ (*1*), –20 (*2*), and +20 V (*3*). Curve *4* corresponds to the conductivity switch-off caused by a sharp change in the applied transverse electric field.

above. These nanotubes were placed between conducting paths and cut (mechanically or electrically) with the aid of the probe of an atomic force microscope (Fig. 1). The obtained gaps ranged from 20 to 500 nm. The field between such electrodes had the required "channel" configuration. A planar molecular conductor was obtained by applying a drop of ED-20 epoxy diane resin (ED-20). This dielectric liquid has a large viscosity, consists of sufficiently long extended molecules with a molecular mass of $M = 400$–900 (containing two benzene rings per monomer), and possesses a residual bulk resistivity on the order of 10^{10} Ω cm. Application of a potential difference of up to 10 V to the gap between nanotubes led to the appearance of electric current in the circuit, which indicated that a molecular conductivity channel was created in the gap. Owing to the planar character of the channel, the molecules constituting this channel are subjected to the orienting action of the substrate. This factor accounts for the stability of the channel in the absence of a drain–source voltage. Since the diameter of nanotube electrodes is on the order of 10 nm and the applied voltage is on a level of several volts, the fields generated at the ends of such electrodes reach 10^8–10^9 V/m and are sufficient to provide for the cold electron emission at a high current density. Electrons emitted with an energy exceeding 5 eV can produce a rupture of the intramolecular bonds of the epoxy resin. Therefore, it is not excluded that the molecular channel formed

between carbon nanotubes may contain fragments of the molecules of the epoxy diane resin and residual impurities.

It was found that the conductivity of the molecular channel could be controlled using the third electrode situated under a silicon oxide layer of the substrate. Figure 2 shows several static current–voltage characteristics of a circuit including conducting paths, multiwall carbon nanotubes, and the molecular channel. A considerable contribution to the resistance of this circuit is related to the contacts of nanotubes with the conducting paths. As can be seen, the conductivity of the molecular channel is modulated by the control gate field, so that the experimental device exhibits the properties of a field-effect transistor. It should be noted that multiwall carbon nanotubes played the role of electrodes and their conductance was not significantly modulated by the field. Upon a sharp change in the control field (e.g., switching the gate voltage from –20 to +20 V with a transient time on the order of 0.1 ms), the conductivity disappeared. In order to restore the conductivity, it was necessary to apply again a drain–source voltage of about 10 V. In these regimes, the experimental device exhibited the properties of an energy-independent memory cell.

We believe that the observed experimental behavior can be explained by considering the micromechanics of molecules in external electric fields. The longitudinal electric field aligns macromolecules and favors the for-

mation of linear conducting molecular bridges (evidence for rather high linearity is provided by the ballistic transport regime observed in an analogous vertical structure [4]). The transverse field of the gate probably produces a partial reorientation of the molecules. However, questions concerning the particular mechanism of conductivity modulation in the molecular channel remain open.

REFERENCES

1. V. K. Nevolin, Pis'ma Zh. Tekh. Fiz. **22** (21), 57 (1996) [Tech. Phys. Lett. **22**, 889 (1996)].

2. E. S. Snow, F. K. Perkins, E. J. Houser, *et al.*, Science **307**, 1942 (2005).

3. K. Tsukagoshi, I. Yagi, and Y. Aoygi, Appl. Phys. Lett. **85**, 1021 (2004).

4. V. K. Nevolin and V. A. Bessol'tsev, Elektron. Tekh., Ser. 3: Mikroélektronika, No. 3, 58 (1989).

5. V. K. Nevolin and V. A. Bessol'tsev, RF Patent No. 4905010 (1991).

Translated by P. Pozdeev

A New Method for the Structural Analysis of Thin Island Films

V. I. Psarev and L. A. Parkhomenko

Zaporozhye National Technical University, 69063 Zaporozhye, Ukraine
e-mail: dilap@zntu.edu.ua
Received January 12, 2005; in final form, June 3, 2005

Abstract—Analytical formulas for a systemic analysis of the structural coarsening of an island film on a solid substrate are obtained based on a comparison of the characteristics of theoretical and experimental distributions of the island size. This approach established a correlation between the features of transformation of the experimental distributions (histograms) and the features of processes in the island film material. © *2005 Pleiades Publishing, Inc.*

Let us consider the stability of thin island films with respect to coarsening via the Ostwald coagulation of microscopic islands with the accompanying processes. Important information about this process can be obtained from an analysis of the island size distribution and its variation with time and from a comparison between the experimental histograms and theoretical distributions.

Theoretical island size distributions are obtained from the relation between the rate of the growth and dissolution of microscopic islands and their dimensions, which is called the dimensional motion equation. One variant of such equation was obtained previously [1] through a modification of the Chakraverty formula [2] and can be written as follows:

$$v(u) \; = \; v_k(t)\left(\frac{dr_k}{dt}\right)^{-1}\frac{dr}{dt} \; = \; \frac{u-1}{\gamma(u)}, \qquad (1)$$

where dr/dt is the rate of variation of the size of an island with the current radius $r = r_s/\sin\Theta$, r_s is the effective radius of islands in the substrate plane, Θ is the contact angle, $v_k(t)$ is the reduced rate of variation of the critical island radius r_k with the time t, $u = r/r_k$ is the dimensionless radius, and $\gamma(u)$ is a factor determining the mechanism of the process under consideration.

Assuming that

$$\gamma(u) \; = \; u^s \quad \text{and} \quad v_k(t) \; = \; \frac{dr_k}{dt}\frac{r_k^s}{A_s}$$

(where A_s is a factor characterizing various types of mass transfer corresponding to $s = 1, 2, 3, \ldots$), we obtain a universal formula combining several different mechanisms of the diffusion mass transfer in disperse systems [3]. It should be noted that the quantity s is identical to p in an analogous expression in [4, Eq. (37)]. Tak-

ing into account that each particle in the disperse system under consideration can be assigned its own diffusion regime, it would be expedient to make a generalizing assumption that s can vary in a broad interval from zero to infinity (see also [3]). The information concerning the influence of s on the process has to be exhaustive.

In particular, a mixed reaction–diffusion mechanism corresponds to

$$\gamma(u) = \varepsilon u^3 + u^{1-\alpha}, \quad v_k(t) = \frac{dr_k}{dt}\frac{r_k}{aKV} \;\; \text{and} \;\; \varepsilon = \frac{Kr_k}{D_S},$$

where K is the velocity of atoms crossing the interface (or the rate of their attachment to the island [1]), D_S is the coefficient of surface diffusion of the adatoms, V is the specific volume of the film, and α is the parameter of the structural distribution of islands on the substrate surface. In the case of

$$\gamma(u) = u^3 + \varepsilon_1 u^{1-\alpha}, \quad v_k(t) = \frac{dr_k}{dt}\frac{r_k^2}{aD_S V} \;\; \text{and} \;\; \varepsilon_1 = \varepsilon^{-1}$$

we deal with a mixed diffusion–reaction mechanism leading to the coarsening of islands in the film.

An expression for the set of theoretical distribution functions corresponding to a given $v(u)$ is as follows [5]:

$$\varphi(u) \; = \; \frac{3v_k}{v_k u - v(u)}\exp\left[-3v_k\int\frac{du}{v_k u - v(u)}\right]. \quad (2)$$

In terms of the dimensional variables, each distribution density function at every moment of time t can be determined as $f(r, t) = Cr_k^{-4}\varphi(u)$, where C is a constant quantity. The characteristics of particular theoretical distribution curves significantly depend on the factor $\gamma(u)$ in Eq. (1). Taking this circumstance into account,

Table 1. Numerical characteristics of the theoretical distribution density function of islands with respect to their relative size for various values of s in the quantity $\gamma(u) = u^s$ in Eq. (1)

s	u_g	v_k	u_m	u_{p1}	u_{p2}	v
0	∞	1	0	–	0	∞
0.2	6	0.5824	0.2180	–	0.6745	27.528
0.5	3	0.3849	0.6633	–	1.2055	4.523
0.9	2.111	0.2687	0.9609	0.5143	1.3412	2.197
1	2	0.25	1	0.6084	1.3458	2
2	1.5	0.1481	1.1346	0.9721	1.290	1.322
5	1.2	0.067	1.1187	1.0777	1.1588	1.073
∞	1	0	1	1	1	1

Note: $v = u_g/u_m$ is the degree of asymmetry of the distribution density curve; u_{p1} is the bending point on the distribution curve in the interval from 0 to u_m; u_{p2} is the bending point on the distribution curve in the interval from u_m to u_g; for other notations see the text.

we will obtain the corresponding expression using [1, Eqs. (9)–(11)].

The upper boundary of the relative island size $u_g = r_g/r_k$ (where r_g is the maximum island size, that is, the distribution width) can be determined from the following equation:

$$\gamma - \gamma' u(u-1)|_{u_g} = 0. \tag{3}$$

The reduced velocity $v_k = v_k(t)$ is calculated as

$$v_k = (\gamma + \gamma' u)^{-1}|_{u_g} = (\gamma' u^2)^{-1}|_{u_g}. \tag{4}$$

The values of $u_m = r_m/r_k$ (where r_m is the modal radius corresponding to the maximum of the distribution density function) can be determined from the equation

$$4 v_k \gamma^2 - \gamma + \gamma'(u-1)|_{u_m} = 0. \tag{5}$$

Positions of the bending points in the distribution curves are determined from the equation

$$2 O v_k^2 \gamma^4 - 13 v_k \gamma^2 z + 2z^2$$
$$- [\gamma\gamma''(u-1) + 2\gamma' z](v_k u \gamma - u + 1)|_{u_p} = 0, \tag{6}$$

where $z = \gamma - \gamma'(u-1)$. In Eqs. (3)–(6), γ' and γ'' denote the first and second derivatives of $\gamma = \gamma(u)$ with respect to u.

Table 1 gives the numerical values of characteristics of the theoretical distributions of islands with respect to their relative size for various values of s in the quantity $\gamma(u) = u^s$. It should be noted that no contradictions appear in the case of continuous variation of s from zero to infinity. The well-known theoretical distributions can be obtained for the corresponding values of s, including the Wagner distribution ($s = 1$) [6], the Lifshits–Slezov

distribution ($s = 2$) [7], and some others [8, 9]. All these distributions exhibit one, two, or none bending points for s varying from zero to infinity, and they have a single bending point in the interval from u_m to u_g.

Assuming that $s = 0$ ($u_g = \infty$, $v_k = 1$) and substituting Eq. (1) into expression (2), we obtain $\varphi(u) = cu\exp(-3u)$. Since $v_k > 0$, a disperse system of islands described by this function is susceptible to diffusion coagulation. For large s ($s = \infty$), a polydisperse system of islands degenerates into a monodisperse one, which is not susceptible to coagulation ($v_k = 0$).

However, all distributions with s in the interval $I \le s < \infty$ (including the well-known distributions) exhibit a negative asymmetry with the coefficient $S_k = \mu_3/\sigma^3 < 0$, where μ_3 is the central moment of the third order and σ is the standard variance.

Table 2 gives the numerical values of characteristics of the theoretical two-parametric distribution functions corresponding to two mechanisms of island coarsening in the disperse system. The case of $\alpha = \varepsilon = 0$ corresponds to the Wagner distribution function [6], and the case of $\alpha = \varepsilon_1 = 0$ corresponds to the Chakraverty distribution [2]. This table also presents the results of an analysis of the experimental data [10] on the distribution of the effective radii of platinum islands on γ-Al_2O_3 substrates. In these experiments, the samples of films on the substrates were heated to 700°C in a 2%O_2 + N_2 atmosphere. The analysis showed a high similarity of the theoretical and experimental distributions, which allowed us to determine the parameters of distributions (using [1, Eq. (15)]) upon a heat treatment for 1 h ($\alpha = 0.19$, $\varepsilon = 0.01$, $S_k = -0.276$, $r_k = 9.32$ nm) and for 16 h ($\alpha = 0.362$, $\varepsilon = 0.01$, $S_k = 0.311$, $r_k = 11.48$ nm). A change in the sign of S_k is indicative of a significant transformation of the experimental distribution function. Further evidence for an anomalous course of the Ostwald coagulation of islands is provided by the character of variation of the parameter α, the related change

Table 2. Numerical characteristics of the theoretical distribution density function of islands with respect to their relative size for various values of $\gamma(u)$ in Eq. (1)

α	$\varepsilon; \varepsilon_1$	u_g	v_k	u_m	u_{p1}	u_{p2}	v
$\gamma(u) = \varepsilon u^3 + u^{1-\alpha};\ 0 \le \alpha \le 1;\ 0 \le \varepsilon \le 1$							
0	0	2	0.25	1	0.6084	0.1358	2
0.2	0	2.25	0.2904	0.9110	0.3803	1.3298	2.4697
					0.1239		
0.8	0	6	0.5824	0.2180	–	0.6746	27.528
0.8	0.05	2.0449	0.3231	0.5752	–	1.3570	3.5552
0.19	0.01	2.0924	0.2730	0.9421	0.4443	1.3437	2.2210
					0.1100		
0.362	0.01	2.2649	0.3100	. 0.8440	–	1.3216	2.6835
$\gamma(u) = u^3 + \varepsilon_1 u^{1-\alpha};\ 0 \le \alpha \le 1;\ 0 \le \varepsilon \le 1$							
0	0	1.3333	0.1055	1.1417	1.0508	1.2297	1.1679
0	0.5	1.3865	0.0830	1.1455	1.0314	1.2565	1.2104
0.2	0.5	1.3890	0.0841	1.1459	1.0307	1.2583	1.2122
					0.0688		
1	0.5	1.3948	0.0881	1.1480	1.0310	1.2640	1.2149
1	0.8	1.4254	0.0807	1.1481	1.0167	1.2800	1.2417

in u_g, v_k, and v, and a decrease in the fraction of growing islands from 24.91 to 18.69% after the 16-h heating.

The proposed method for the identification of the experimental distributions based on the comparison of their characteristics with those of the theoretical distribution functions can provide substantial supplementary information to that obtained by means of a dispersive computer-aided analysis analogous to the procedure used in the case of volume disperse systems [11]. The new approach provides valuable information on the influence of various factors (doping, interaction with atmosphere, faceting of the growing islands, etc.) on the process of coarsening of the island film material.

REFERENCES

1. V. I. Psarev, Metally, No. 6, 105 (1999).
2. B. K. Chakraverty, J. Phys. Chem. Solids **28**, 2401 (1967).
3. V. I. Psarev, Metally, No. 5, 87 (2003).
4. S. A. Kukushkin and A. V. Osipov, Zh. Éksp. Teor. Fiz. **113**, 2193 (1998) [JETP **86**, 1201 (1998)].
5. V. I. Psarev, Izv. Vyssh. Uchebn. Zaved., Fiz., No. 12 (1990).
6. C. Wagner, Z. Elektrochem. **65**, 581 (1961).
7. I. M. Lifshitz and V. V. Slezov, Zh. Éksp. Teor. Fiz. **35**, 479 (1958) [Sov. Phys. JETP **8**, 331 (1958)]
8. R. D. Vengrenovith, Acta Metall. **30**, 1079 (1982).
9. V. V. Kondrat'ev and Yu. M. Ustyugov, Fiz. Met. Metalloved. **76** (5), 40 (1993).
10. P. Wynblatt and N. A. Gjostein, Scr. Metall. **7**, 969 (1973).
11. V. I. Psarev, Izv. Vyssh. Uchebn. Zaved., Tsvetnaya Metallurgiya, No. 3, 28 (2001).

Translated by P. Pozdeev

Field Ion Microscopy of Objects on a Micron Scale

V. A. Ksenofontov, E. V. Sadanov, I. M. Mikhailovskij*, and O. A. Velikodnaya

Kharkov Institute of Physics and Technology, National Scientific Center, Kharkov, Ukraine
* e-mail: mikhailovskij@kipt.kharkov.ua
Received June 6, 2005

Abstract—An anomalously low level of electric field strengths for the field evaporation and field ionization of metals and alloys has been observed in the presence of elevated partial pressures of water vapor. This effect can be used in field ion microscopy for the formation and polishing of point samples with dimensions on a micron scale, which allows the sample volume to be increased by 3–4 orders of magnitude. © *2005 Pleiades Publishing, Inc.*

Field ion microscopy (FIM) is one of the methods making possible the direct observation of atoms on solid surfaces. Among the other modern high-resolution techniques of surface physics, FIM is distinguished by the ability to form atomic-smooth surfaces of samples with various crystal orientations, which is achieved due to the phenomenon of field evaporation. This makes possible, in particular, the investigation of surface morphology on the crystal faces with high Miller indexes. Field evaporation has been widely used [1, 2] for the cleaning and smoothening of points prior to FIM imaging. Sequential field evaporation of surface layers reveals the internal structure of the point material, thus being an important tool not only for the preparation of samples, but for the subsequent profound investigation of their microstructure as well [2].

As is known, the operation of a field ion microscope (ion projector) requires the creation of an electric field with a strength of $(2–6) \times 10^{10}$ V/m at the sample surface, which provides for the field ionization of atoms of an inert gas usually employed for the FIM image formation. Such field strengths can be created at the surface of a sample with a point tip curvature radius of $10–100$ nm at an applied positive potential of 2–30 kV. The possibility of increasing the radius of curvature at the point tip is limited by the breakage of point samples under the action of ponderomotive forces developed in the electric field [3], which is related to the strength scaling factor. An increase in the sample surface radius is accompanied by the growth of the working voltage and, hence, of the vacuum breakdown, which also leads to breakage of the samples.

This Letter presents the results of our attempts to increase the range of dimensions for the samples studied by FIM. This was achieved by using the phenomenon of water-vapor-stimulated field evaporation [1, 4] for the sample surface formation. It was demonstrated [4] that the field strength required for the evaporation of tungsten is decreased 2–2.5 times in the presence of water vapor with a partial pressure of $(1.9–2.7) \times 10^{-4}$ Pa. We have performed experiments on the field evaporation of samples at elevated partial pressures (up to 10^{-1} Pa) of water vapor and observed an anomalous—by two orders of magnitude—decrease in the evaporation field strength for some metals at room temperature, which allows the limiting curvature radii of samples for the FIM imaging to be increased up to several microns.

The experiments were performed in a field ion microscope equipped with an image brightness enhancer employing an MKP-46 microchannel plate (amplification coefficient, 10^3). The residual gas pressure in the vacuum chamber was 10^{-5} Pa, and the partial pressure of water vapor was controlled on a level of $10^{-1}–10^{-2}$ Pa. Under these conditions, the evaporation field strength for tungsten and a W–20% Re alloy at room temperature decreased from 5.5×10^{10} V/m (in a residual vacuum) to 6×10^8 V/m (in the presence of water vapor). The analogous phenomenon of decrease in the room-temperature evaporation field strength at elevated partial pressures of water vapor was observed for molybdenum and chromium–nickel steel Kh18N10T. An unexpected result was that the rate of water vapor ionization at such low electric field strengths was sufficient for the FIM image formation. According to the classical theory of the field ionization for gases [1, 2], the known ionization potential of water molecules (12.6 eV) implies a much higher ionization field strength on the order of $\sim 10^{10}$ V/m.

In order to evaluate the sample surface curvature radius and the magnification factor, we used either the initial value of the tip radius determined according to the standard FIM method [1] or the final tip radius after the field evaporation, as determined using shadow imaging in an optical microscope. Intermediate values of the sample curvature were determined assuming a linear relation between the field evaporation voltage and the sample curvature radius. The evaporated layer thickness was calculated from a change in the field
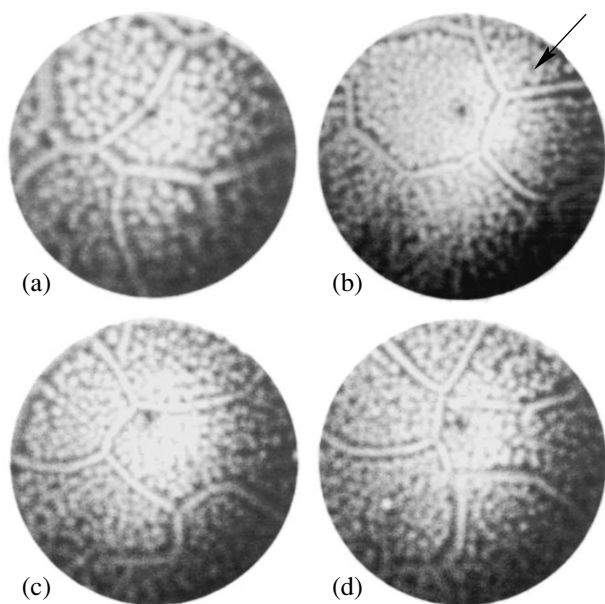
Fig. 1. A series of FIM images of the surface of a polycrystalline point prepared from a non-recrystallized W–20% Re alloy and studied under the conditions of water-vapor-stimulated field evaporation.
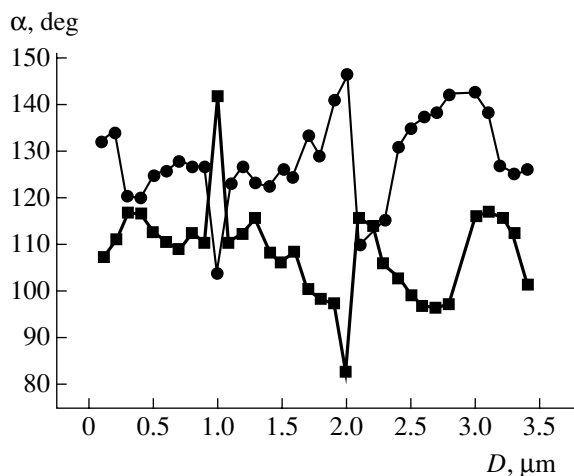

Fig. 2. The typical depth profiles of dihedral angles α between grain boundaries at a triple junction indicated by the arrow in Fig. 1.

evaporation voltage for a preliminarily determined value of the cone angle at the sample point tip.

For samples on a micron size scale, the resolution of a field ion microscope is virtually independent of the diffraction effects and the size of imaging gas molecules. In this case, the well-known expression for the resolution of an ion projector [1] can be written as

$$\delta = 4\beta\left(\frac{rkT}{k_f eF}\right)^{1/2},$$

where r is the sample curvature radius, β is the image compression factor, k_f is the field geometry factor, T is the sample temperature, F is the electric field strength at the sample surface, and e is the electron charge. For our instrument, the field geometry factor (which depends on the electrode configuration) was $k_f = 10$. For the samples with $r = 1$ µm, the field strength for the best image was $F = 2 \times 10^9$ V/m. Assuming the image compression factor to be $\beta = 1.5$ and the sample temperature $T = 300$ K, we estimate the resolution at $\delta = 7$ nm. This value is decreased as compared to the resolution achieved in the instruments using inert imaging gases, but all the other advantages (including the possibility of forming atomically-smooth surfaces and studying the sample microstructure *in situ* in the course of sequential layer removal by stimulated field evaporation) are retained.

Figures 1a–1d show a series of FIM images of the surface of a polycrystalline point prepared from a non-recrystallized W–20% Re alloy. The sample voltage in the course of exposure was 12 kV, while the field strength in the course of material evaporation and the resulting increase in the tip curvature radius monotonically decreased from 2×10^9 to 1.5×10^9 V/m. The micrographs presented in Fig. 1 were obtained in the course of the water-vapor-stimulated field evaporation of a 1-µm-thick layer of the sample. As can be seen, the FIM images display grains comprising chaotic sets of bright spots and reveal grain boundaries, which are decorated in the course of stimulated field evaporation in the presence of water vapor. The micrographs in Fig. 1 show the possibility of using the proposed FIM technique for investigations of the topology and statistics of the ensemble of grain boundaries and their triple junctions. In particular, we have determined the statistical distributions of dihedral angles α between grain boundaries and studied their variation in the course of stimulated field evaporation to a depth D.

Figure 2 shows the typical distributions of dihedral angles α between grain boundaries at the triple junctions. The angles were measured by passing at a step of about 100 nm along the triple junction line. The dihedral angle is one of the main characteristics of triple junctions and is a factor determining the mechanical and other structure-sensitive properties of fine-grained polycrystalline materials [5]. Until now, FIM has not been used for the investigation of dihedral angle distributions in individual triple junctions, this being related to the limited volume of material removed in the course of field evaporation. Previously, statistically reliable data were obtained only for the ensembles of triple junctions in various samples [6, 7].

Using the anomalous decrease in the evaporation field strength as a result of the water-vapor-stimulated field evaporation, it is possible to study the samples with initial dimensions on a micron level and to

increase the volume of evaporated material to 10^3–10^4 μm^3, which is 3–4 orders of magnitude greater than the volume evaporated in the standard FIM investigations using inert imaging gases.

REFERENCES

1. E. W. Muller and T. T. Tsong, *Field Ion Microscopy, Field Ionization, and Field Evaporation* (Pergamon, Oxford, 1973).

2. M. K. Miller, A. Cerezo, M. G. Hetherington, and G. D. W. Smith, *Atom-Probe Field Ion Microscopy* (Oxford Univ. Press, Oxford, 1996).

3. I. M. Mikhailovskij, P. Ya. Poltinin, and L. I. Fedorova, Fiz. Met. Metalloved. **56**, 186 (1983).

4. N. M. Blashenkov, G. Ya. Lavrent'ev, and V. N. Shrednik, Pis'ma Zh. Tekh. Fiz. **30** (12), 50 (2004) [Tech. Phys. Lett. **30**, 509 (2004)].

5. V. Randle, Acta Metall. Mater. **43**, 1741 (1994).

6. I. M. Mikhailovskij and E. V. Sadanov, Poverkhnost: Fiz. Khim. Mekh. **5**, 119 (1990).

7. A. S. Lazarenko, I. M. Mikhailovskij, V. B. Rabukhin, and O. A. Velikodnaja, Acta Metall. Mater. **43**, 639 (1994).

Translated by P. Pozdeev

Bromine–Iodine Excimer Electric-Discharge Lamp with Continuous UV Radiation Spectrum

A. K. Shuaibov and I. A. Grabovaya

Uzhgorod National University, Uzhgorod, Ukraine
e-mail: ishev@univ.uzhgorod.ua
Received May 3, 2005

Abstract—The optical characteristics of a small-size UV lamp filled with a working mixture of xenon and krypton with bromine and iodine vapor and pumped by longitudinal electric discharge have been studied. The lamp emits a resonance atomic line of iodine I* at 206.2 nm (with a full width at half maximum of 0.10 nm) and a continuum in the range 220–390 nm, which is formed by the emission bands of diatomic molecules [XeI(B–X), XeBr(B,D–X), Br_2(B–X), I_2(B–X), and IBr(B–X)]. The optimum partial pressure of iodine vapor is 100–200 Pa, that of bromine vapor ranges from 130 to 400 Pa, and that of heavy inert gases, from 400 to 800 Pa. The average total UV output radiation power was 10–12 W at an efficiency of 10–12%. © *2005 Pleiades Publishing, Inc.*

Excimer–halogen dc lamps are the most powerful sources of UV radiation available at present, but the working life of such sources operating on the 222 nm (KrCl*) and 308 nm (XeCl*) bands does not exceed 100 h [1]. The passage to iodine, which is the least aggressive halogen, increases the working life of a glow-discharge-pumped lamp in a static regime up to 500–1000 h [2, 3]. About half of the output radiation power of such lamps is concentrated in the form of a continuum in the wavelength range from 220 to 360 nm, which represents broadened emission bands at 253 nm (XeI*) and 342 nm (I_2^*).

In order to provide for a more uniform coverage of the 220–400 nm wavelength range and to create an effective wide-band UV lamp capable of operating in the continuous regime (replacing the well-known but insufficiently effective lamp emitting the continuum due to hydrogen molecules), we suggested to supplement the emission from iodine-containing molecules by that of the bromine-containing species. For this purpose, it was necessary to obtain a complex halogen carrier containing a mixture of bromine and iodine vapors. Unfortunately, the emission characteristics of glow-discharge plasmas in Xe–Br_2–I_2 and Kr–Br_2–I_2 mixtures were not previously studied and, hence, the working regimes and output characteristics of such lamps were unknown.

This Letter presents the results of investigations of the emission characteristics of a wide-band UV excimer dc lamp operating on a mixture of heavy inert gases with bromine and iodine vapors.

The longitudinal dc glow discharge was initiated in a quartz discharge tube with an internal diameter of 14 mm and an interelectrode distance of 100 mm. The tube walls were transparent for radiation wavelengths up to 190 nm (on a transmission level of no less than 70%). High-purity crystalline iodine was contained in a special finger situated behind the anode. Bromine vapor was introduced into the discharge tube from a container with high-purity liquid bromine via a special vacuum–gas admission system. The discharge tube was initially evacuated to a residual pressure of 3–7 Pa, washed with neon of spectral purity, and outgassed by glow discharge in this neon at a maximum discharge current. A criterion for the lamp being prepared to filling with a working gas mixture was the absence of most bright lines of the second positive stem of nitrogen in the emission spectra of glow discharge in heavy inert gases.

The emission spectrum of glow discharge plasma generated in the lamp was analyzed using a spectrometer based on a monochromator (MDR-2) with a diffraction grating (1200 lines per mm) or a holographic grating (2400 lines per mm) and a photomultiplier (FEU-106). The detector was preliminarily calibrated with respect to the relative spectral sensitivity in a 190–400 nm wavelength range with the aid of a standard hydrogen lamp. The envelope of the resonance emission line of iodine atoms (λ = 206.2 nm) was studied using a holographic grating.

The glow discharge was power supplied from a high-voltage rectifier ($I_{ch} \leq 100$ mA; $U_{ch} \leq 10$ kV). In the course of experiments, the discharge tube could be heated up to 40°C, so that the saturated iodine pressure was within 100–200 Pa [4]. The total UV radiation power was measured using a power meter of the Quartz-01 type according to the standard photometric technique with allowance for the experimental geometry [5]. The electric power supplied to the discharge was varied from 5 to 100 W. The current–voltage
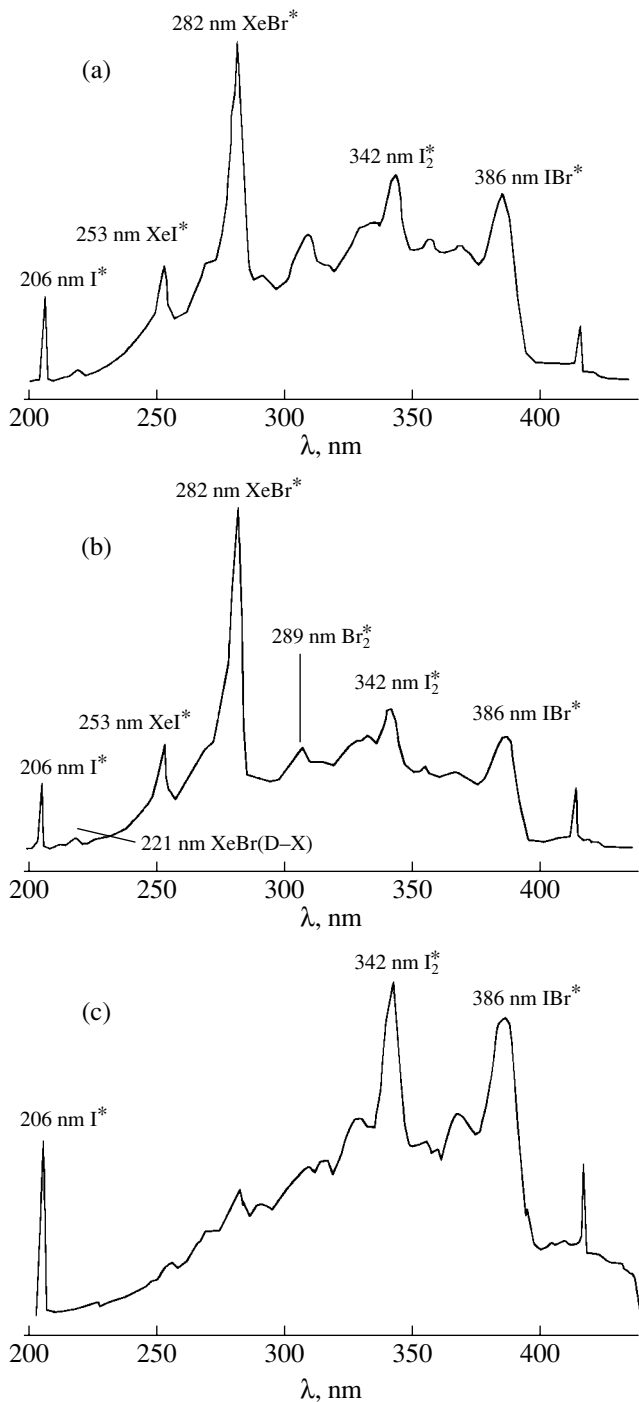
Fig. 1. The typical spectral characteristics of a wide-band excimer–halogen lamp measured at an average discharge current of 30 mA and various partial pressures of the working gas mixture components: (a) $P(Xe)/P(Br_2)/P(I_2) = 800/400/(100–200)$ Pa; (b) $P(Xe)/P(Br_2)/P(I_2) = 1200/130/(100–200)$ Pa; (c) $P(Kr)/P(Br_2)/P(I_2) = 800/200/(100–200)$ Pa.

Fig. 2. Plots of the relative intensity of (*1*) the atomic emission lines at 206.2 nm (I*) and the main continuum components at (*2*) 282 [XeBr[B–X]], (*3*) 253 nm [(XeI(B–X)], and 342 nm [I_2(B–X)] versus electric power supplied to the plasma of glow discharge in a Xe–Br_2–I_2 mixture with the partial pressures $P(Xe)/P(Br_2)/P(I_2) = 800/130/(100–200)$ Pa.

(I–U) characteristics of discharge in Xe and Kr mixtures with Br_2–I_2 vapors corresponded to the subnormal and normal stages of dc glow discharge. The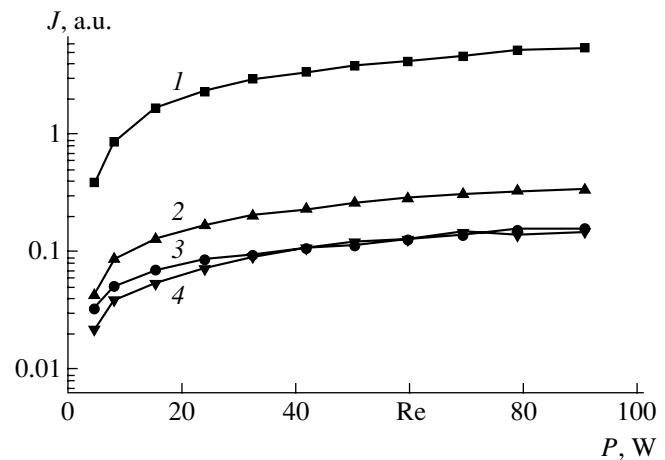 I–U curves were very close to those previously observed for the discharge in Kr and Xe mixtures with iodine vapor [6].

Figure 1 shows the emission spectrum of the proposed dc lamp (without correction for the relative spectral sensitivity of the monochromator and photomultiplier). The most intense emission line corresponding to the emission from atomic iodine at 206.2 nm (I*) was observed in all experiments. The full width at half maximum (FWHM) of this line was 0.10–0.12 nm and weakly depended on the experimental conditions. In the spectrum of discharge in Kr–Br_2–I_2 mixtures, this line virtually coincided with a narrow band at 207 nm (KrBr*) (Fig. 1c). More than half of the total UV output radiation power is concentrated in the continuum extending from 220 to 390 nm, where the main components represent the broad emission bands at 221 nm [XeBr(D–X)], 253 nm [(XeI(B–X)], 282 nm [XeBr[B–X]], 289 nm (Br_2^*), 342 nm (I*), and 386 nm (IBr*). The maximum contribution to the UV continuum was observed for a partial xenon pressure within 400–800 Pa and a partial bromine pressure of 300–400 Pa (Figs. 1a and 1b). In the continuous emission of the lamp filled with Kr–Br_2–I_2 mixtures, the main power was radiated in the spectral interval of 300–390 nm.

Figure 2 shows plots of the intensity of the main spectral line 206.2 nm (I*) and the main continuum components versus electric power supplied to the plasma of discharge in Xe–Br_2–I_2 mixtures. The maximum rate of increase in the intensity of emission for the spectral line of atomic iodine and the main molecular bands was observed in the subnormal stage of discharge. On the passage to a normal stage, the intensity of emission increased with the supplied power at a lower rate. The optimum partial pressure of a heavy

inert gas in the mixture was within 400–800 Pa, while the optimum partial pressures of iodine and bromine vapors were within 100–200 and 100–400 Pa, respectively.

The average total UV output radiation power was 10–12 W at an efficiency (percentage of the electric power supplied to the discharge) of 10–12%. The working life of the experimental lamp was 300–400 h.

In conclusion, we have demonstrated that a low-pressure glow-electric-discharge-pumped lamp filled with a mixture of xenon or krypton with a complex halogen carrier Br_2–I_2 radiates a narrow resonance emission line of iodine atoms (206.2 nm I*) and (predominantly) a continuum over a spectral range from 220 to 390 nm formed by a system of broad emission bands due to xenon and krypton halides. The optimum partial pressure of Xe or Kr in the working mixture was within 400–800 Pa, and those of iodine and bromine vapors were within 100–200 and 100–400 Pa, respectively.

REFERENCES

1. M. I. Lomaev, V. S. Skakun, E. A. Sosnin, *et al.*, Usp. Fiz. Nauk **173**, 201 (2003) [Phys. Usp. **46**, 193 (2003)].
2. M. I. Lomaev and V. F. Tarasenko, Proc. SPIE **4747**, 390 (2002).
3. A. K. Shuaibov and I. A. Grabovaya, Opt. Spektrosk. **98**, 567 (2005) [Opt. Spectrosc. **98**, 510 (2005)].
4. *Properties of Inorganic Compounds: A Handbook* (Khimiya, Leningrad, 1983) [in Russian].
5. A. K. Shuaibov, L. L. Shimon, A. I. Dashchenko, and I. V. Shevera, J. Phys. Stud. **5**, 131 (2001).
6. A. K. Shuaibov and I. A. Grabovaya, Zh. Prikl. Spektrosk. **72**, 247 (2005).

Translated by P. Pozdeev

Discrete Diffraction and Spatial Self-Action of Light Beams in One-Dimensional Photonic Lattices in Lithium Niobate

V. M. Shandarov[a,*], K. V. Shandarova[a], and D. Kip[b,**]

[a] *Tomsk State University of Control Systems and Radioelectronics, Tomsk, Russia*
[b] *University of Technology, Clausthal-Zellerfeld 38678, Germany*
*e-mail: * shan@svch.rk.tusur.ru; ** detlef.kip@tu-clausthal.de*
Received June 14, 2005

Abstract—Features of the behavior of light beams in one-dimensional photonic lattices in iron-doped lithium niobate have been experimentally studied. It is demonstrated that bright discrete spatial solitons and bright gap solitons can be formed in this system using 633 nm radiation on a microwatt power level. © *2005 Pleiades Publishing, Inc.*

Light beams can exhibit diffractionless propagation (called spatial optical soliton regime) in a nonlinear optical medium, whereby the diffraction is completely compensated by self-focusing and self-defocusing effects [1–3]. In recent years, special attention has been devoted to the behavior of light beams in periodic arrays of coupled optical waveguides (OWGs) [4, 5]. In such arrays, the waveguide effect leads to certain features in the diffraction of light and changes the sign of optical nonlinearity for the light propagating in directions close to the Bragg angle [4]. This makes possible the self-focusing of light beams with the formation of bright discrete spatial solitons in a medium with defocusing nonlinearity and, on the contrary, the self-defocusing and the formation of dark discrete solitons in a medium with focusing nonlinearity. Such effects have been observed in one-dimensional arrays of GaAs-based channel OWGs with Kerr's nonlinearity for light with a wavelength of 1.53 µm at an instant power on the order of 10^2 watts [6]. These effects were also observed in one- and two-dimensional photonic lattices (PLs) representing optically induced waveguide arrays in photorefractive crystals of strontium barium niobate [7, 8], where the photorefractive optical nonlinearity allowed the spatial self-action effects to be observed on a microwatt power level. A high photorefractive optical nonlinearity is also inherent in lithium niobate ($LiNbO_3$) doped with iron (Fe), copper (Cu), and some other admixtures. In particular, the formation of bright spatial gap solitons in a one-dimensional channel OWG array in $LiNbO_3$:Cu was observed at a light beam power below 10 µW [9].

This Letter reports on the first experimental study of discrete diffraction and spatial self-action of light beams in one-dimensional PLs formed in $LiNbO_3$:Fe crystals.

The PLs were formed using a double-beam scheme of photorefractive hologram recording with He–Ne laser radiation (λ = 633 nm). The PL vector was oriented along the optical axis of a crystal and the total power of a recording beam was ~1 mW. The polarization of light corresponded to that of the ordinary wave in the crystal. In our experiments, the PL period was varied from 10 to 15 µm and the PL aperture was within 2–3 mm.

Figure 1a shows a schematic diagram of the experimental setup used to study the features of light propagation in the obtained PLs. The laser beam was focused onto the entrance plane of the PL by spherical lenses *4* with a focal length of F = 20–200 mm. The readout beam polarization corresponded to that of the extraordinary wave (i.e., the optical axis of the crystal is parallel to the polarization plane). This polarization allows the depth of the refractive index modulation for the readout beam in the PL region to be increased due to the electrooptical coefficient r_{33}. The image of the exit plane of the PL was projected by lens *5* onto CCD camera *6*. The crystal sample was mounted on a rotary table, which provided for a high-precision adjustment of the light propagation direction relative to the PL vector.

Since the PL represents a system of coupled OWGs, diffraction in the direction of the PL vector can be either completely absent or manifested due to the light tunneling to the adjacent waveguide layers. The discrete diffraction was experimentally studied upon the light wave excitation in one or several (up to six) PL layers. Figure 1b shows the light wave intensity profiles in the entrance (curve *1*) and exit crystal sample faces. The light was focused by a lens with F = 30 mm onto the PL entrance plane where the beam waist size was 15–17 µm. As a result of diffraction, the beam width increased to ~150 µm at the exit plane of a homogeneous crystal 9-mm-long in the direction of light propagation (Fig. 1b, curve *2*). The output intensity distribution in a crystal with the PL with a period of 15 µm illuminated with a parallel beam is depicted by curve *3*. For
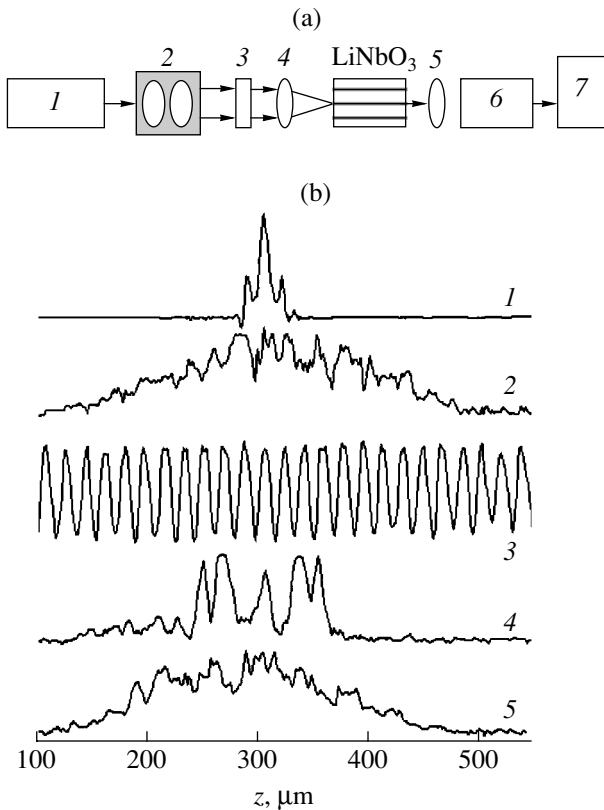
(a)

(b)

Fig. 1. (a) Schematic diagram of the experimental setup used to study the light field in PLs: (*1*) He–Ne laser; (*2*) collimator; (*3*) polarizer; (*4*) spherical focusing lens; (*5*) imaging lens; (*6*) CCD camera; (*7*) personal computer. (b) The patterns of discrete diffraction of a light beam in a one-dimensional PL, showing the light wave field intensity profiles (*1*) in the entrance plane, (*2*) in the exit plane in the absence of a PL, (*3*) in the exit plane for the PL excited by a parallel beam, (*4*) in the exit plane in the lattice vector direction for the excitation of a single waveguide layer, and (*5*) in the plane of a separate waveguide layer.

this PL, the induced change in the refractive index is $\Delta n_e \sim 10^{-4}$. In the case of the excitation of a single waveguide, the main portion of the light energy at the PL exit plane is distributed (as a result of the light tunneling) between five waveguide layers, with a maximum at the periphery (Fig. 1b, curve *4*). This behavior well agrees with the previous experimental and theoretical results [5]. In the waveguide plane, the light beam exhibits diffraction similar to that in a homogenous medium (Fig. 1b, curve *5*).

The optical nonlinearity in photorefractive crystals is manifested even for the light beam power on a microwatt level. As was noted above, the optical nonlinearity changes sign in the region of anomalous diffraction (i.e., for the light propagating in the directions close to the conditions of Bragg's reflection). In the arrays based on $LiNbO_3$ (a material with defocusing photorefractive nonlinearity), this may result in the formation of bright discrete spatial solitons. In addition, the optical nonlinearity can remove the prohibition on light
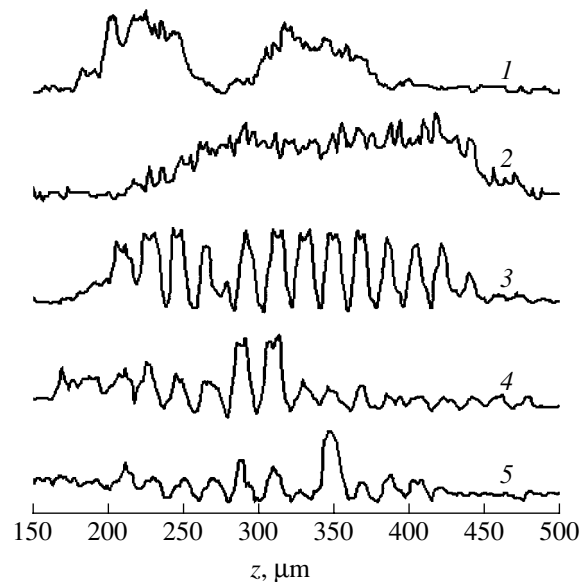

Fig. 2. The patterns of spatial self-action of a light beam, showing the light wave field intensity profiles (*1*) in the initial transmitted beam, (*2*) in the diffracted beam, (*3*) in the PL exit plane at $t = 0$, (*4*) in the PL exit plate at $t = 120$ min (in the stage corresponding to the formation of a discrete spatial soliton), and (*5*) in the PL exit plane at $t = 300$ min (in the stage corresponding to the formation of a spatial gap soliton).

propagation in the directions corresponding to Bragg's reflection, thus leading to the formation of the so-called spatial gap solitons [10].

We have studied the phenomenon of spatial self-action using light beams with a power of 10–50 μW. The array was illuminated in the directions close or corresponding to the conditions of Bragg's reflection. Four to six waveguide layers were excited in this experiment; the light beam was focused onto the PL entrance plane by a lens with $F = 20$ cm. The light wave intensity profiles in the PL output plane are presented in Fig. 2. At the initial moment, immediately upon the excitation of light in the sample array, the distribution of light intensity in the output beam (separated from the total light field by means of spatial filtration) exhibits a characteristic minimum corresponding to the conditions of Bragg's reflection (curve *1*). The intensity of the part of the field reflected from the array is depicted by curve *2*, while curve *3* presents the total field intensity distribution in the PL exit plane.

The photorefractive self-action leads to a change in the light field intensity distribution in the PL exit plane with time. In particular, the field exhibited localization near a direction corresponding to the conditions of Bragg's reflection (Fig. 2, curve *4*), so that a significant part of the energy was concentrated within two waveguide layers. This situation corresponds to the formation of a bright discrete spatial soliton in the region of the field for which the angular spectrum components

occur in the immediate vicinity of the first Brillouin zone edge. In some time, the bright discrete spatial soliton was broken, but a new region of the light wave localization appeared, as is seen in curve *5*. In this case, the light wave field was localized in a single waveguide layer occurring at equal distances from the region of minimum intensity in the transmitted beam (Fig. 2, curve *1*) and the region of maximum intensity in the reflected wave field (curve *2*). Apparently, this stage corresponds to the formation of a spatial gap soliton. Indeed, a gap soliton must correspond to a light beam propagating in the PL in the direction corresponding to the transmission band edge. However, in this case, the group velocity vector must point in the forward direction, so that the energy is transferred along the waveguide layer [10]. Accordingly, the localization of light in the PL exit plane can be expected in the same waveguide layers where the light is excited in the PL entrance plane.

It should be noted that the nonlinear localization of light observed in our experiments did not exhibit a stationary character and the gap soliton was broken with time (like the bright discrete soliton) at the edge of the first Brillouin zone. The main reason for this behavior is evidently the irreversible variation of the PL field upon readout with a beam possessing extraordinary polarization in the absence of recording beams. A certain role is also played by the diffraction of light in the plane of the waveguide layer, which makes the coeffi-

cient of coupling between adjacent waveguide layers dependent on the longitudinal spatial coordinate.

REFERENCES

1. M. D. Iturbe-Castillo, P. A. Merquez-Aguilar, J. J. Sanchez-Mondragon, *et al.*, Appl. Phys. Lett. **64**, 408 (1994).

2. N. N. Rozanov, Opt. Spektrosk. **89**, 422 (2000) [Opt. Spectrosc. **89**, 422 (2000)].

3. N. N. Rozanov, J. Appl. Phys. **89**, 380 (2001).

4. D. N. Christodoulides and R. I. Joseph, Opt. Lett. **13**, 794 (1988).

5. F. Lederer and Y. Silberberg, Opt. Photonics News **2**, 48 (2002).

6. D. Neshev, E. Ostrovskaya, Yu. Kivshar, *et al.*, Opt. Lett. **28**, 710 (2003).

7. J. Fleischer, T. Carmon, M. Segev, *et al.*, Phys. Rev. Lett. **90**, 023902 (2003).

8. D. Mandelik, R. Morandotti, J. S. Aitchison, *et al.*, Phys. Rev. Lett. **92**, 093904 (2004).

9. Yu. Kivshar, Opt. Lett. **18**, 1147 (1993).

10. F. Chen, M. Stepic, C. E. Rüter, *et al.*, Opt. Express **13**, 4314 (2005).

Translated by P. Pozdeev